DRL Line Item No. 10

DOE/JPL-954868-79/1
Distribution Category UC-63

AUTOMATED ARRAY ASSEMBLY, PHASE II

(NASA-CR-158874) AUTOMATED ARAY ASSEMBLY, PHASE 2 Interim Report (RCA Labs., Princeton, N. J.) 136 p HC A07/MF A01 CSCL 10A

N79-29607

Unclas
G3/44 34160

R. V. D'Aiello

RCA Laboratories
Princeton, New Jersey 08540

INTERIM REPORT

JANUARY 1979

This work was performed for the Jet Propulsion Laboratory, California Institute of Technology, under NASA Contract NAS7-100 for the Department of Energy.

The JPL Low-Cost Silicon Solar Array Project is funded by DOE and forms part of the DOE Photovoltaic Conversion Program to initiate a major effort toward the development of low-cost solar arrays.

Prepared Under Contract No. 954868 For

JET PROPULSION LABORATORY
CALIFORNIA INSTITUTE OF TECHNOLOGY
Pasadena, California 91103

PREFACE

This Interim Report, prepared by RCA Laboratories, Princeton, NJ 08540, describes the results of work performed from January 1, 1978 to December 31, 1978 in the Energy Systems Research Laboratory, B. F Williams, Director; Materials and Process Laboratory, Solid State Division, Somerville, NJ, H. Veloric, Manager; and at the Advanced Technology Laboratory, Government and Commercial Systems, Camden, NJ, F. E. Shashoua, Director. The Project Scientist is R. V. D'Aiello and the Project Supervisor is D. Richman, Head, Semiconductor Materials Research. Others who participated in the research and writing of this report are:

E. C. Douglas C. Wu	-	Ion implantation
K. Bube	-	Screen printing
W. Kern	-	Spray-on AR coating
J. Toner	-	Cost analysis
R. Scott P. Coyle	-	Interconnect and panel assembly
L. Guarino	-	Processing

TABLE OF CONTENTS

TABLE OF CONTENTS (Continued)

LIST OF ILLUSTRATIONS

LIST OF TABLES

LIST OF TABLES (Continued)

SECTION I

SUMMARY

This report summarizes the work conducted during a 1-year program designed to establish the technological readiness and provide verification for the elements of a manufacturing sequence which would ultimately be suitable for the large-scale production of silicon solar-array modules at a cost of less than $500/peak kW. Each of Sections II-V, which comprise the main body of this report, contains a detailed description of the development and experimental verification for individual process steps. These sections are self-contained in that the technical data and conclusions concerning the readiness of each process are included. In our earlier programs with JPL, detailed cost analyses of these processes were conducted and reported so that only those factors uncovered in the present work which could cause major deviations in cost are discussed.

Section II describes the results of a detailed experimental study and evaluation of the factors which influence the performance of ion-implanted silicon solar cells. The factors which were investigated include:

(1) Implant dose
(2) Implant energy
(3) Implant species
(4) Furnace gettering
(5) Effect of starting silicon parameters

As a result of this study, a processing procedure was defined which can be used to produce ion-implanted solar cells with up to 15% efficiency.

Section III gives a review of a comprehensive test program performed on state-of-the-art commercial screen-printable metallizing inks as well as RCA-formulated materials. Data are presented on the critical areas of electrical conductivity, solderability, and adhesion of the films as-fired into silicon surfaces. These properties were systematically evaluated as a function of ink composition and firing conditions. Analytical techniques were employed to assess metallization penetration into the shallow n-layer of solar cells; ink compositions and firing conditions were optimized to balance the physical and electrical requirements of the metallization for solar-cell applications.

A process for screen printing and infrared-lamp firing of silver inks for the front grid and back contact of 3-in.-diameter solar cells was developed, and performance data of these cells as a function of firing parameters and inks are given. The results of applying this process to ion-implanted solar cells are also presented.

Section IV discusses process development and optimization studies for low-cost spray deposition of single-layer antireflection (AR) coatings. These studies included effects of spray deposition machine parameters, metallization bondability after coating, cell electrical performance as a function of AR coating type, thickness, and heat-treatment effects.

The processing steps for a panel assembly process involving the lamination of a double-glass structure were developed. The procedures required to successfully laminate large panels are given in Section V.

Detailed process specifications for these processes were written and are available upon request from the Processes and Equipment Development Area of the JPL-LSA Project.

SECTION II

A STUDY OF THE FACTORS WHICH CONTROL THE EFFICIENCY OF ION-IMPLANTED SILICON SOLAR CELLS

A. BACKGROUND

Ion-implantation fabrication techniques are among the least expensive technologies for fabricating silicon solar cells. This study has investigated the ion-implant conditions and suitable post-implantation annealing steps which can be used to yield p-n junctions of sufficient quality to form efficient solar cells. When implantation is used to introduce dopant atoms into a substrate, not all of the atoms are initially electrically active, i.e., not all the atoms are located on substitutional lattice sites, and in addition, damage is introduced into the substrate lattice. High-temperature anneal steps (800 to 1000°C) are usually used to activate the implanted atoms and to reduce or eliminate the implant damage. These high-temperature steps can degrade the minority carrier diffusion length in the bulk of the wafer and, hence, can degrade the conversion efficiency of the resulting solar cell. This situation is aggravated by the fact that gettering effects which usually accompany diffusion processing are either minimal or are absent from the anneal procedures used on ion-implanted layers.

The solar cells made during the course of this experimental study were fabricated using the best quality silicon wafers available and using optimum masking, capping, and metallization techniques. The object was to minimize as much as possible the potential conflicting factors which may interfere with the study of implantation effects that might adversely affect the performance of implanted solar cells.

This section describes the results of experiments which were designed to investigate the factors which influence the performance of ion-implanted silicon solar cells. As a result of these experiments, a process specification was written and is available upon request from the Processes and Equipment Development Area of the JPL-LSA Project. This processing procedure can be used to produce solar cells with up to 15% conversion efficiencies. The factors which were investigated include: (1) implant dose, (2) implant energy, (3) implant species, (4) various processes for forming the backside contact layer and at the same time improving diffusion length in the bulk, (5) substrate orientation, and (6) substrate resistivity.

The performance of the solar cells was evaluated under standard AM-1 conditions by measuring the open-circuit voltage V_{cc}, the short-circuit current I_{sc}, and the maximum power values I_m and V_m for cells. From these data were calculated the values of the cell fill factor

$$FF = \frac{I_m V_m}{I_{sc} V_{oc}} \tag{1}$$

and conversion efficiency

$$\eta = \frac{I_m V_m}{\Phi A} \tag{2}$$

where Φ = 100 mW/cm^2 under standard AM-1 conditions and A is the area of the solar cell. These data, for the 182 cells fabricated. are presented in Appendix A.

In addition to the basic performance parameters, on selected cells the diffusion length was measured in the starting wafer, using a surface photovoltage technique [1], and in the finished cell, using curve-fitting techniques on the cell quantum efficiency data [2]. These diffusion lengths were used to evaluate the effectivcness of the anneal procedures employed in the fabrication of the cells.

The mask set used to fabricate the solar cells produces not only solar cells of various sizes (see Appendix B), but also produces diodes of various sizes so that both light and dark I-V curves could be constructed for selected cells. From these I-V curves, the values of the parameters in the diode equation [3]

$$J = J_{o1}\left(e^{qV/kT} - 1\right) + J_{o2}\left(e^{qV/nkt} - 1\right) \tag{3}$$

1. ASTM Tentative Test Method F391 for Minority Carrier Diffusion Length in Silicon by Measurement of Steady-State Surface Photovoltage, *1976 Annual Book of ASTM Standards*, Part 43, Electronics (1976).
2. The diffusion length L is obtained from a best parameter fit of the measured quantum efficiency data to the diffusion-only equations described by H. J. Hovel, "Solar Cells: Carrier Collection, Spectral Response and Photocurrent," Chapter 2 in *Semiconductors and Semimetals*, Vol. 11, Edited by Willardson and Beer.
3. A. S. Grove, *Physics and Technology of Semiconductor Devices*, (Wiley-Interscience, New York, 1967), Chapter 6.

$$\cong J_{o1} e^{qV/kT} + J_{o2}\, e^{qV/nkT} \quad \text{for } V >> \frac{kT}{q}$$

can be determined. The values of J_{o2} and n indicate the amount of residual damage left in the junction depletion region by the ion-implant fabrication process. In the experiments reported here, this residual damage was found generally to be small. The value of [3]

$$J_{o1} = q\, n_i^2 \left. \frac{D_n}{N_a L_n} \right|_{\text{bulk}} + \left. \frac{D_p}{N_D L_p} \right|_{\text{emitter}} \tag{4}$$

together with a knowledge of the diffusion length L_n in the bulk region can be used to estimate the effect of recombination in the ion-implanted emitter. For the cells constructed in this study, the recombination in the emitter is found generally to be negligible compared with the diffusion length effects associated with the bulk.

Table 1 presents a synopsis of the tests performed and the conclusions drawn from the various experiments. The major conclusions from the study are:

(1) Diffusion length in the bulk is the dominant factor in cell efficiency.

(2) Gettering and annealing techniques exist which can preserve or improve the diffusion length in the bulk, under implant anneal conditions.

(3) With regard to implantation, no effort was noted that limited cell performance.

In the following sections, the various tests listed in Table 1 will be described in detail.

B. PROFILES, JUNCTION DEPTHS, AND SHEET RESISTANCE OF ION-IMPLANTED SILICON SOLAR CELLS

A majority of the solar cells described in this report were fabricated using a 5-keV, ^{31}P implant to form the n^+ high-doped layer. This implant was performed using an Extrion Model 200-1000 implantation machine equipped with a standard 3-in. ferris wheel type endstation. This type of endstation uses an x-y mechanical scan to move the wafer through a stationary beam. The endstation operates in a batch processing mode and can implant 26 3-in. cells per batch.

TABLE 1. SYNOPSIS OF THE ION-IMPLANTED SOLAR-CELL EXPERIMENTS

Parameter Tested	Conclusion
Implant Parameter	
Implant Voltage	The optimum implant energy is in the 5- to 10-keV range.
Dose Level	The optimum dose level lies between 2×10^{15} and 4×10^{15} atoms/cm^2 (used in conjunction with a 5-μm-thick Ti-Al metallization system).
Species (^{11}B, ^{31}P, ^{75}As)	^{31}P in p-type wafers and ^{11}B in n-type wafer yield comparable results. There is no great advantage in using $^{31}P + ^{75}As$ for the n^+ layer.
Wafer Parameter	
Orientation <100> vs <111>	No difference observed.
Starting Wafer Resistivity	For ranges tested (1-2 ohm-cm and 8-12 ohm-cm), resistivity less important than achievable diffusion length after processing. Verified that V_{oc} decreases for increasing resistivity.
Starting Wafer Diffusion Length	Should be large and must not degrade with processing.
n-type vs p-type Starting Wafers	Can achieve slightly higher V_{oc} with p^+ implants into n-type starting wafers.
Anneal Temperature	With the Boron Glass Process B, anneal temperatures between 900 and 1050°C can be used to produce efficient cells.

TABLE 1. SYNOPSIS OF THE ION-IMPLANTED SOLAR-CELL EXPERIMENTS (Continued)

Parameter Tested		Conclusion
Measurement Techniques		
Cell Load Curves	Conversion Efficiency Fill Factor V_{oc} and I_{sc}	Used for basic cell performance evaluation.
Dark I-V Curves Illuminated I-V Curves		Can be used to find J_{o1} values which, in conjunction with bulk diffusion length measurements, can be used to evaluate performance of emitter layer.
Quantum Efficiency Measurements		Can be used to find bulk diffusion length after processing.
Diffusion Length Measurements in Starting Wafers		By comparing starting wafer diffusion length and post-processing bulk diffusion length, can monitor effect of processing on cell performance.

The 5-keV implant energy is achieved by deaccelerating the ions, which are extracted from a hot filament source at 35 keV, with a reversed gradient field in the multigapped "acceleration tube." The dose implanted at 5 keV is usually $2x10^{15}$ $^{31}P^+$ ions/cm^2.

The profiles* which can be expected at 5 keV are shown in Figs. 1 and 2. Figure 1 also shows the profiles which can be expected when selected energies from 5 to 100 keV are used. The wafers with the profiles given in Fig. 1 have received a 900°C anneal in flowing N_2 for 30 min. (The performance of the solar cells resulting from these implants will be discussed in a later section.) The profiles given in Fig. 2 were not annealed and are included in order to show the nature of the 5-keV profile near the surface; Fig. 2 also shows a 5-keV ^{11}B implanted profile.

An analysis of the junction depths of the n^+ layers achievable with various implant energies used in conjunction with the 900°C, 30-min anneal sequence is shown in Fig. 3. The measured depths are anomalously deeper than would be expected from a simple diffusion redistribution of the as-implanted profile. The shape of the curve is also not characteristic of profiles obtained from simple diffusion redistribution of ion-implanted profiles [4]. The shape is more characteristic of concentration-enhanced diffusion, which is very likely to be present since the density at the peak of the as-implanted profile ($5.65x10^{20}/cm^3$) exceeds the solid solubility of ^{31}P in silicon at 900°C ($\bar{N}_{max} = 4x10^{20}/cm^3$). Lowering the dose to avoid concentration-enhanced diffusion causes a deterioration in the cell's efficiency. (This dose effect will be discussed in a later section.) The sheet resistance of the various layers implanted at different energies is given in Fig. 4. The dose of $2x10^{15}/cm^2$ at 5 keV which yields near-optimum cell efficiency produces an n^+ layer, after the anneal step, having a sheet resistance of 65 Ω/□.

The backside p^+ contact layer of the n^+pp^+ solar-cell structure was formed in one of two ways. Process A consists of implanting a 25-keV, ^{11}B layer on the backside of the wafer and then performing a three-step anneal which consists of heating the wafer at 550°C for 2 h in flowing N_2, then

*The profile measurements were obtained using SIMS (secondary ion mass spectropscopy) analysis.

4. E. C. Douglas and A. G. F. Dingwall, "Ion Implantation for Threshold Control in COSMOS Circuits," IEEE Trans. Electron Devices ED-21, 324 (1974).

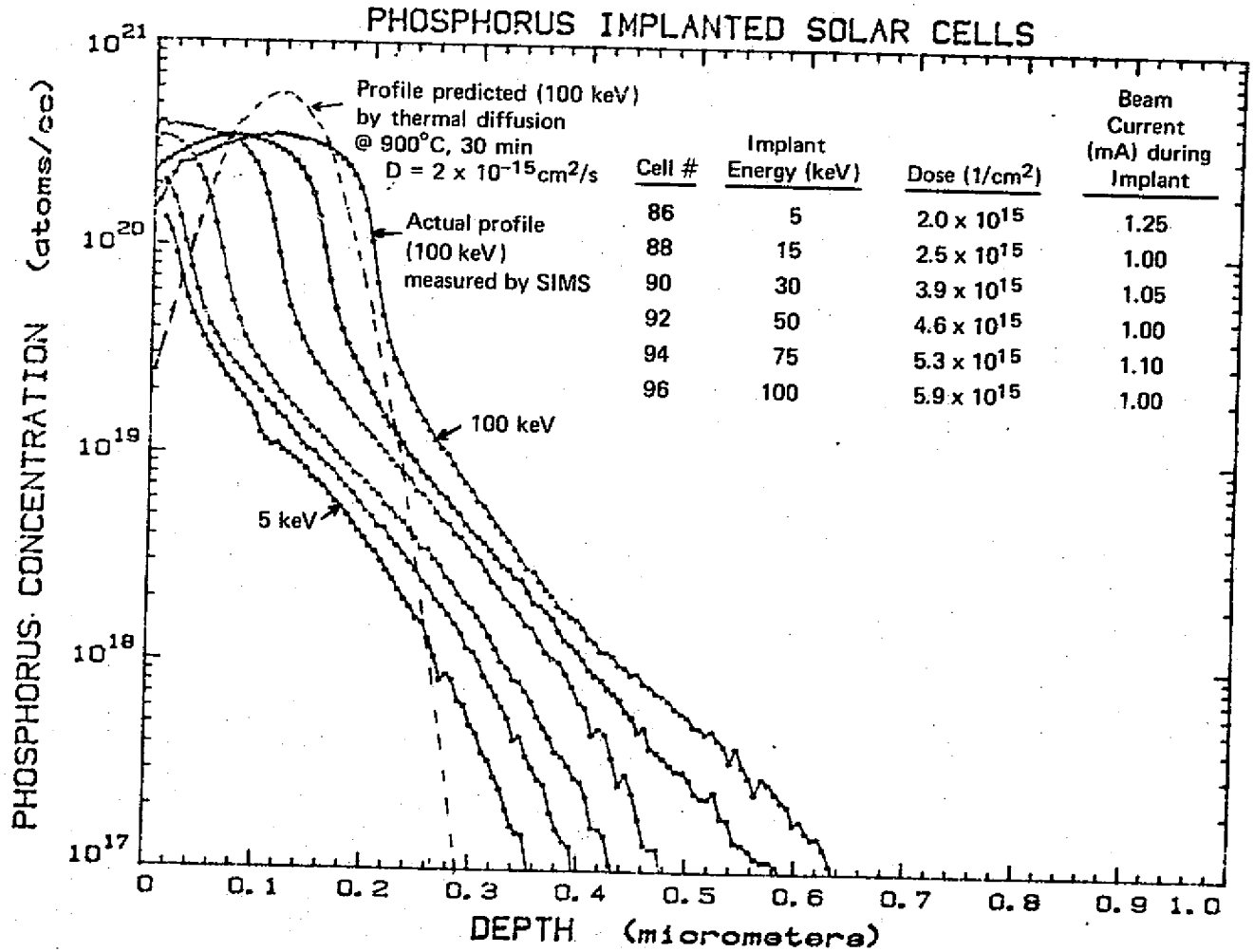

Figure 1. SIMS profile of ion-implanted ^{31}P layers that were used as the n^+ layer in silicon solar cells. The layers were annealed for 30 min at 900°C in flowing N_2.

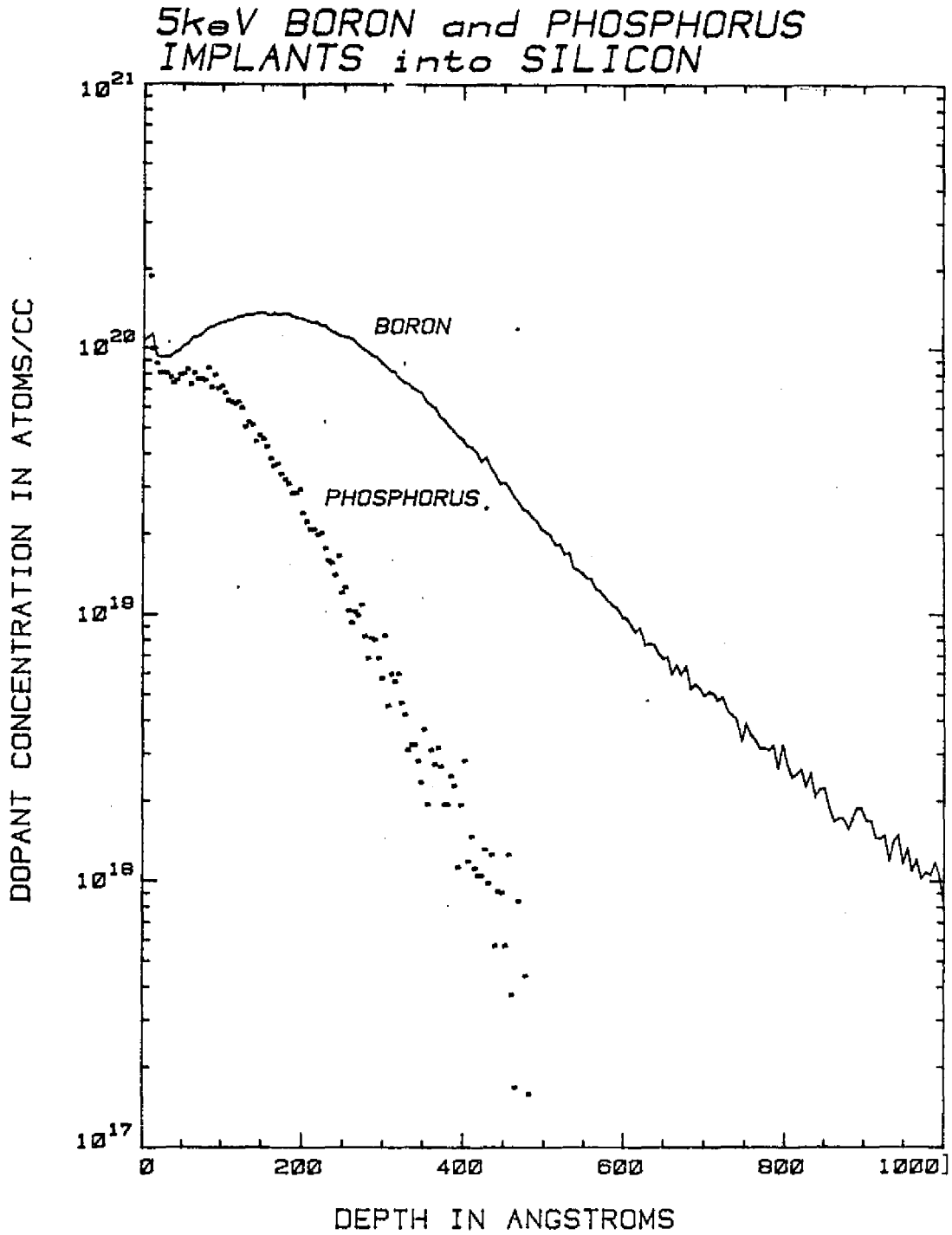

Figure 2. SIMS profiles of 5-keV ion-implanted ^{31}P and ^{11}B. These layers have received no heating steps and represent the as-implanted profiles.

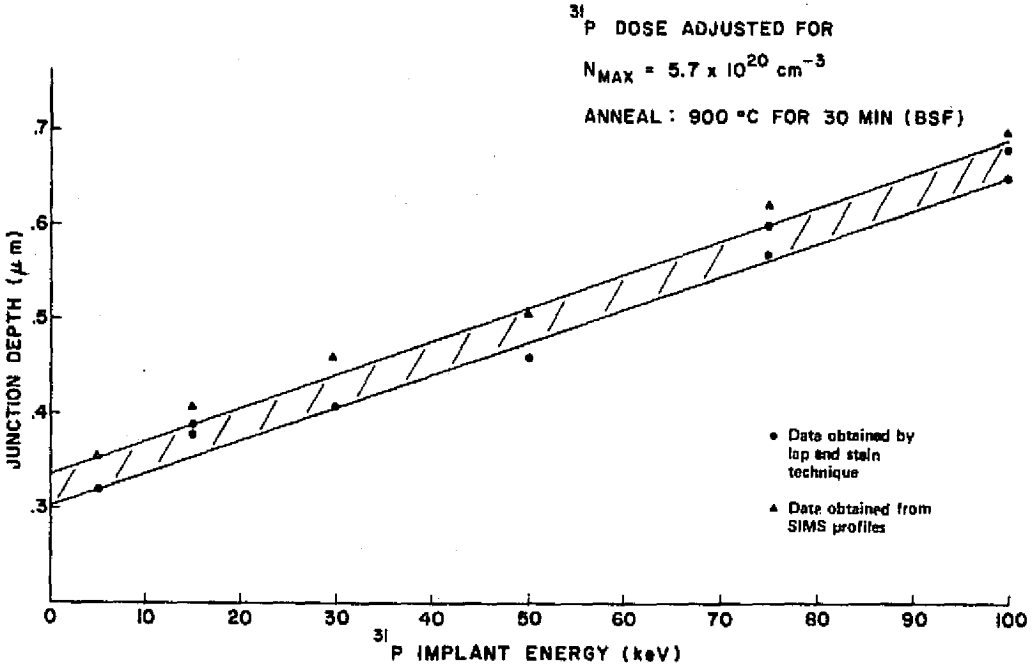

Figure 3. Results of junction depth measurements on ion-implanted layers annealed at 900°C for 30 min in flowing N_2.

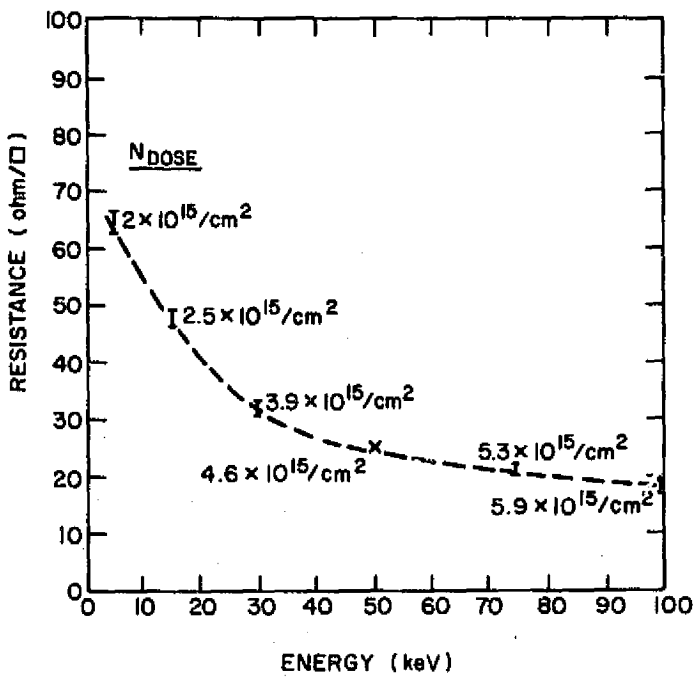

Figure 4. Results of sheet resistance measurements on ion-implanted layers annealed at 900°C for 30 min in flowing N_2. After anneal, the peak values in the layer profile are 3 to 4 x 10^{20} atoms/cm^3.

increasing the temperature to 850°C and heating for 15 min in flowing N_2, and then reducing the temperature back to 550°C and heating for another 2 h in flowing N_2. The second backside doping procedure, Process B, consists of depositing a boron glass layer on the backside of the wafer using a wet boron nitride transfer process* and then performing a 900°C drive-in anneal step for 30 min in flowing N_2. This procedure produces a layer having a sheet resistance of ∿50 Ω/□ and having the profile given in Fig. 5. It will be shown in a later section that both backside doping processes are capable of preserving or increasing the diffusion length in the bulk of the solar cell.

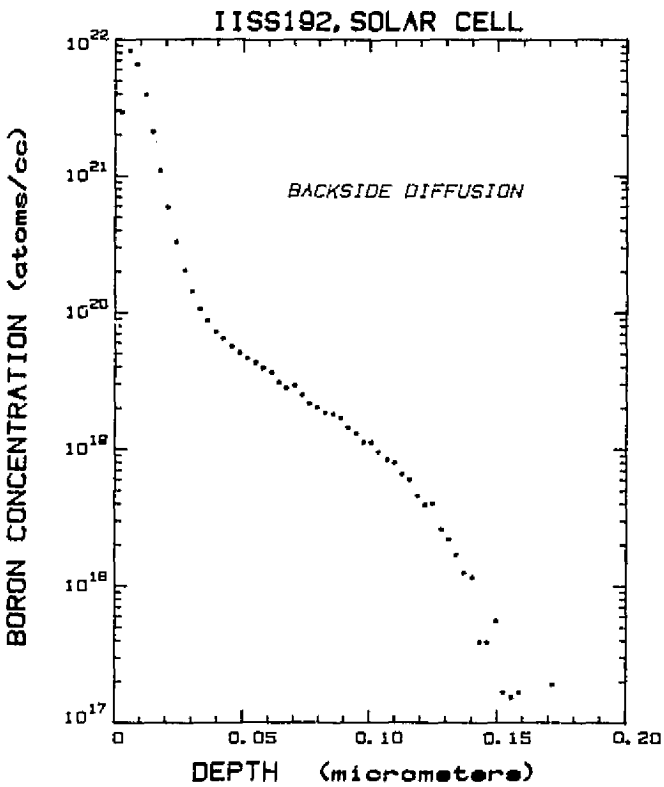

Figure 5. SIMS profile of the backside layer formed by wet boron nitride transfer process B.

C. PRESERVING AND IMPROVING THE DIFFUSION LENGTH IN ION-IMPLANTED SILICON SOLAR CELLS

Initial experiments in fabricating ion-implanted silicon solar cells used 950°C anneal steps and used low temperature (875°C) grown oxide or CVD oxides

*See subsection C.1 below

as capping layers. Analysis of the resulting cells (S1 to S5, IISS11,12 in Appendix A) showed conversion efficiencies (with spin-on AR coatings) which ranged between 8.7 and 12.6%. Measurement of the bulk lifetime in these samples, using the diode reverse recovery technique [5] on test diodes incorporated on the same solar-cell wafer (see Appendix B) revealed that the minority carrier electron lifetime in the base region of these cells ranged from 0.5 to 2.1 μs, with the lowest lifetimes correlating with the poorest conversion efficiencies. This result indicated that a method was needed for improving the minority carrier lifetime in the base region of the solar cells.

1. Boron Glass (BG) Backside Gettering

A technique for fabricating high efficiency p^+n solar cells [6] involves the use of a p^+ layer formed using a wet boron nitride [7,8,9] transfer doping process, and this technique was used to form the backside contact layers on the n^+p ion-implanted cells. Initial tests with the boron glass (BG) backside doping process produced cells with conversion efficiencies between 12.3 and 13.9% (see cells IISS14 to IISS26 in Appendix A). Cells with the BG processing displayed minority carrier lifetimes which were on average more than an order of magnitude higher (9.8 to 17.8 μs) than the earlier cells; a comparison of the quantum efficiency curves for cells made with and without the BG deposited on the backside (see Fig. 6) showed that the contributions of the deeply absorbed

5. R. H. Kingston, "Switching Time in Junction Diodes and Junction Transistors," Proc. IRE 42, 829 (1954). Also see B. Lax and S. F. Neustadter, "Transient Response of a P-N Junction," J. Appl. Phys. 25, 1148 (1954), and R. H. Dean and C. J. Nuese, "A Refined Step-Recovery Technique for Measuring Minority Carrier Lifetimes and Related Parameters in Asymmetric P-N Junction Diodes," IEEE Trans. Electron Devices ED-18, 151 (1971).
6. M. S. Bae and R. V. D'Aiello, "P^+/N High-Efficiency Silicon Solar Cells," Appl. Phys. Lett. 31, 285 (1977).
7. D. R. Rupprecht and J. Stach, "Oxidized Boron Nitride Wafers as an In-Situ Boron Dopant for Silicon Diffusions," J. Electrochem. Soc. 120, 1266 (1973).
8. J. Stach and J. Kruest, "A Versatile Boron Diffusion Process," Solid State Technol. 19, 60 (October 1976).
9. Technical Note, "Hydrogen Injection Process Low Temperature 725°C-975°C," Form C715, June 1978, The Carborundum Co., Graphite Products Division, P.O. Box 577, Niagara Falls, New York 14302.

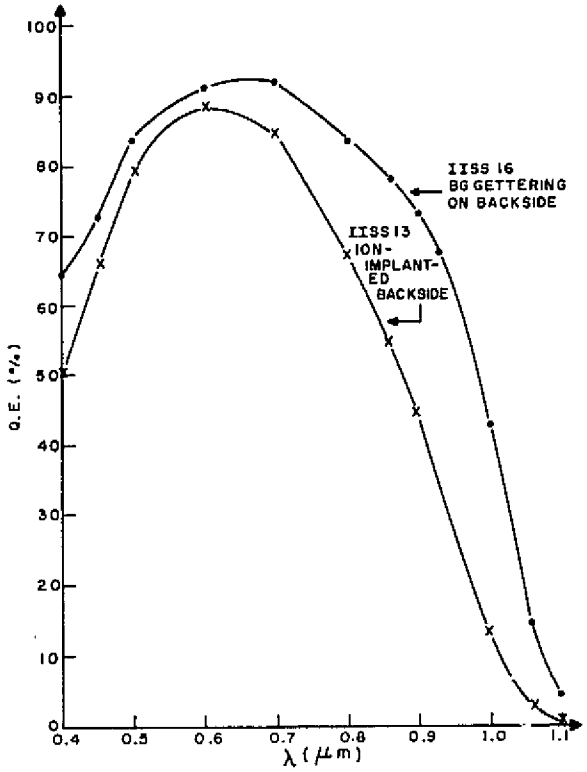

Figure 6. Quantum efficiency curves for a cell made with boron glass (BG), formed by the wet boron nitride transfer process, and ion-implanted boron as the source for the backside p^+ layer. Both cells were annealed at 900°C for 30 min in flowing N_2.

wavelengths were higher for the cells made using the BG backside step. This improvement in lifetime τ (or equivalently in diffusion length $L = \sqrt{D\tau}$ where D is the minority carrier diffusion length which is dependent on the wafer background doping level) indicates that the diffused boron p^+ layer accomplished gettering in much the same fashion as diffused phosphorus layers. The exact nature of the gettering process in the case of the BG layer, however, is not yet known.

A careful measurement of the diffusion lengths in selected cells made with the BG backside doping process (Table 2) showed that the diffusion lengths in the cells after BG processing (205 to 278 μm) are significantly higher than the diffusion length observed in the starting wafers. The values observed for the diffusion length in Wacker* float zone starting wafers were between 100 and 160 μm (see Appendix A, cells IISS147 to IISS160).

*Wacker Chemical Corp., Richardson, TX.

TABLE 2. DIFFUSION LENGTH MEASUREMENTS IN ION-IMPLANTED SOLAR CELLS

Cell	^{31}P, 5-keV Dose	BG on Backside Anneal Temp. 30 min (°C)	L_p (μm) (SPV)†	L_p (μm) DRR†† (D=30)	L_p (μm) QE meas†††
IISS15 WAC1-3*	$1.5x10^{15}$	900	270	149	201
IISS20 WAC1-3	$5x10^{14}$	1000	210	212	274
IISS21 WAC1-3	$7.5x10^{14}$	1000	205	231	278
IISS23 MON1-3**	$7.5x10^{14}$	900	140	191	254
IISS26 MON1-3	$1.5x10^{15}$	1000	150	171	245

*1-3 Ω-cm Wacker float zone wafers, 2 in., <100>.
**1-3 Ω-cm Monsanto Co., St. Peters, MO, Czochralski wafers, 3 in., <100>.
†SPV - Diffusion length measured using the surface photovoltage method.
††DRR - Diffusion length measured using the diode reverse recovery method.
†††QE - Diffusion length measured by fitting the theoretical quantum efficiency curve to the data. L_p is a fit parameter.

The wet boron nitride transfer process differs from earlier processes involving boron nitride wafers in both transfer temperature and background ambient. By introducing and controlling the amount of water vapor in the gas stream, the material HBO_2 is formed and transferred to the silicon solar-cell wafer [8]. HBO_2 has a much higher vapor pressure than the B_2O_3 material which is transferred in the absence of water vapor. The transfer of HBO_2 in a wet ambient can be accomplished at 800°C, a temperature at which no boron diffusion will occur into the silicon. Thus, the transfer process only produces a boron source glass; no uncontrolled diffusion occurs. To achieve the same vapor pressure of transfer material B_2O_3 in a dry transfer process would require a temperature of ∿1200°C. The amount of H_2O in the ambient gas stream must be

carefully controlled so that the glass can be removed easily at the end of the process. This is accomplished by using a ∿10% H_2:N_2 forming gas mixture to which is added a controlled amount of O_2. The amount of H_2O which forms in the gas stream is thus dependent on the O_2 flow rate. (An alternate procedure is to use an N_2:O_2 ambient mixture to which is added a controlled amount of H_2.)

After depositing the boron glass layer (BG) at 800°C, the wafer is placed in a furnace at the desired drive-in anneal temperature. The p^+ layer on the backside and the ion-implanted n^+ layer on the front side are simultaneously annealed. Excess glass is then removed in buffered HF. After the removal step, a boron-rich layer remains on the surface as evidenced by the fact that the backside remains hydrophilic while the front side, which was protected from boron deposition by a CVD SiO_2 layer, becomes hydrophobic. The residual boron-rich layer, however, is conductive and presents no contacting problem. If too much O_2 is used during the transfer process, an excessively thick layer of boron glass will form which results in an undesirable yellow-stained surface after the buffered HF removal step. When the wafers come out of the 800°C deposition step, they should have a pale blue color.

It has been observed that the boron nitride wafers must be periodically oxidized (it is the B_2O_3 layer on the surface that is the transfer source, not the BN) and that the furnace must be allowed to clean itself through use if the gettering effect is to be achieved. It can be seen from the data in Appendix A that the cells after IISS83, as well as the first attempt at 3-in. solar cells (IISS45 to IISS52), do not display efficiencies as high as those before IISS83. All these cells were made with the same BG processing. Cells before IISS83 were processed in a 2-in. boron nitride transfer furnace while those after IISS83 were processed in an upgraded 3-in. BG furnace which had not achieved the required degree of cleanliness during our use of it. Subsequent tests in newly set-up BG transfer furnaces indicate that a period of furnace cleaning-by-use is required for the gettering to become effective.

2. Three-Step Annealing

A second backside processing procedure, the three-step anneal [10] procedure which is carried out after the wafer has been implanted on both sides, has also been used to produce efficient solar cells. Wafers IISS72 to 77, IISS126 to 132, IISS140 to 146 and IISS154 to 160 showed a significant improvement in bulk diffusion length after the front side n^+ implant and the backside p^+ implant had been performed, followed by the three-step anneal sequence. Again the exact reason for the increase in diffusion length is not known. The long low-temperature steps followed by the short high-temperature step nicely anneals the implanted dopant atoms; but the accompanying phenomenon which leads to longer minority carrier diffusion lengths is not obvious. We can speculate, based on the observations of Helmreich and Sirtl [11], that optimum conditions in the crystal lattice are established by the long low-temperature heating steps.

Both the three-step annealing process A and the backside boron glass (BG) procedure B are capable of preserving or increasing the diffusion length in the bulk region of the wafer. The BG process B has the advantage that it allows annealing steps in the 900 to 1000°C temperature range to be carried out (see cells IISS54 to 65) without sacrificing cell efficiency. The BG process B also requires only 65 min of process time for deposition and anneal. On the other hand, the BG process B has the disadvantage that the front side must be capped during the BG deposition. The three-step anneal procedure A has the advantage of being an all ion-implanted procedure which can be performed with no capping layer. It has the disadvantage of requiring 250 min of furnace time.

---

10. A. Kirkpatrick, "Process Specification for High Efficiency Implanted 3" Diameter Cells," Proceedings: 9th Project Integration Meeting, LSA Low Cost Solar Array Project, JPL, April 11-12, 1978. (See page 4-104 of Proceedings.)
11. D. Helmreich and E. Sirtl, "Oxygen in Silicon: A Modern View," Semiconductor Silicon 1977, Proceedings of the 3 rd International Symposium on Silicon Materials Science and Technology, The Electrochemical Society, Inc., P.O. Box 2071, Princeton, NJ 08540. (Article located on Pages 626 to 636.)

D. SOLAR-CELL PERFORMANCE AS A FUNCTION OF DOSE AND ANNEAL CYCLE

A series of experimental solar cells were fabricated, with different dose values for the 5-keV implanted ^{31}P atoms, to determine the optimum dose value. The results of the experiment using the boron glass backside annealing process B is shown in Figs. 7 through 10 where the annealing has been performed at both 900 and 1000°C for 30 min. It can be seen from Fig. 7 that the efficiency of both 900 and 1000°C annealed samples peaks in the dose region between $2x10^{15}/cm^2$ and $5x10^{15}/cm^2$. The fall-off at lower dose value is caused by a decrease of both V_{oc} and fill factor FF as the dose is lowered (see Figs. 9 and 10). Increased n^+ sheet resistance and decreased junction poter tial contribute to this fall-off. Notice from Fig. 8 that the short-circuit current is relatively insensitive to the dose level. This indicates that J_{sc} is dominated by bulk effects which are relatively unaffected by the formation of the n^+ layer by implantation as long as diffusion length in the bulk is preserved or increased during the anneal cycle.

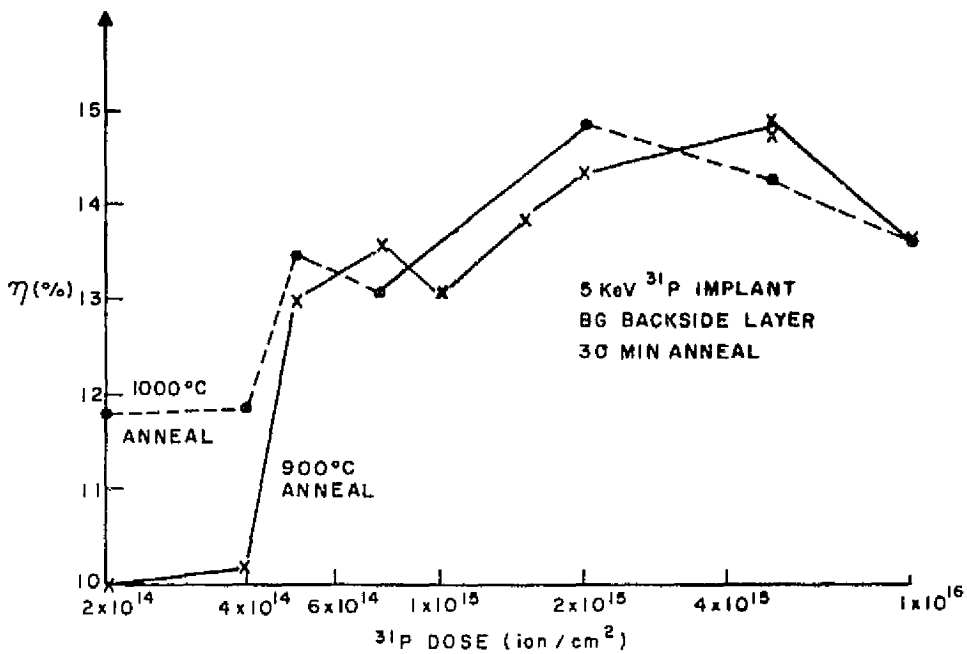

Figure 7. A plot of the conversion efficiency of solar cells made with 5-keV ^{31}P implanted at different dose levels. Boron glass process B was used during the anneal cycle which was carried out at 900 and 1000°C.

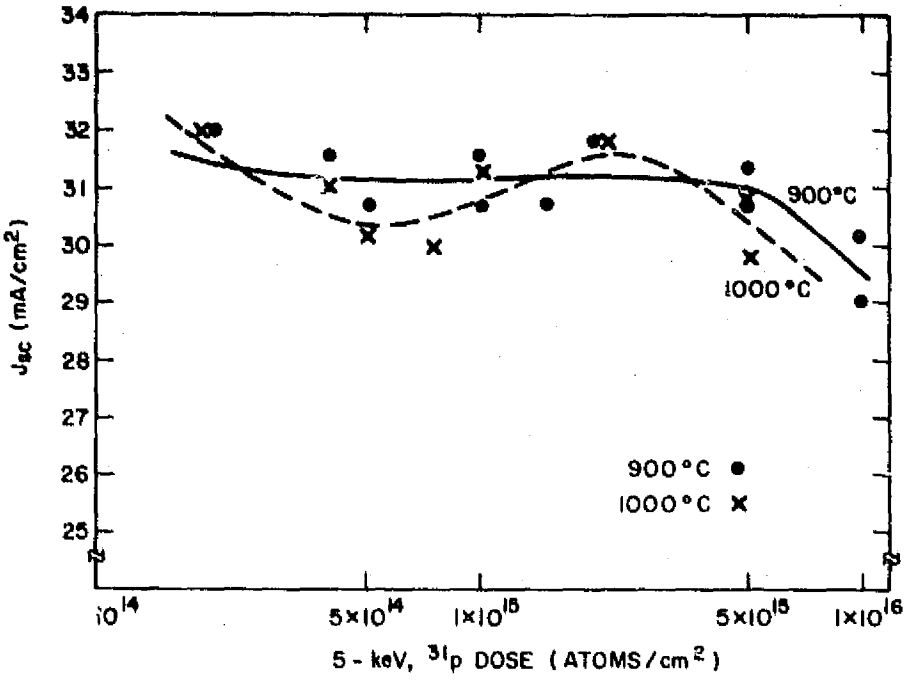

Figure 8. A plot of the short-circuit current density of solar cells made with 5-keV ^{31}P implanted at different dose levels. Boron glass process B was used during the anneal cycle which was carried out at 900 and 1000°C.

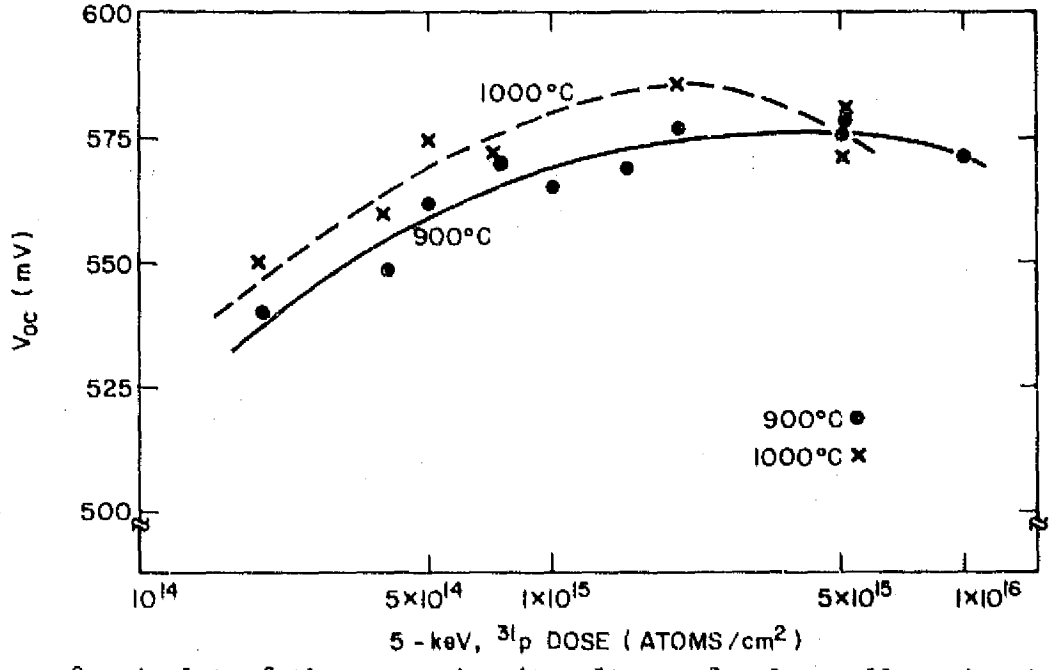

Figure 9. A plot of the open-circuit voltage of solar cells made with 5-keV ^{31}P implanted at different dose levels. Boron glass process B was used during the anneal cycle which was carried out at 900 and 1000°C.

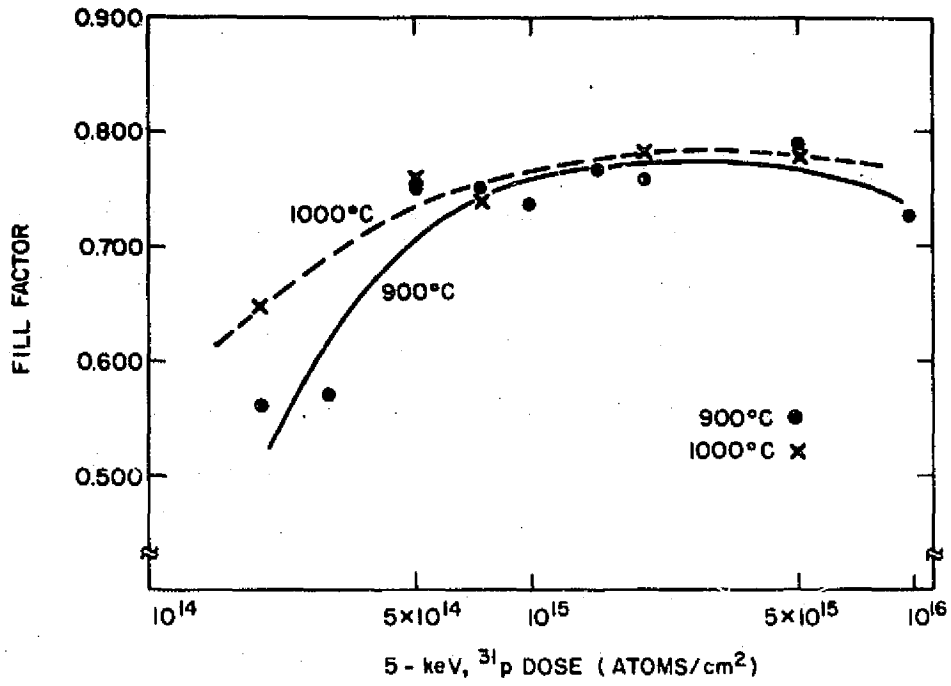

Figure 10. A plot of the fill factor of solar cells made with 5-keV ^{31}P implanted at different dose levels. Boron glass process B was used during the anneal cycle which was carried out at 900 and 1000°C.

The effect of using either the three-step anneal process A or the boron glass process B on samples fabricated using different dose levels is shown in Fig. 11. The three-step anneal process and the boron glass process yield comparable results at the optimum dose levels of $2x10^{15}$ to $5x10^{15}$ atoms/cm^2. As can be seen from Fig. 12, however, the open-circuit voltage for all dose levels tested tends to increase with the anneal temperature; this is also evident in Fig. 9. It appears that at lower dose levels the three-step process suffers from insufficient annealing. It also appears that it is desirable to anneal the samples at the highest temperature that does not degrade the diffusion length in the bulk. The boron glass anneal process B has the advantage of preserving or increasing the diffusion length when anneal temperatures as high as 900 to 1000°C are used.

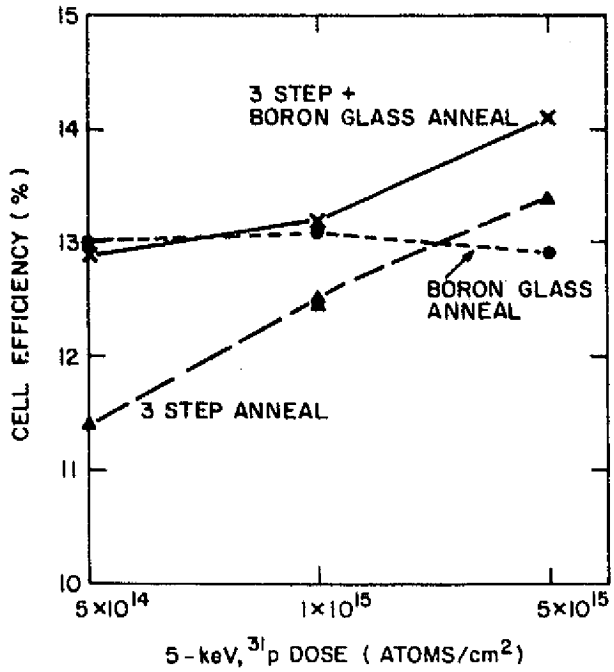

Figure 11. A plot of the conversion efficiency of solar cells made with 5-keV ^{31}P implanted at different dose levels. The anneal was performed using either the three-step anneal process A, the boron glass process B at 900°C, or a combination of the two.

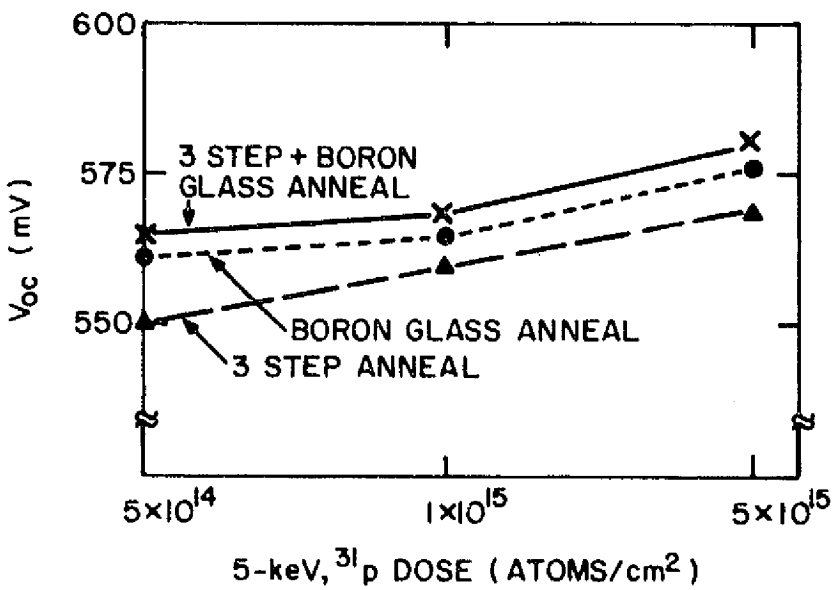

Figure 12. A plot of the open-circuit voltage of solar cells made with 5-keV ^{31}P implanted at different dose levels. The anneal is performed using either the three-step anneal process A, the boron glass process B at 900°C, or a combination of the two.

E. SOLAR-CELL PERFORMANCE AS A FUNCTION OF IMPLANTED SPECIES

N^+p cells were fabricated using 5-keV ^{31}P, 5-keV ^{75}As, and a combination of 5-keV ^{31}P + 5-keV ^{75}As to form the n^+ layer. The cells received anneal cycles, using the boron glass process B, ranging from 900 to 1050°C. The conversion efficiencies of the resulting cells, as a function of implanted dose, are given in Figs. 13 and 14. The cells tend to peak in efficiency in the same range ($2x10^{15}$ to $5x10^{15}/cm^2$) as observed in the previous experiments. We have observed that higher temperature anneal steps are needed to produce efficient ^{75}As implanted cells. A third conclusion to be drawn is that the presence of both ^{31}P and ^{75}As in the n^+ layer of the cell does not significantly improve the conversion efficiency. It has been reported in the

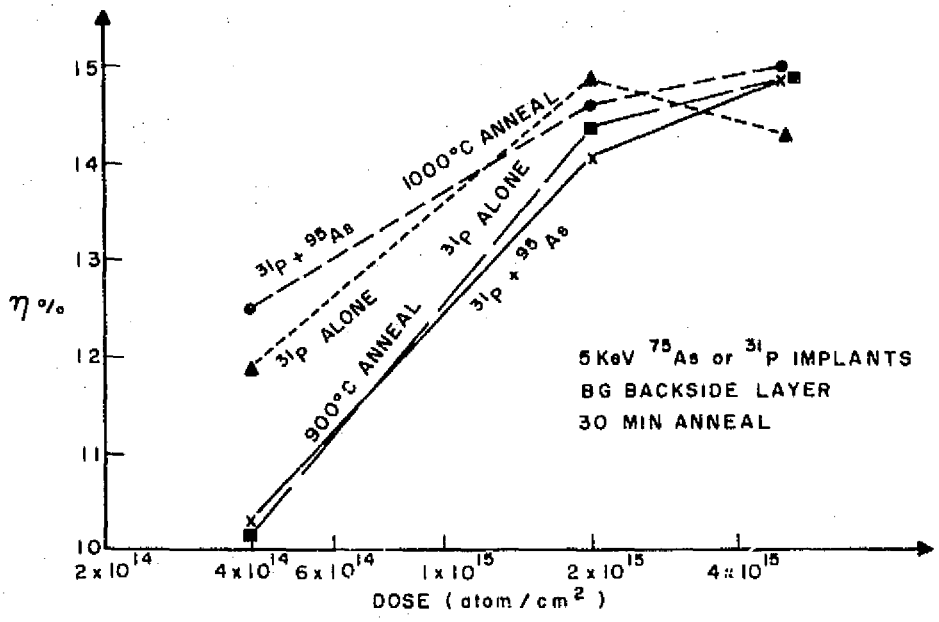

Figure 13. A plot of the conversion efficiencies of solar cells implanted with ^{31}P alone and cells implanted with both ^{31}P and ^{75}As to form the n^+ layer.

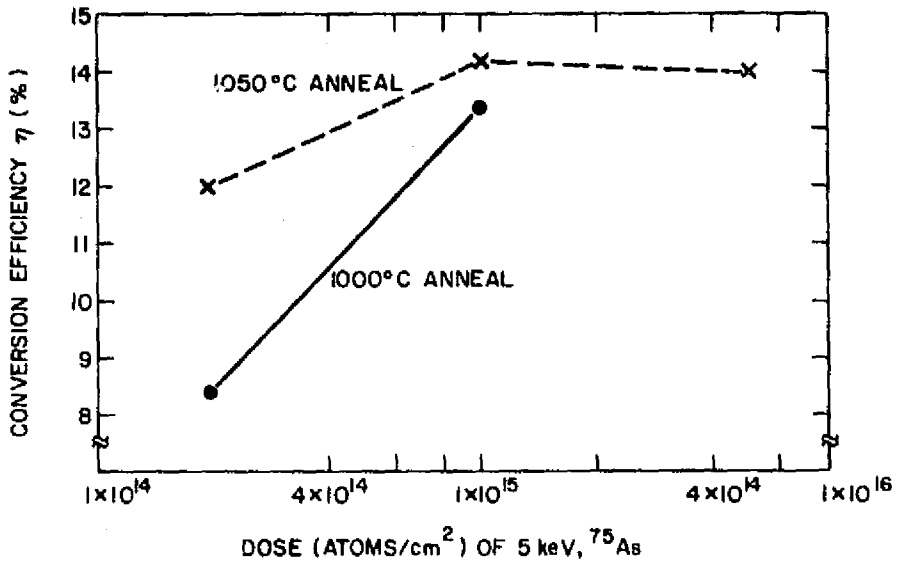

Figure 14. A plot of the conversion efficiencies of cells implanted with ^{75}As to form the n^+ layer. The backside layer of the cells was formed using the boron glass process B and the cells were annealed at 1000 or 1050°C for 30 min.

literature [12,13] that the use of both ^{31}P and ^{75}As in the emitters of bipolar transistors can reduce dislocation formation and improve the emitter characteristics. This effect does not appear to be of significance in our implanted solar cells.

p^+n cells were also fabricated using ion-implanted ^{11}B at 5 keV. The n^+ backside layer of these cells was formed by depositing CVD phosphorus-doped oxide and performing both the front side anneal and the backside diffusion at

12. M. Watanabe, H. Muraoka, and T. Yonezawa, "Perfect Crystal Technology," Proceedings of the 6th Conference on Solid State Devices, Tokyo, 1974, Supplement to the Journal of the Japan Society of Applied Physics, Vol. 44, 269 (1975).
13. T. Yonezewa, M. Watanabe, Y. Koshino, H. Ishida, H. Muraoka, and T. Ajina, "High Concentration Diffusion without Generation of Crystal Defects," Proceedings of the Third International Symposium on Silicon Materials Science and Technology, Philadelphia, PA 1977. *Semiconductor Silicon 1977*, Vol. 77-2, p. 658, The Electrochemical Society, Princeton, NJ.

the same time. A known gettering effect [14] is achieved with this type of phosphorus treatment. Table 3 shows the performance of the p^+n cells, annealed at two different temperatures, compared with the best of the n^+p cells. Although the conversion efficiency, the short-circuit current, and the fill factors are comparable for the two types of cells, the open-circuit voltage of the p^+n structures is consistently higher than the open-circuit voltage of the n^+p cells.

F. SOLAR-CELL PERFORMANCE AS A FUNCTION OF IMPLANT ENERGY

Solar cells were made using different implant energies (see cells IISS85 to IISS96 in Appendix A) for the implantation of ^{31}P to form the n^+ layer. The profiles of the cells are given in Fig. 1, and the performance of the cells is plotted as a function of energy in Figs. 15 and 16. The boron glass process B was used during the anneal step which was carried out at 900°C for 30 min.

The fill factor and the open-circuit voltage of these cells is nearly independent of energy because the cells were designed to have the same peak concentration in the emitter. The short-circuit current of the cells, however, is a decreasing function of implant energy and this causes the conversion efficiency of the cell to drop with increasing implant energy. The reason for this loss of conversion efficiency is the drop in quantum efficiency at lower wavelengths with increasing implant energy (i.e., increasing junction depth) as shown in Fig. 17 where the quantum efficiency at four different wavelengths is plotted as a function of energy. Except for the slight initial increase in quantum efficiency for the two lower wavelengths, an effect which is probably associated with near surface damage produced by the lowest implant energies, the quantum efficiency generally decreases with increasing energy. For longer wavelengths, the quantum efficiency tends to remain constant with increasing energy until the ratio of the layer depth to the absorption depth reaches a particular value. For deeper layer depths, the quantum efficiency begins a rapid decrease.

---

14. A Goetzberger and W. Shockley, "Metal Precipitates in Silicon P-N Junctions," J. Appl. Phys. 31, 1821 (1960). See also M.N. Nakamura and T. Kato, "A Study of Gettering Effect of Metallic Impurities in Silicon," Japan J. Appl. Phys. 7, 512 (1968) and E. L. MacKenna, "Silicon and Silicon Dioxide Gettering in Perspective," Extended Abstract No. 216, Electrochem. Soc. Vol. 74-2, October 1974.

TABLE 3. A COMPARISON OF THE PERFORMANCE OF n^+p AND p^+n ION-IMPLANTED SOLAR CELLS

Cell	Structure*	Species	Dose	Anneal Temp (°C)	η (%)	J_{sc} (mA/cm^2)	V_{oc} (mV)	FF
IISS60	n^+p	^{31}P	2.0×10^{15}	900	14.4	31.9	577	0.760
IISS61	n^+p	^{31}P	2.0×10^{15}	1000	14.9	31.9	587	0.780
IISS36	n^+p	^{75}As	1.0×10^{15}	1050	14.2	31.3	578	0.760
IISS38	n^+p	^{75}As	5.0×10^{15}	1050	14.0	30.7	580	0.760
IISS62	n^+p	$^{31}P+^{75}As$**	2.5×10^{15}	900	14.9	31.8	583	0.780
IISS63	n^+p	$^{31}P+^{75}As$**	2.5×10^{15}	1000	15.0	31.1	590	0.730
IISS107	p^+n	^{11}B	2.0×10^{15}	900	14.9	31.6	601	0.760
IISS108	p^+n	^{11}B	2.0×10^{15}	900	14.4	31.0	600	0.751
IISS109	p^+n	^{11}B	2.0×10^{15}	1000	14.7	31.0	600	0.766
IISS110	p^+n	^{11}B	2.0×10^{15}	1000	14.5	31.1	600	0.755

*The n^+p cells were made with 1 to 3 ohm-cm, p-type starting substrates. The boron glass process B was used during the anneal cycle.
The p^+n cells were made with 1 to 2 ohm-cm, n-type starting substrates. The backside layer was formed using a phosphorus-doped CVD oxide as the diffusion source.
All the cells were annealed for 30 min.

**Equal amounts of each dopant.

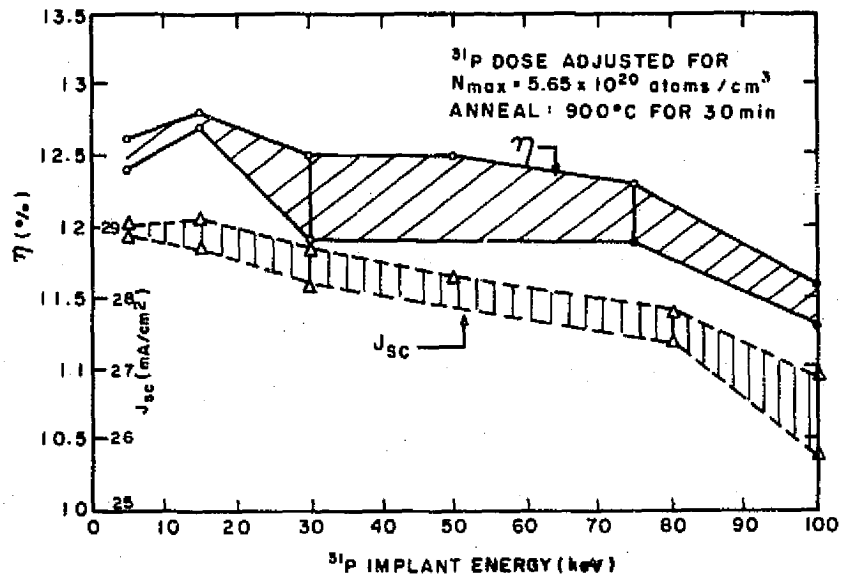

Figure 15. A plot of the conversion efficiency and the short-circuit current for ^{31}P implanted solar cells made with various implant energies. The boron glass process B was used during the 900°C - 30-min anneal cycle.

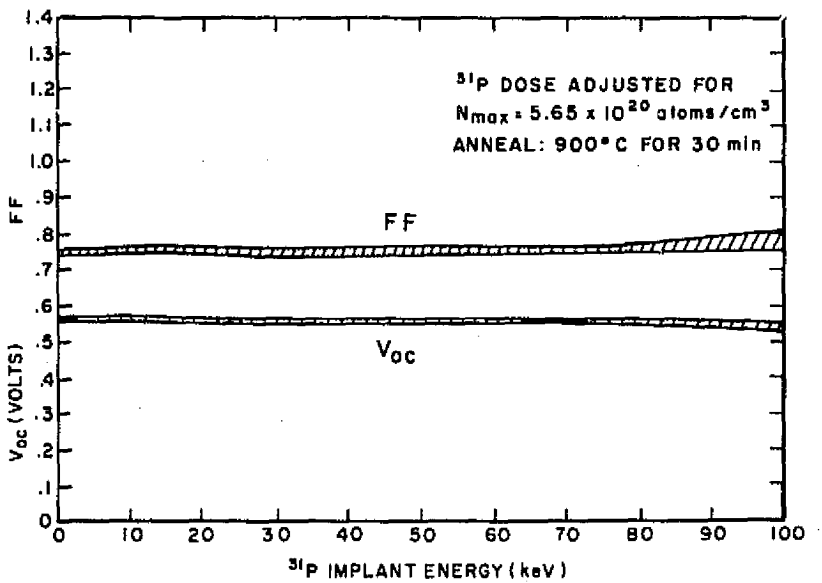

Figure 16. A plot of the open-circuit voltage and fill factor for ^{31}P implanted solar cells made with various implant energies. The boron glass process B was used during the 900°C - 30-min anneal cycle.

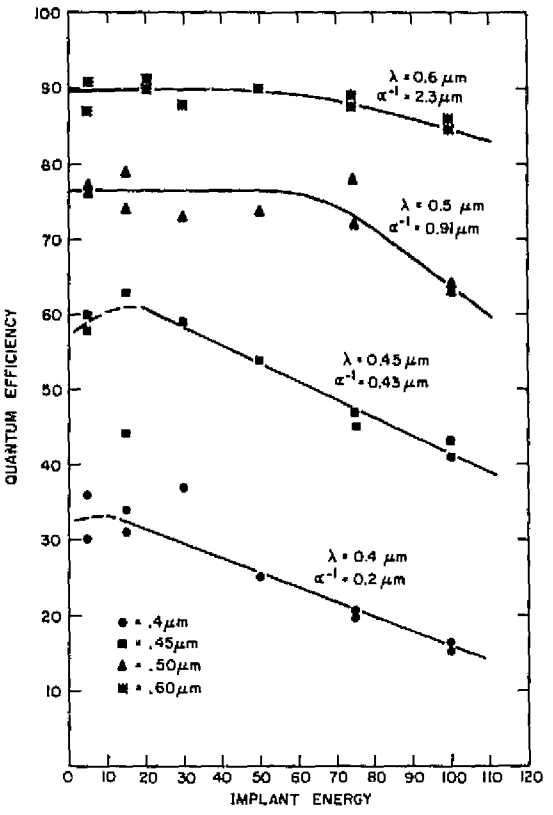

Figure 17. A plot of the quantum efficiency of the ^{31}P implanted solar cells as a function of the implant energy for various wavelengths of incident light. a^{-1} is the absorption depth in silicon for the given wavelength.

G. SOLAR-CELL PERFORMANCE AS A FUNCTION OF SUBSTRATE RESISTIVITY, SUBSTRATE ORIENTATION, AND SUBSTRATE DIFFUSION LENGTH

Solar cells were fabricated using different starting wafer resistivities and different starting wafer orientations. The results of these experiments are given in Table 4. The samples were measured without AR coating, which is part of the reason for the low conversion efficiencies. Measurements were also made of the diffusion lengths in the wafers before and after processing of the cells. Surface photovoltage (SPV) measurements of the diffusion length after processing were made on a region near the solar cell which was not covered by an n^+ junction. The reason for the low values of diffusion length observed in the finished cells, and, hence, a second reason for the low conversion efficiences, is, as mentioned in Section III.C, that the furnace used during the

TABLE 4. MEASUREMENTS OF SOLAR-CELL PERFORMANCE AS A FUNCTION OF WAFER ORIENTATION AND RESISTIVITY

Cell	Wafer Doping (ohm-cm)	Orientation	SPV Diffusion Length before Processing (μm)	SPV Diffusion Length After Processing (μm)	Diffusion Length for Parmeter Fit to QE Data After Processing (μm)	η (%)	J_{sc} (mA/cm^2)	V_{oc} (mV)	FF
IISS97	WAC* 1-4	<100>	110	110	89	8.8	20.2	552	.786
IISS98	WAC* 1-4	<100>	110	100	100	8.9	20.5	553	.785
IISS99	WAC 1-4	<100>	100	70	109	8.9	20.5	556	.781
IISS100	WAC† 8-12	<100>	130,90	110	115	8.4	20.9	520	.774
IISS102	WAC† 8-12	<100>	100	350	106	8.3	20.9	516	.771
IISS103	WAC[1] 8-12	<111>	100,90	130	107	8.3	20.8	514	.774
IISS104	WAC[1] 8-12	<111>	110,100	210	150	8.3	20.6	524	.773
IISS119	MON* 8-15	<100>	120	-	23	7.8	20.0	510	.769
IISS120	MON* 8-15	<100>	105	-	83	8.2	20.7	518	.768
IISS133	MT† 1.5	<100>	110	-	80	8.6	20.1	550	.777
IISS134	MT† 1.5	<130>	130	-	71	8.5	20.0	546	.777

WAC* - Wacker Floatzone Wafers, 1-4 ohm-cm, <100>, p-type, 10-12 mil thick, 2-in. diam

WAC† - Wacker Floatzone Wafers, 8-12 ohm-cm, <100>, p-type, 10-12 mil thick, 2-in. diam

WAC[1] - Wacker Floatzone Wafers, 8-12 ohm-cm, <111>, p-type, 10-12 mil thick, 2-in. diam

MON* - Monsanto Co. (St. Peters, MO) Czochralski Wafers, 8-15 ohm-cm, <100>, p-type, 14-16 mil thick, 3-in. diam, cut down to 2-in. diam

MT† - RCA Mountaintop Czochralski Wafer, 1.5 ohm-cm, <100>, p-type, 13-15 mil thick, 2-in. diam

boron glass processing of the wafers was not clean enough for the gettering layer to be effective in increasing the diffusion length in the samples over their starting value. In spite of the low conversion efficiencies achieved with these cells, it can be concluded from these experiments that (1) the final conversion efficiency of the solar cell depends more on the diffusion length existing in the cell after processing than it does on the starting wafer resistivity or orientation. The tests also indicate that (2) if cells of high conversion efficiency are to be fabricated, then the diffusion length found in the starting wafers, which in the cells considered here ranges from 100 to 130 μm, must be increased by a factor or two or more. This point is graphically illustrated in Fig. 18 where all of the cells listed in Appendix A, upon which diffusion length measurements have been made, have their conversion efficiency plotted as a function of diffusion length measured in the finished cell. When the diffusion length is less than the thickness of the cell, the efficiency is an increasing function of the diffusion length in the final cell, and if the diffusion lengths are not increased over their value of ~100 μm in the starting wafer, then low values of cell efficiency will be obtained. When the value of the diffusion length in the final cell equals or exceeds the thickness of the

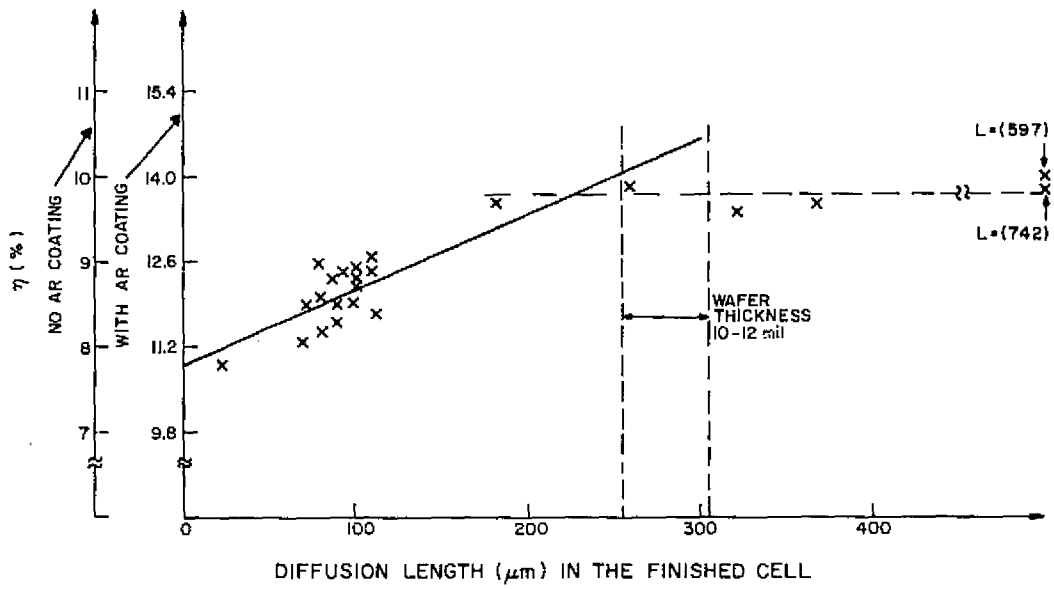

Figure 18. A plot of the efficiency of the ion-implanted solar cells as a function of the diffusion length measured in the finished cell. For the most efficient cells, the diffusion length equals or exceeds the wafer thickness.

wafer, the cell efficiency tends to saturate at a value determined by the achievable values of open-circuit voltage and fill factor. This saturation effect occurs because of the narrow base effect, i.e., L << W (the thickness of the cell). Under these conditions, for an ohmic contact, L_p in Eq. (4) can be replaced by W [15]. It should be noted here that when the diffusion length in the wafer approaches or exceeds the thickness of the wafer, the accuracy of both the SPV method and the parameter fit method becomes degraded and the experimental value measured becomes a lower bound on the actual value. For very long values of diffusion length, the effect of the back surface becomes significant and this effect is not adequately treated by the SPV method, although this parameter is included in the parameter fit to the quantum efficiency data. The best fit value for the backside surface recombination velocity is ∿150 cm/s.

H. ANALYSIS OF I-V MEASUREMENTS MADE ON ION-IMPLANTED SILICON SOLAR CELLS UNDER CONDITIONS OF ILLUMINATION OR TOTAL DARKNESS

The results of the experiments discussed so far indicate that the most important factor controlling the efficiency of the cell is the diffusion length in the base region of the cell. One method of investigating this further is to measure the J_{o1} values of the cell [see Eq. (4)]. This can be accomplished by measuring either the dark or the illuminated I-V curves and then, on a semilog plot, extrapolating the tangent to the n=1 portion of the curve to zero voltage. Figures 19 and 20 show examples of this measurement performed in the dark on small test diodes positioned on the wafer along with the active solar cells (see Appendix B). Because the test diodes are of different areas, the J_{o1} values of the various units should scale with the diode area, but the J_{o1} values for each diode should be the same. In the example given in Fig. 19, the measured values fall in the range $J_{o1} = 4.4\times10^{-12} \pm 0.7\times10^{-12}$ A/cm^2. In actuality the data were analyzed by performing a curve fit of the measured data to Eq. (3) using as parameters J_{o1}, J_{o2}, and n. It is interesting to note that the J_{o2} values for the test diodes 2 to 5 on wafer IISS17 are too small to

15. J. Lindmayer, "Development of 20% Efficient Solar Cells," Final Project Report NSF/RANN/SE/GI-43090/FR/75/2, NSF Grant GI-43090, October 1975.

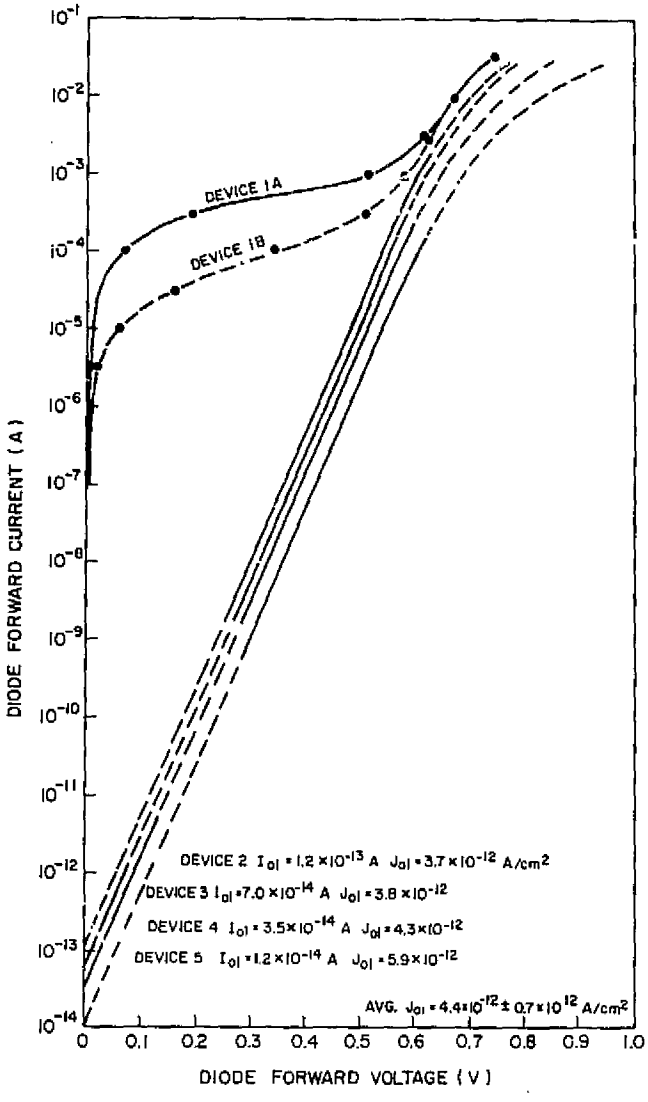

Figure 19. A plot of the dark I-V characteristics for six test diodes fabricated on solar-cell wafer IISS17. The n^+ layer was formed with a 5-keV ^{31}P implant and a dose of $5 \times 10^{14}/cm^2$.

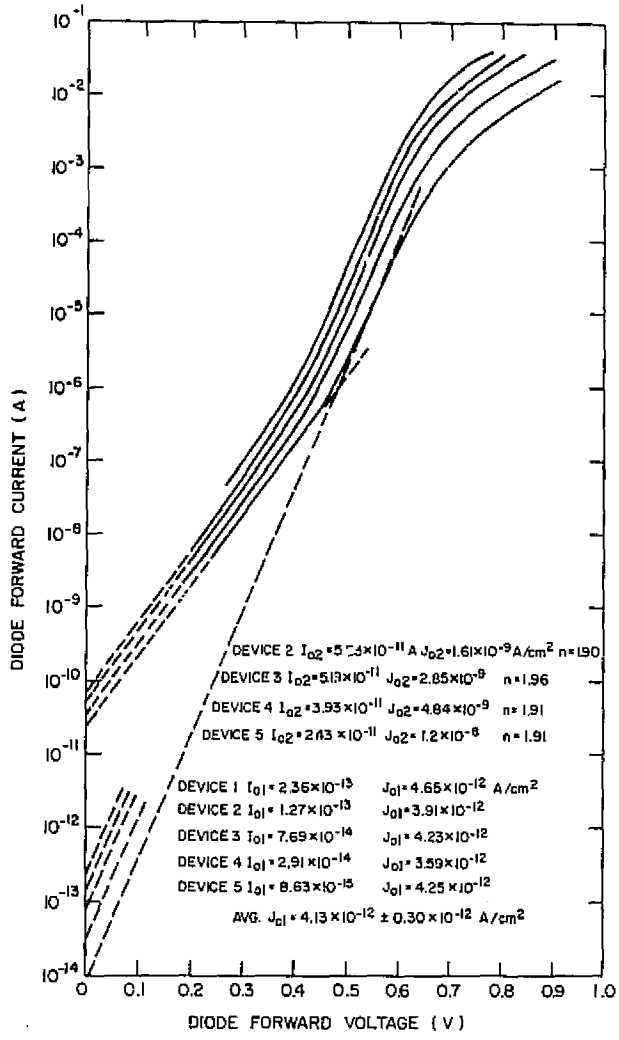

Figure 20. A plot of the dark I-V characteristics for five test diodes fabricated on solar-cell wafer IISS56. The n^+ layer was formed with a 5-keV ^{31}P implant and a dose of $4x10^{14}/cm^2$.

measure. The test diodes 1A and 1B on wafer IISS17, however, display a behavior that cannot be described by Eq. (3) because in this equation it is required that $1 < n < 2$. The behavior of these anomalous diodes is characteristic of shunt leakage within the diode most likely caused by wafer defects which fall in the region occupied by the diode or perhaps caused by alloy spiking of the metallization layer through the thin n^+ layer forming the diode.

Figure 20 shows dark I-V measurements made on test diodes on wafer IISS56. In this second case, no excess shunt leakage is observed; however, the defect recombination in the junction region is large enough to produce measurable values of J_{o2}. The values of J_{o2} in this case are respectibly small and indicate that the implanted dose does not introduce damage which causes problems, at 1 sun operating levels, by becoming nucleated and driven-in during subsequent annealing steps. Table 5 lists the values of J_{o1}, J_{o2}, and n for cells made with different implantation doses. For all dose levels considered, the values of J_{o1} are small.

TABLE 5. VALUES OF J_{o1}, J_{o2}, AND n OBTAINED BY LEAST-SQUARES CURVE FITTING THE MEASURED DATA TO Eq. (3)

Cell	Dose (atoms/cm^2)	J_{o1} (A/cm^2)	J_{o2} (A/cm^2)	n
IISS27	2×10^{14}	$(3.00\pm0.34)\times10^{-12}$	$(1.15\pm0.48)\times10^{-8}$	1.82
IISS56	4×10^{14}	$(4.13\pm0.30)\times10^{-12}$	$(2.52\pm1.2)\times10^{-9}$	1.90
IISS17	5×10^{14}	$(4.40\pm0.70)\times10^{-12}$	-	-
IISS18	7.5×10^{14}	$(8.1\pm2.0)\times10^{-12}$	-	-
IISS60	2.0×10^{15}	$(9.3\pm1.5)\times10^{-12}$	$(5.7\pm2.1)\times10^{-10}$	1.40
IISS69	1×10^{16}	$(2.3\pm0.36)\times10^{-12}$	$(3.17\pm0.08)\times10^{-8}$	1.55

To ensure that the test diodes are yielding a value of J_{o1} which also applies to the operation of the solar cell, illuminated I-V curves were also measured. If we restrict ourselves to a region of the I-V curve where n=1, then the current produced in a load across the cell is

$$J = J_o - J_{o1}(e^{qV/kT} - 1) \qquad (5)$$

When the cell is open circuited, $V = V_{oc}$ and $J = 0$, hence $J_o = J_o \left(e^{qV_{oc}/kT} - 1\right)$. When the cell is short circuited, $V = 0$ and $J_{sc} = J_o$. Hence, we can write

$$J_{sc} = J_{ol}\left(e^{qV_{oc}/kT} - 1\right) \cong J_{ol}\, e^{qV_{oc}/kT} \quad \text{for } V_{oc} >> qV/kT \qquad (6)$$

A plot of the $\mathrm{Ln}(J_{sc})$ vs V_{oc} for various levels of illumination should thus extrapolate to J_{ol}. This is a useful method for measuring J_{ol} in large cells with finger metallization because it avoids problems involved with the non-uniformity of current injection under dark conditions [16]. The plots in Fig. 21 show illuminated I-V curves for two different solar cells and show dark I-V curves for two different test diodes, all located on wafer IISS135. The J_{ol} values derived for the four cells are all in the range $J_{ol} = 5.1\text{x}10^{-12} \pm 0.5\text{x}10^{-12}$ A/cm^2 which is comparable to the spread observed among dark I-V measured values (see Table 5).

A plot of the J_{ol} values of a number of test wafers plotted as a function of the implant dose used to make the n^+ layer is given in Fig. 22. The horizontal dotted lines show the limits of the values of J_{ol} in 1- to 2-ohm-cm substrates having a post-processing diffusion length of 200 μm and assuming that all contributions from the emitter [Eq. (4)] are negligible. On a few of the cells, the actual post-processing diffusion length in the bulk region was measured, and in these cases the limits of the theoretical values of J_{ol} for 1- to 2-ohm-cm substrates, again assuming the contributions from the emitter term are negligible, are indicated in Fig. 22 with curly brackets. Figure 23 shows a plot of the values of J_{ol} as a function of the diffusion length measured in the bulk region of the final cell. These data, measured on cells with 1- to 2-ohm-cm and 8- to 12-ohm-cm starting substrates, indicate that the J_{ol} values of the cells closely track the value of the diffusion length which is obtained in the bulk. Note that the value of L obtained for cell 127 has been plotted at both the measured value (597 μm) and at the value corresponding to the wafer thickness (381 μm). The value yielded by the curve fit to the QE data is unreasonably large.

16. J. Lindmayer, "Theoretical and Practical Fill Factors in Solar Cells," Comsat Tech. Rev., Vol. 2, No. 1, pp. 105-121, Spring 1972.

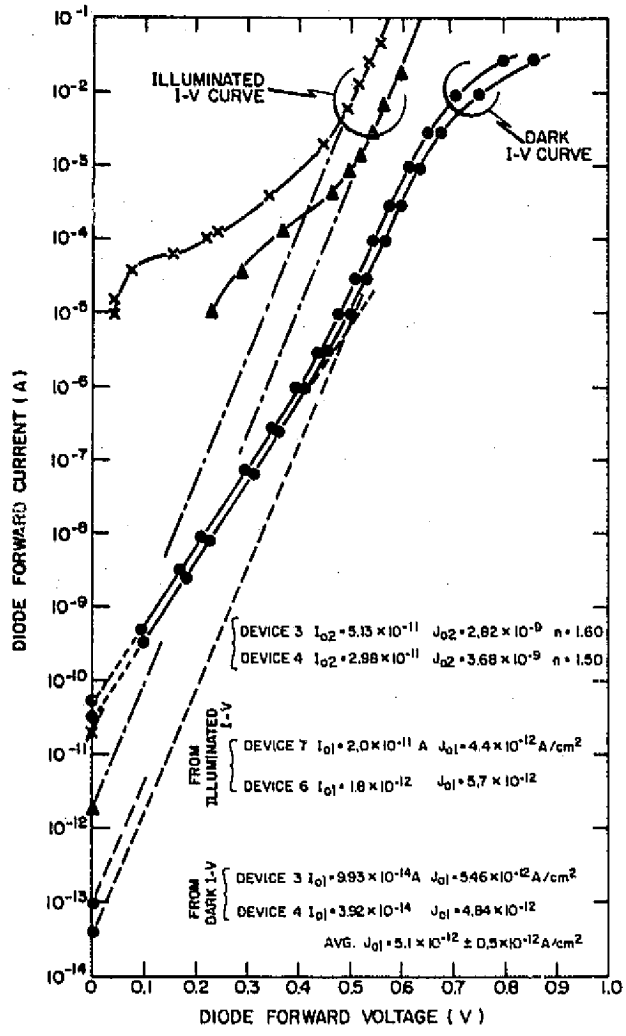

Figure 21. A plot showing both the dark and the illuminated I-V curves measured on two sizes of solar cells (0.316 cm^2 for device 6 and 4.5 cm^2 for device 7). The dark I-V curves were made on small test diodes included on wafer IISS135 along with the solar cells.

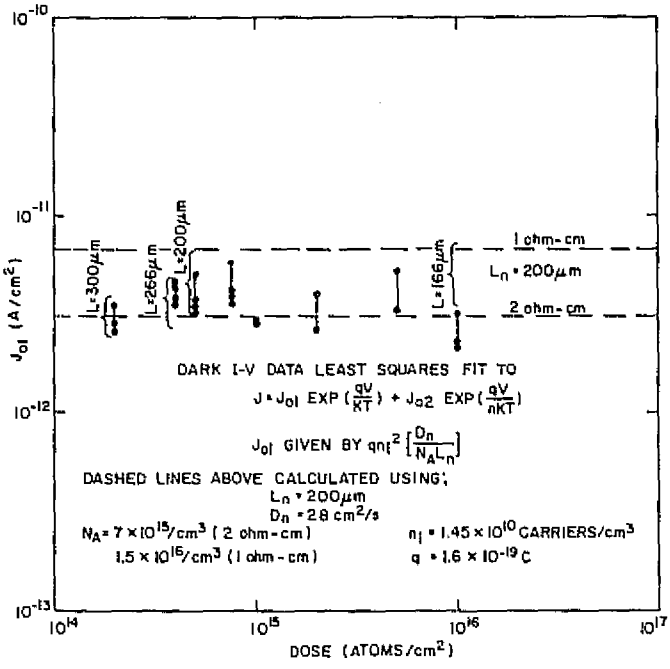

Figure 22. A plot of the values of J_{01} measured on various solar-cell wafers as a function of dose. The cells were fabricated on 1- to 2-ohm-cm wafers and the horizontal dotted lines mark the limits to be expected for a 200-μm diffusion length in the bulk. The curly brackets around the data points show the limits based on measured diffusion length in the cell.

The values plotted in Fig. 23 also indicate that the contribution to the J_{01} value caused by the emitter term [Eq. (4)] can at most be a small fraction of the contribution from the base term. The calculated contribution from the base term is given by the solid curves. If the emitter term equalled the base term, we would expect the experimental points to fall nearly on or above the solid line in Fig. 23 corresponding to 2 or 12 ohm-cm. The data points fall in the middle or in the lower portion of the range, indicating that emitter effects have not become significant in these two resistivity ranges. This is consistent with Lindmayer's [16] observations that saturation effects due to the emitter term should not become important until substrate resistivity values fall below 1 ohm-cm.

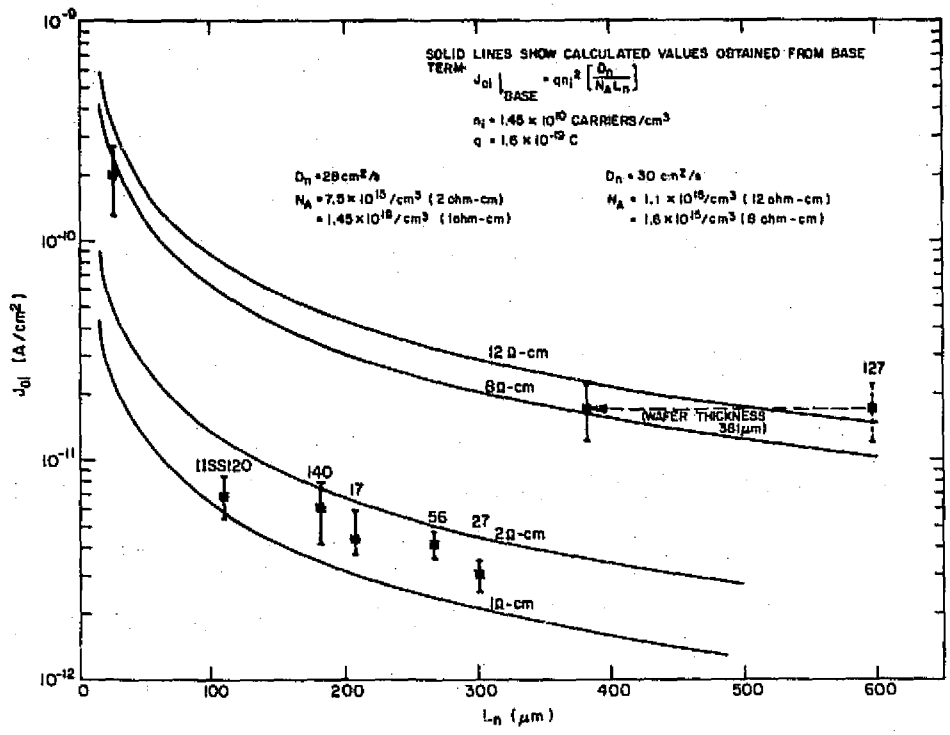

Figure 23. A plot of the values of J_{o1} measured on various solar-cell wafers as a function of diffusion length measured in the final cell.

It can be seen from Eq. (6) that a relation exists between J_{sc}, J_{o1}, and V_{oc}. It would be interesting to compute V_{oc} from the measured value of J_{sc} and J_{o1} and see how well it compares with the measured value of V_{oc}. Table 6 shows the results of the comparison for six cells made on two different wafer resistivities. The measured value of V_{oc} is generally lower than the computed value by an amount ranging from 0 to 11%. This effect could be caused by insufficiently alloyed metal contacts which allows the formation of a parasitic Schottky diode.

TABLE 6. A COMPARISON OF THE VALUES OF MEASURED V_{oc} AND THE VALUES OF V_{oc} CALCULATED FROM THE MEASURED VALUES OF J_{ol} and J_{sc}.

Sample	Substrate Resistivity (ohm-cm)	Diffusion Length (μm)	J_{ol} (meas) (A/cm^2)	J_{sc} (meas) (A/cm^2)	V_{oc} (meas) (volts)	$V_{oc} = \frac{kT}{q} \ln \frac{J_{sc}}{J_{ol}}$ T = 28°C	% Diff.
IISS119	8-12	23	$(2.0\pm0.7)\times10^{-10}$	20.0	0.510	0.524±1.7%	2.7
IISS127	8-12	(597)?	$(1.7\pm0.5)\times10^{-11}$	23.3	0.560	0.547±1.3%	2.3
IISS140	1-2	181	$(6.0\pm1.9)\times10^{-12}$	21.6	0.572	0.572±1.6%	0.0
IISS135	1-2	∿80	$(5.1\pm.09)\times10^{-12}$	19.6	0.556	0.573±.9%	3.1
IISS117	1-2	206	$(4.4\pm1.0)\times10^{-12}$	29.8	0.562	0.589±1.0%	4.8
IISS56	1-2	266	$(4.1\pm0.6)\times10^{-12}$	31.6	0.548	0.591±0.6%	7.8
IISS27	1-2	301	$(3.0\pm0.5)\times10^{-12}$	32.0	0.540	0.600±0.6%	11.1
IISS18	1-2	-	$(8.1\pm2.0)\times10^{-12}$	30.7	0.570	0.569±1.1%	0.2
IISS60	1-2	-	$(9.3\pm1.5)\times10^{-12}$	31.9	0.577	0.566±0.7%	1.9
IISS69	1-2	-	$(2.3\pm3.8)\times10^{-12}$	30.2	0.572	0.601±0.5%	5.0

I. QUANTUM EFFICIENCY MEASUREMENTS ON ION-IMPLANTED SOLAR CELLS

Quantum efficiency measurements were carried out on selected solar cells and the diffusion lengths in the final cells were deduced by curve fitting the equations for the cell response (see Hovel [2]) to the measured data. The diffusion-only model was used and the junction depth was assumed to be 0.4 μm. Collection effects associated with the depletion width were neglected. Figure 24 shows plots of the data reduction. The measured data was first corrected for surface reflectance to obtain the internal quantum efficiency curve. The four parameters L_p (base), L_n (emitter), S_p/D_p (back surface), and S_n/D_n (front surface), where S is the surface recombination velocity, were then varied to obtain best fit calculated values to the internal quantum efficiency curve. The values of diffusion length given in Appendix A under "L(μm), QE (after)" are the results of these fitting experiments.

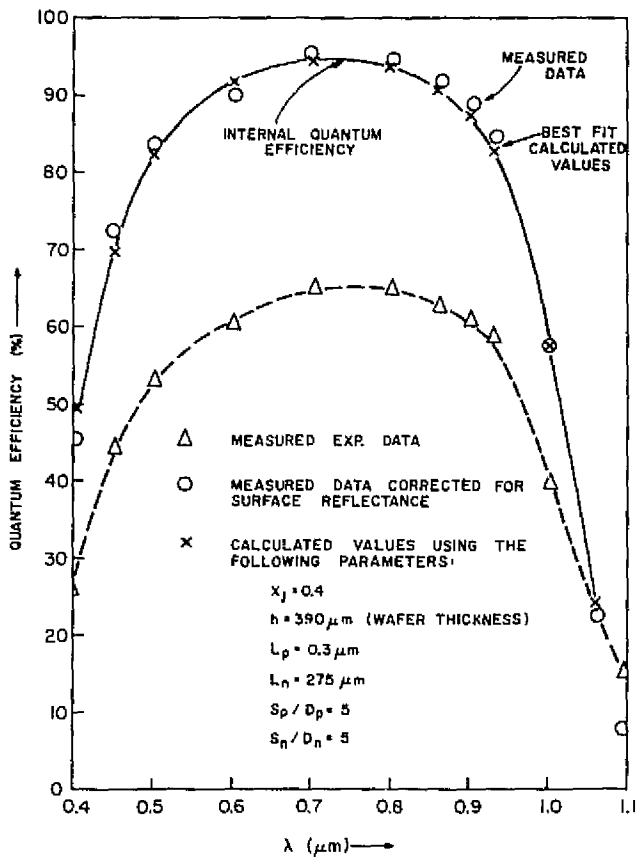

Figure 24. Plots of data reduction.

J. DISCUSSION AND CONCLUSIONS

The solar cells made during the course of this experimental study were fabricated using good quality silicon wafers and using optimum masking, capping, and metallization techniques. The object was to minimize as much as possible the potential conflicting factors which might interfere with the study of implantation effects that might adversely affect the performance of implanted solar cells.

It became apparent early in the study that processing steps eliminated by implantation, i.e., diffusion steps involving phosphorus and boron, act as getters in conventional processing and by their absence cause a degradation in all-ion-implanted cells. This degradation can be associated with a degradation of the minority carrier diffusion length in the bulk region of the solar cell. When these gettering steps are reintroduced, usually to form the back-side contact layer, then the diffusion length in the cells can be maintained or increased above the value in the starting wafer and efficient cells can be made with ion-implanted front-side active layers. Alternate processing procedures, involving the use of long low-temperature ($\sim$500°C) anneal steps, have also proved effective in maintaining or increasing the diffusion length in all-ion-implanted cells.

A careful examination of the I-V curves and the J_{o1} values of ion-implanted cells has indicated that for optimized implantation into substrates in the 1- to 2-ohm-cm and 8- to 12-ohm-cm resistivity ranges, the performance of the cell is dominated by the diffusion length in the bulk of the cells. Recombination effects associated with the highly doped, ion-implanted front side barrier layer are small compared to the base recombination effects. We conclude that there is no degradation in cell performance that can be associated with implant damage or the process of annealing out implant damage.

Two processes have been demonstrated for annealing the ion-implanted layers while at the same time preserving or improving the diffusion length in the base region of the cell. One of these processes, the boron glass process B, provides effective gettering at temperatures as high as 1050°C, so that anneal temperatures in the range between 900 and 1050°C can be used for efficient cell fabrication.

Experiments designed to optimize the implant procedures and the starting wafer characteristics indicate that 5- to 10-keV implant energies should be used and that doses in the range between $2 \times 10^{15}/cm^2$ and $4 \times 10^{15}/cm^2$ should be selected. ^{11}B into n-type wafers or ^{31}P into p-type wafers are both capable of producing cells with 15% conversion efficiency. The p^+n cells tend to have slightly higher open-circuit voltages. The characteristics of the wafer, i.e., <111> or <100>, float zone or Czochralski, n-type or p-type, are less important than the diffusion length which can be obtained in the wafer after processing. Wafer characteristics are only important, then, to the extent that they impact the observed diffusion length.

As a final observation, the technique of analyzing the initial and final diffusion length in the cells and combining these values with the J_{o1} and J_{o2} values obtained from either dark or illuminated I-V analysis has provided a data reduction procedure which has provided valuable insight into the operation of solar cells. The information obtained from cell performance tests indicates that a cell is good or bad; the diffusion length information and J_{o1}, J_{o2} information indicate why the performance is good or bad. This type of information also provides controls on the processing procedures because it can provide a continuing quantitative check on the performance of the annealing and gettering steps. Diffusion length analysis can monitor furnace problems and I-V analysis can isolate problems with shunt leakage, alloy spiking, or parasitic barriers.

When ion-implantation steps and other solar-cell fabrication steps are fitted together properly, efficient solar cells can be obtained. It is thus possible to realize the cost savings benefits and fabrication simplicity characterizing ion-implantation for the manufacture of silicon solar cells.

SECTION III

SCREEN-PRINTED THICK-FILM METALLIZATION

A. INTRODUCTION

In addition to the critical physical and electrical properties of the screen-printed metallization, the reliability of the screen-printing process as applied to solar cells was addressed initially. Therefore, this analysis will be described prior to the evaluation of metallization properties per se. The report concludes with a discussion of interface reactions and recommendations for future developmental effort.

B. SCREEN-PRINTING PARAMETERS

To check the possibility of silicon wafer cracking during or following screen-printing, a worst-case printing test was devised. It is known that screen-printing variables, e.g., squeegee speed, snap-off distance (screen-to-substrate distance), and squeegee compression can affect the uniformity of ink deposited. For example, Fig. 25 illustrates the change in coefficient of variation of ink weight deposited as a function of the three key variables. Normal printing is done in a squeegee speed range of 3 to 6 in./s and a snap-off distance of 0.025 to 0.040 in. Squeegee compression, which directly affects the force applied to the substrate to be printed, is best kept within the 0.006- to 0.012-in. range. Excessive squeegee compression, although useful in improving deposited-ink uniformity, unnecessarily stresses the substrate and hastens squeegee wear.

The applied force vs squeegee compression was measured directly with a force gage and found to be about 0.6 lb at 0.009-in. squeegee compression as shown in Fig. 26. This mid-range compression value was then used for the test. Nine silicon wafers, as-sawed, and measuring about 0.022 in. thick were screen printed with the collector grid pattern on *both* sides of the wafer at 90° orientation to each other. This orientation maximized the stress applied to the wafers midway between the collector grid lines. The printed wafers were cleaned to remove the dried ink deposit and, with an unprinted control wafer, exposed to a thermal shock cycle. The wafers were immersed in liquid N_2 (-196°C) for 20 s and transferred rapidly to liquid 1-octodecanol (200°C),

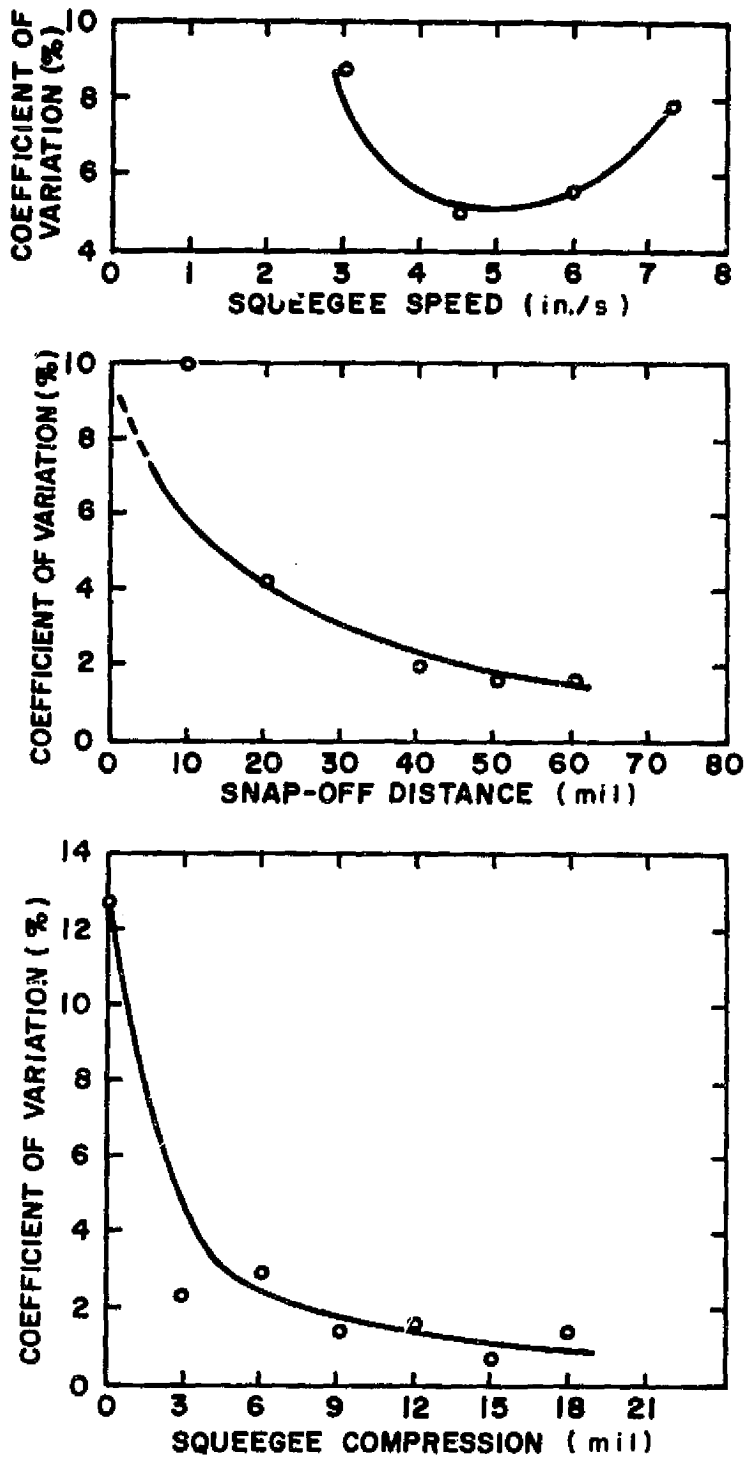

Figure 25. Effect of coefficient of variation of various screen-printing parameters.

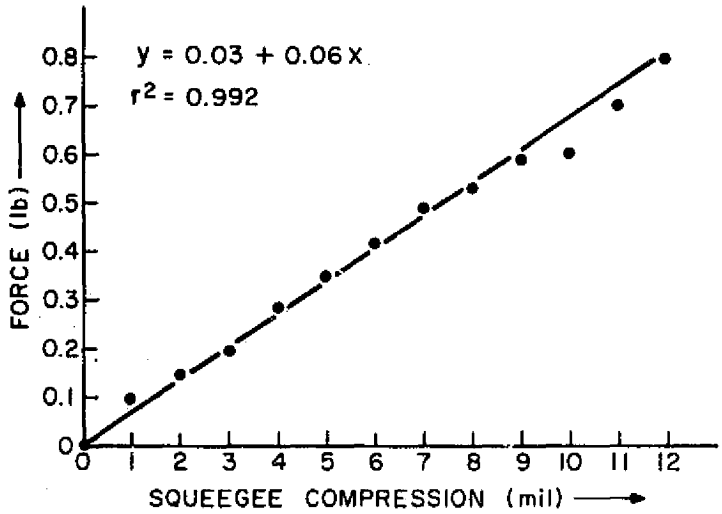

Figure 26. Applied force as a function of squeegee compression in screen-printing.

held there for 20 s and transferred rapidly to liquid methanol (45°C) to remove the 1-octodecanol. This cycle was repeated five times for all wafers. All wafers were subsequently examined microscopically and after etching* to delineate any cracks which may have formed during printing, thermal shocking, or etching. No cracks were found. It is therefore assumed that normal screen-printing forces will not damage wafers containing stress raising flaws induced by the sawing operations.

C. MATERIALS CHARACTERIZATION

Several commercial inks were purchased and analyzed prior to evaluation. The emission spectrographic analyses of these inks can be found in Appendix C. The commercial frit-bearing inks are generically lead borosilicate in composition with varying proportions of the three major oxides PbO, B_2O_3, and SiO_2. The remaining elements are present in trace quantities and are brought in by impurities in the raw materials and/or ball-mill grinding of the frit. The solids content of the inks ranged from 78 to 83 wt pct.

For RCA formulation three commercial Ag powders were selected, based on variation in particle size, and were analyzed for impurities by emission spectroscopy as shown in Appendix D, Table D-1. Of those impurities found, Cu

*50 cc HNO_3, 30 cc HF, and 20 cc acetic acid.

would most seriously affect the electrical conductivity of silver, since 0.1 to 0.2 wt pct Cu is soluble near room temperature. The Metz* K-150 Ag perhaps exceeds this amount, but it was kept for comparative testing anyway.

Cellulosic polymers, which are used to control viscosity and green strength in the ink were also analyzed as shown in Appendix C, Table C-2. Although the Na level is significantly above background in each case, the total quantity remaining available for diffusion into silicon is negligible when the ultimate dilution with other ink ingredients is considered.

Three specific frits or adhesive agents were prepared, two by standard glass melting techniques and ball-mill grinding. The third, $AgPO_3$, was formed by chemical precipitation from the reaction between $AgNO_3$ and stabilized HPO_3. The stability of the third frit is in question, since x-ray diffraction analysis identified $Ag_4P_2O_7$ and/or Ag_3PO_4 in various instances. A summary of material properties is presented in Table 7. The good wetting exhibited by the $AgPO_3$ and $80PbO\text{-}10B_2O_3\text{-}10SiO_2$ frit makes them excellent candidates for metallization on n- and p-type silicon surfaces, respectively.

TABLE 7. MATERIAL PROPERTIES

Material (wt pct)	Specific Surface Area (m^2/g)	Density (g/cm^3)	Contact Angle* (Degree) on Si	on Ag
$PbO(80)\text{-}B_2O_3(10)\text{-}SiO_2(10)$	0.4453	6.376	5	14
$PbO(70)\text{-}ZnO(10)\text{-}B_2O_3(10)\text{-}SiO_2(10)$	0.5240	6.079	36	43
$AgPO_3$	0.0291†	3.702	18	0
Ag (Metz K-150)	3.40	10.490	--	--
Ag (Metz FS Type C)	0.88	10.490	--	--
Ag (U.S. Met. Ref. 71-2)**	0.24	10.490	--	--

*Contact angle: after 10 minutes at 675°C in air.
**U.S. Metals Refining, Carteret, NJ.
†Some difficulty was noted in obtaining this value; use with caution.

*Metz Metallurgical Co., South Plainfield, NJ.

Particle size distribution curves, determined by the x-ray sedimentation method, are shown for the three Ag powders (and one Al powder*) in Fig. 27 and confirm that the high-surface area K-150 contains the highest percentage of submicron particles. While the finer particles are an aid to rapid sintering at low firing temperatures, they require an additional organic vehicle for proper dispersion. The resultant decreased metallic content in the ink raises the effective sheet resistance. For comparative purposes, however, the three Ag powders were retained for preliminary evaluations.

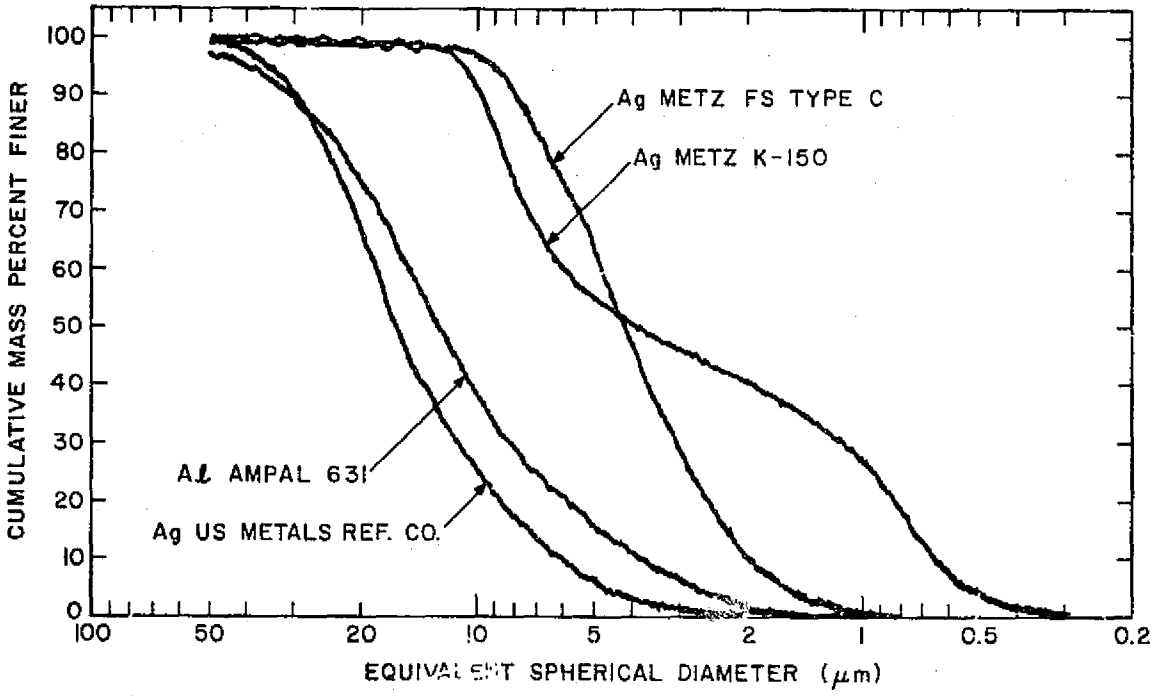

Figure 27. Powder particle size distribution curves.

D. ELECTRICAL CONDUCTIVITY OF RCA-FORMULATED AND COMMERCIAL INKS

The frit and Ag powder were incorporated into an ink vehicle consisting of 6 wt pct ethyl cellulose (N-300) dissolved in butyl Carbitol,** i.e., diethylene glycol monobutyl ether. The final solids content of the ink varied with the specific surface area of the Ag powder. The solids content of the

*Ampal 631 is a product of US Bronze Powders, Flemington, NJ.
**Carbitol is a registered trademark of Union Carbide Corp., New York, NY.

Metz K-150 Ag could only achieve a maximum of 70 wt pct and still provide adequate screen-printing quality whereas the lower surface area powders, Metz FS type C and U.S. Metal Refining* Lot 71-2, could be increased to 80 wt pct and still print well.

The test inks were screen-printed through an 1874-square serpentine line pattern (0.015 in. wide, 0.015 in. spacing) onto a 1- by 1-in. 96% alumina test substrate to determine ink conductivity. As shown in Fig. 28, the sheet resistance does not appear to vary significantly when the ink is fired for various time and temperature combinations. When the fired film thickness is measured microscopically and resistivity is computed, the effect of increasing time and temperature becomes more apparent, as shown in Fig. 29. However, it became obvious that determining minute differences in electrical conductivity would require a more accurate measure of metal deposited. Consequently, after sintering the test patterns, the Ag ink and substrate were weighed, the electrical resistance was measured, the Ag ink was stripped in HNO_3, and the substrate was reweighed. Hence, the exact weight of Ag deposited was obtained and this value used to compute the ideal resistance for that amount of Ag. From the observed-to-ideal resistance ratio, the percent of bulk electrical conductivity was computed, and these values are reported for the RCA-formulated and commercial inks in Tables 8, 9, and 10. It should be noted that each test pattern was heated to 500°C for 2 min prior to heating to the listed combination in the Tables. The one exception is shown in Table 10 where the Thick Film Systems** (TFS) 3347 Ag was fired at 300 and 400°C to illustrate the poor electrical conductivity achieved at these low temperatures.

In Table 8, which compares the unfritted RCA-formulated Ag inks, the highest conductivities are achieved by the Metz K-150 (3.4 m^2/g surface area) and Metz FS Type (0.88 m^2/g). The values for the 600 to 700°C regime range from 47 to 64% of bulk electrical conductivity when fired for 600 s. However, the U.S. Metal Refining Ag (0.24 m^2/g) only achieved 30 to 43% under the same conditions. The later Ag powder was therefore excluded from further testing.

In Table 9 the influence of various frit additions upon electrical conductivity of Metz K-150 and FS Type C silver is compared. It can be seen that the presence of sufficient frit, i.e., 10 vol pct, improves conductivity as

*U.S. Metal Refining Co., Carteret, NJ.
**Thick Film Systems, Inc., Santa Barbara, CA.

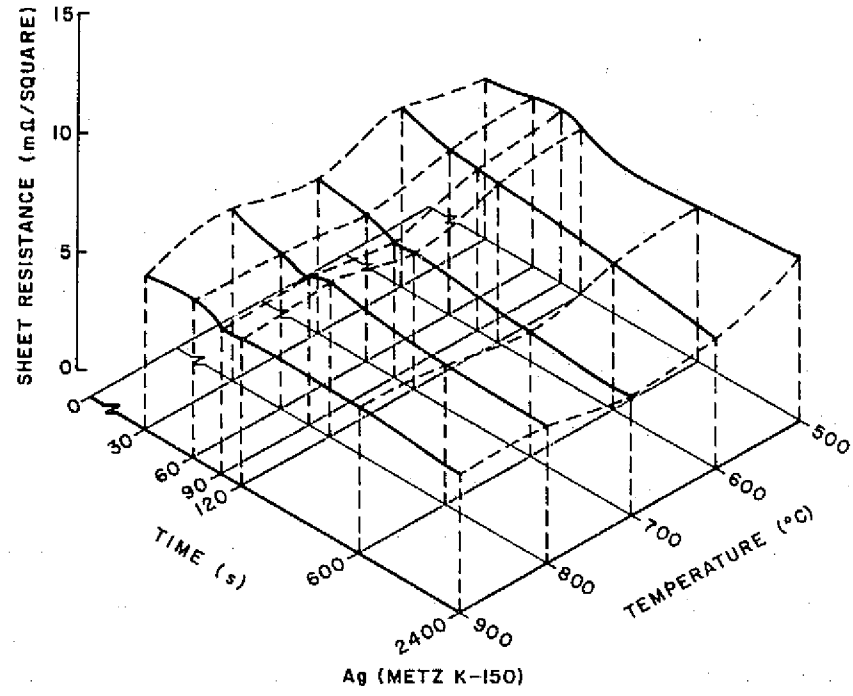

Figure 28. Firing time-temperature dependence of sheet resistance of screen-printed Metz K-150 silver ink.

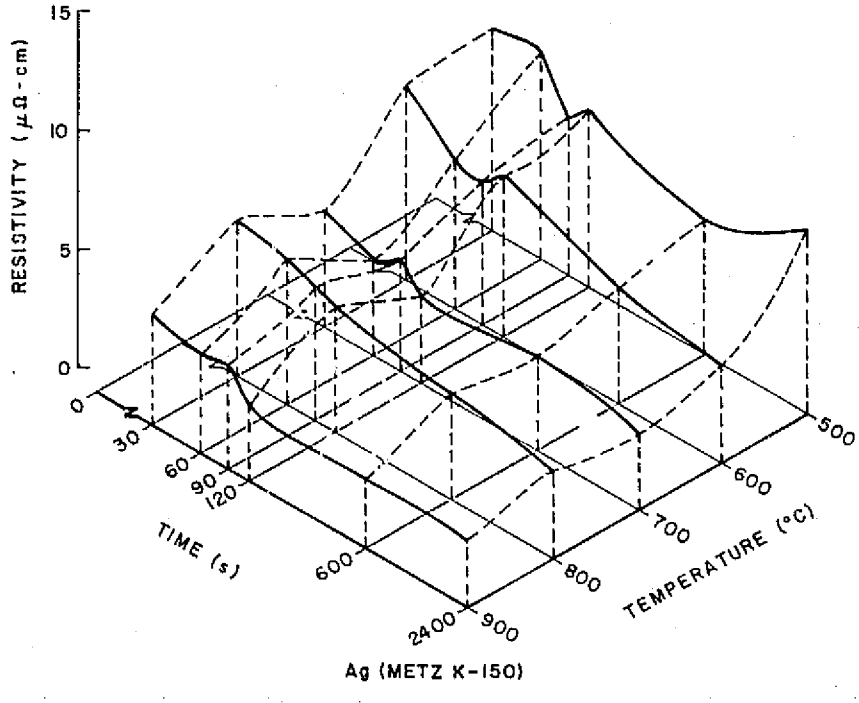

Figure 29. Firing time-temperature dependence of resistivity of sheet resistance of screen-printed Metz K-150 silver ink.

TABLE 8. PERCENT OF BULK ELECTRICAL CONDUCTIVITY OF RCA Ag INKS (NO FRIT)

	Temperature (°C)				
Time (s)	500	600	700	800	900
	RCA - Metz K-150 Ag				
30	50	46	52	47	52
60	47	49	54	52	55
90	45	49	59	55	55
120	47	50	59	47	55
600	52	55	64	57	58
2400	49	61	69	58	58
	RCA - Metz FS Type C Ag				
30	30	38	45	47	60
60	32	36	51	60	64
90	34	38	53	60	69
120	35	43	53	60	69
600	39	47	60	68	72
2400	41	53	61	70	75
	RCA - U.S. Metal Refining Lot 71-2 Ag				
30	25	26	31	--	41
60	24	26	32	33	45
90	26	28	35	35	44
120	26	29	35	35	22
600	28	30	43	37	35
2400	28	36	45	25	--

TABLE 9. PERCENT OF BULK ELECTRICAL CONDUCTIVITY OF RCA - METZ Ag vs FRIT CONTENT

	Temperature (°C)				
Time (s)	500	600	700	800	900
	RCA - Metz K-150 Ag (no frit)				
30	50	46	52	47	52
60	47	49	54	52	55
90	45	49	59	55	55
120	47	50	59	47	55
600	52	55	64	57	58
2400	49	61	69	58	58
	RCA - Metz K-150 Ag + 5 vol pct glass ($80PbO-10B_2O_3-10SiO_2$)				
30	48	47	56	60	60
60	48	48	58	59	58
90	47	55	58	59	56
120	45	56	59	63	57
600	49	51	59	62	61
2400	49	53	59	66	63
	RCA - Metz K-150 Ag + 10 vol pct glass ($80PbO-10B_2O_3-10SiO_2$)				
30	56	58	62	69	67
60	54	59	63	70	72
90	55	62	68	74	71
120	57	61	67	71	71
600	58	64	74	75	74
2400	58	70	71	74	69

TABLE 9. PERCENT OF BULK ELECTRICAL CONDUCTIVITY OF RCA - METZ Ag vs FRIT CONTENT (Continued)

	Temperature (°C)				
Time (s)	500	600	700	800	900
RCA - Metz K-150 Ag + 5 vol pct $AgPO_3$					
30	41	36	50	55	60
60	36	41	48	56	60
90	38	44	53	63	63
120	38	46	54	64	64
600	39	46	62	69	65
2400	41	50	63	67	67
Time (s)	500	600	675		
RCA - Metz FS Type C Ag + 10 vol pct glass ($80PbO-10B_2O_3-10SiO_2$)					
60	25	40	45		
90	32	44	48		
120	35	45	51		
600	42	54	61		
RCA - Metz FS Type C Ag + 3 wt pct Al + 10 vol pct glass ($80PbO-10B_2O_3-10SiO_2$)					
60	24	35	40		
90	27	48	39		
120	32	40	39		
600	38	48	44		

TABLE 10. PERCENT OF BULK ELECTRICAL CONDUCTIVITY OF COMMERCIAL INKS

	Temperature (°C)				
Time (s)	300	400	500	600	700
	Thick Film Systems 3347 (Ag)				
30	15	18	44	51	59
60	15	18	47	55	64
90	15	18	47	58	67
120	15	18	48	60	68
600	15	19	53	68	75
Time (s)	500	600	700	800	900
	Owens-Illinois 6105 (Ag)				
30	54	61	61	65	74
60	54	56	68	71	80
90	53	55	70	75	83
120	50	56	72	79	87
600	50	62	79	87	95
2400	52	67	81	93	98
	Thick Film Systems A-250 (no glass) (Ag)				
30	39	53	64		
60	42	61	70		
90	43	64	72		
120	44	67	74		
600	51	73	80		
	Englehard E-422-C (Ag)				
30	55	57	63		
60	56	61	66		
90	57	62	69		
120	58	62	70		
600	61	70	76		

TABLE 10. PERCENT OF BULK ELECTRICAL CONDUCTIVITY OF COMMERCIAL INKS (Continued)

Time (s)	Temperature (°C) 500	600	700	800	900
		Engelhard E-422-E (Ag)			
30	42	45	49		
60	42	47	53		
90	43	48	55		
120	43	48	57		
600	46	52	62		
		Engelhard E-422-D (Ag/Al)			
30	42	44	36		
60	42	45	33		
90	44	45	32		
120	44	46	33		
600	46	47	32		
		Engelhard E-422-F (Ag/Al)			
30	35	37	22		
60	35	38	9		
90	35	38	9		
120	36	39	9		
600	38	39	7		

predicted by liquid-phase-assisted sintering theory [17]. For example, at the 600-s firing time, the percent of bulk electrical conductivity increases from 55 to 64 when fired at 600°C and 64 to 74 when fired at 700°C for the Metz K-150 Ag. The percent of bulk electrical conductivity for Metz FS Type C with 10 vol pct frit fired at 600°C-600 s, however, is only equivalent to the pure, unfritted Metz K-150. This result is also expected since larger Ag particles in the FS Type C powder do not sinter as rapidly as the smaller particles in the K-150 powder.

Despite the lower electrical conductivity of the FS Type C powder, a greater solids content, i.e., 80 wt pct vs 70 wt pct for the K-150, in the ink is possible due to the lower surface area of the Ag. This difference showed up in the fired film appearance which was more dense than the K-150 Ag film, and may influence solderability and adhesion properties.

The initial test completed with 8.3 vol pct addition of $AgPO_3$ showed lower conductivity (Table 9) than pure K-150 Ag when fired at 500 to 700°C. At 800 to 900°C the conductivity of the $AgPO_3$ based ink was greater than the pure K-150. This improvement at the higher temperatures implies that the $AgPO_3$ precipitate was not pure but contained higher melting compounds, e.g., $Ag_4P_2O_7$ (mp* 585°C) and Ag_3PO_4 (mp 849°C) vs $AgPO_3$ (mp 482°C). Thus the benefit derived from liquid-phase sintering did not occur until these compounds melted. Further development is needed with $AgPO_3$ stabilization to improve the desired effect of low-temperature liquid-phase-assisted sintering.

With Metz FS Type C flake silver, Figs. 30, 31, and 32 depict the changes in conductivity for firing times of 1, 2, and 5 min, respectively, at 600 to 900°C and $AgPO_3$ concentrations of 8.3 to 30.1 vol pct. If the three plots are superimposed, the conductivity results show the 5-min firing time to be slightly superior, but the 1- and 2-min firing times are almost identical. The similarity in conductivity results provides a wide latitude in processing time. Hence, optimization of metallization solderability and adhesion can proceed without too much concern for conductivity losses. The slight decline in conductivity between 8.3 and 30.1 vol pct $AgPO_3$ may imply that lower concentrations would provide higher conductivity. While apparently contrary to

17. K. R. Bube and T. T. Hitch, "Basic Adhesion Mechanisms in Thick and THin Films," Final Report, March 1978, NASC Contract N00019-77-C-0176.

*Melting point.

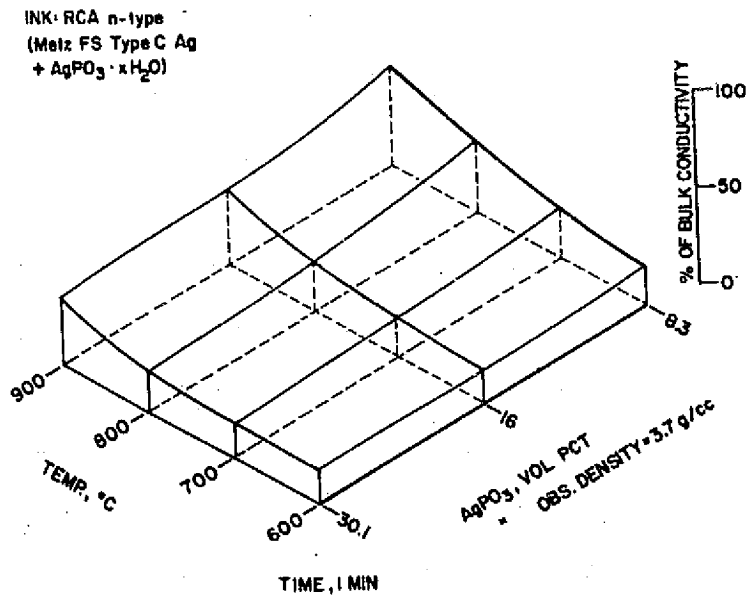

Fig. 30. Conductivity vs temperature and vol pct $AgPO_3$ for RCA n-type ink. Firing time = 1 min.

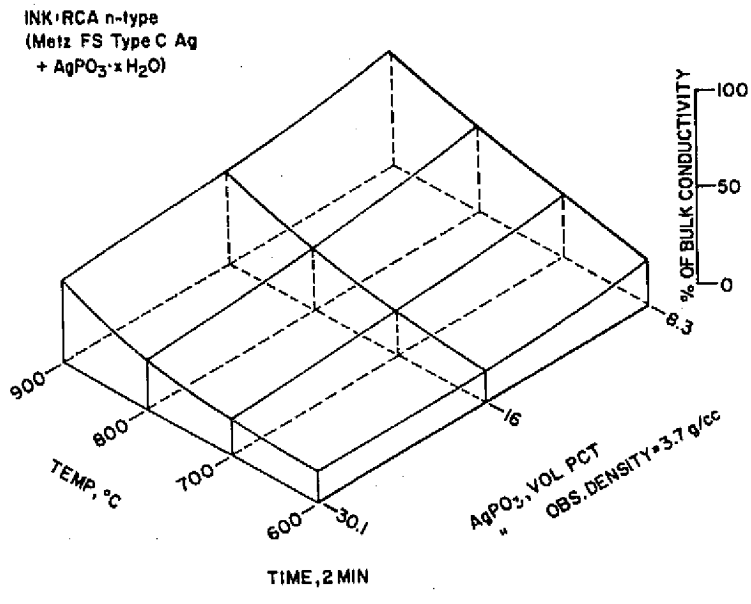

Fig. 31. Conductivity vs temperature and vol pct $AgPO_3$ for RCA n-type ink. Firing time = 2 min.

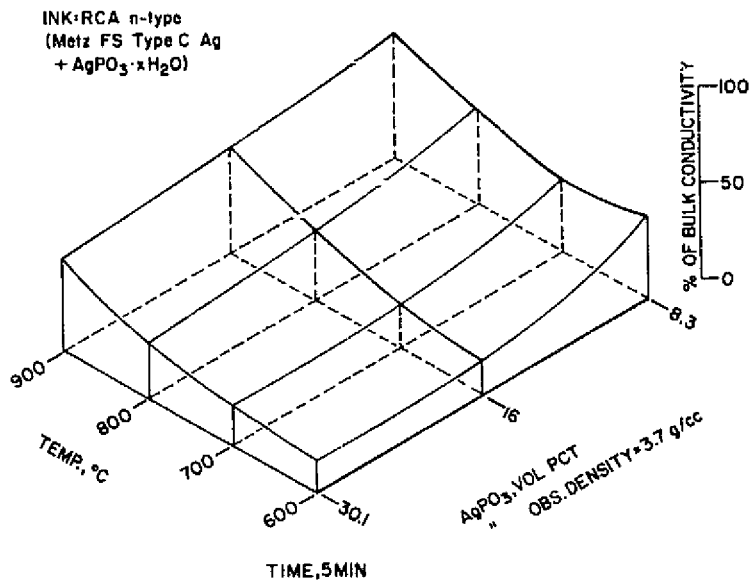

Fig. 32. Conductivity vs temperature and vol pct $AgPO_3$ for RCA n-type ink. Firing time = 5 min.

liquid-phase sintering theory, the extreme wettability, e.g., the 0° contact angle between Ag and $AgPO_3$, may account for very rapid sintering at lower concentrations than are usually observed. Excessive concentrations of the nonconductive phase would then predictably increase the electrical resistance of the film.

For contact to the p-type Si on the back of the cell, a Ag + 3 wt pct Al ink was prepared containing 10 vol pct glass. As shown in Table 9, the conductivity is generally lower than the unalloyed Ag inks for equivalent firing conditions. In air firing, two competing reactions are occurring, namely, oxidation of the Al powder and alloying with the Ag. Both tend to reduce the electrical conductivity, while sintering tends to raise it. Extended time at higher temperature appears to have a neutral to negative effect upon conductivity.

The electrical conductivity of commercial inks appears in Table 10 and shows data for Thick Film Systems 3347, A-250, Owens-Illinois* (OI) 6105, Engelhard** E-422-C, E-422-E, E-422-D (Ag/Al), and E-422-F (Ag/Al). When fired at 300 to 400°C the TFS 3347 Ag never exceeds 19% of bulk electrical conductivity, indicating the basic reason for much higher peak firing temperatures.

*Owens-Illinois, Inc., Toledo, OH.
**Engelhard Industries, Inc., East Newark, NJ.

When fired at higher temperatures, the conductivities are slightly higher than the RCA-Metz K-150 with 10 vol pct glass. Without careful analysis of Ag particle size distribution and glass composition and content it is difficult to surmise which, if not all, factors are contributing to the improvement. When TFS 3347 is compared with fritless TFS A-250, the higher electrical conductivity of the latter is also difficult to assess. At least the three previously mentioned factors can influence conductivity, i.e., Ag particle size distribution, glass content, and glass composition. For example, if the glass content is not sufficiently high or the glass viscosity is not sufficiently low at the selected firing temperatures, the conductivity will not be as high as the pure Ag ink, in keeping with liquid-phase-assisted sintering.

The phosphorus-bearing OI-6105 Ag shows progressively superior conductivity with increasing temperature when compared with RCA-Metz K-150 in the 700 to 900°C range. It is the only ink which actually approaches pure Ag conductivity when fired at 900°C for 2400 s. However, in the region of interest, e.g., 600 s at 600 to 700°C, the inks are about equivalent in conductivity.

Limited testing was also completed on two Engelhard Ag and two Engelhard Ag/Al inks. Ag ink E-422-C shows slightly superior conductivity in the 600-s, 600 to 700°C region and the other one, E-422-E, considerably lower conductivity than the RCA-Metz K-150 ink. Similarly, the Ag/Al inks are about comparable to slightly lower in conductivity.

In addition to Ag inks, a Cu ink, Cermalloy* 7029-5, was analyzed as shown in Appendix C, Table C-3 and found to contain a lead borosilicate frit, similar to the Ag inks. Conductivity data for the Cu ink were obtained after firing in tank N_2 and deoxidized tank N_2, and, as shown in Table 11, the Cu ink is considerably lower in conductivity in the area of interest, e.g., 600 to 700°C, than the RCA-Metz K-150 Ag ink.

Furthermore the dot-to-dot pattern, used for determining specific contact resistance, was applied to a silicon solar cell (lot 85). The contact resistance was measured after firing at 500, 600, and 700°C for 5 min and found to be 1.77 Ω-cm^2 at 500°C, 0.70 Ω-cm^2 at 600°C and 0.41 Ω-cm^2 at 700°C. The combination of high contact resistance and low electrical conductivity for the Cu ink is not encouraging. Therefore, attention will continue to be directed toward the Ag inks.

*Division of Bala Electronics, West Conshohocken, PA.

TABLE 11. PERCENT OF BULK ELECTRICAL CONDUCTIVITY

Cermalloy 7029-5 (Cu)

Time (s)	Temperature (°C) 500	600	700	800	900
	Ambient: Tank N_2, preheat 500°C-2-min				
30	22	27	33	41	45
60	22	28	40	48	55
90	22	36	43	51	57
120	24	33	46	50	56
600	28	48	54	59	62
2400	28	53	61	57	--
	Ambient: Deoxidized N_2, without 500°C-2-min preheat				
60	4	24	35	43	55
90	9	28	40	50	58
120	12	31	50	53	61
600	19	44	53	62	71

To test the effectiveness of laser heating as a quick means of sintering a screen-printed Ag line, a small comparative test was carried out. A 0.015-in.-wide x 0.75-in.-long test bar was screen-printed onto single-crystal Si pieces. Samples A and B were preheated after printing to burn out the polymer in the ink at 400°C for 30 s. If the ink polymer is not removed prior to exposure to the laser beam, the pattern is explosively removed upon laser pulsing.

Sample A was exposed to a Nd:glass laser pulse of 2.9 J/cm^2 and a second pulse of 3.6 J/cm^2. Sample B was fired in a belt furnace set to achieve about a 10-min dwell at 675°C. Electrical measurement showed sample A (laser pulsed) decreased in electrical resistance about 13% while sample B decreased about 58%. Thus, laser pulsing does not appear to be a practical way for rapidly sintering a screen-printed Ag line on Si.

E. SOLDERABILITY OF RCA AND COMMERCIAL INKS

Some preliminary tests were performed to determine relative solderability values. Both OI-6105 phosphated-silver ink and RCA inks were screened onto 96% Al_2O_3 substrates using the 1874-square serpentine pattern. After drying and firing for 10 min at 675°C, the metallization patterns were coated with Kester* 1544 solder flux and immersed in 215°C solder, i.e., 62Sn-36Pb-2Ag (wt pct), for varying times from 2 to 8 s. The sample patterns were visually examined to determine the extent of solder dewetting which is indicative of excessive silver dissolution by the solder or poor initial wettability. As shown in Table 12, OI-6105 is essentially unsolderable or too rapidly dissolved by the solder. The first RCA ink, Metz FS type C Ag + 10 vol pct PBS frit (i.e., $80PbO-10B_2O_3-10SiO_2$ wt pct) showed only slight dewetting up to 6 s. The second RCA ink, Metz FS type C Ag + 10 vol pct PBS frit + 3 wt pct Al, showed slightly greater dewetting but more resistance to longer immersion in molten solder.

TABLE 12. SOLDERABILITY COMPARISON - PERCENT DEWETTING

Metallization	Time (s) in 215°C - Solder (62Sn-36Pb-2Ag, wt pct)*			
	8	6	4	2
OI-6105	70-80	80-85	70-80	70-80
RCA-Metz FS Type C+ 10 vol pct PBS**	30-40	1	2	1
RCA-Metz FS Type C+ 10 vol pct PBS** +3 wt pct Al	5	5	5	5

*Flux: Kester 1544
**Frit: PBS is $80PbO-10B_2O_3-10SiO_2$ (wt pct)

The adhesion test pattern, described subsequently and shown in Fig. 33, also contained a large dot which was used in conjunction with reflowed solder balls to measure the solder-to-metallization contact angle.

A cursory examination of solderability of 4.2, 8.3, and 16 vol pct $AgPO_3$ inks showed the latter two to be unsolderable (with 62Sn-36Pb-2Ag wt pct

*Kester Solder Co., Chicago, IL.

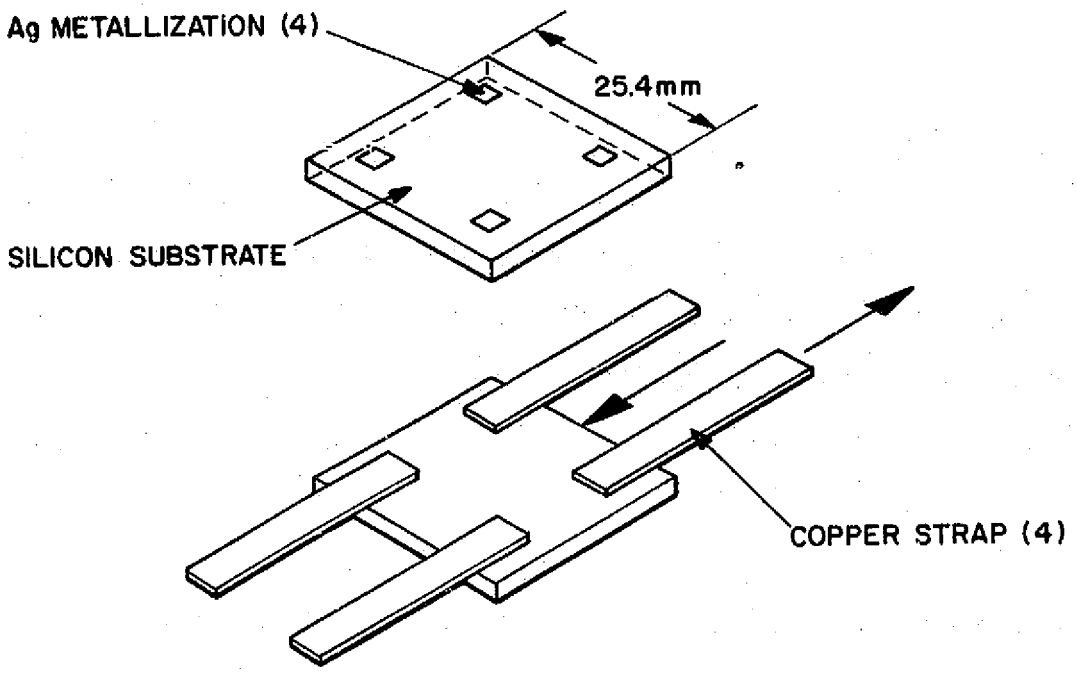

Figure 33. Adhesion test pattern.

solder and Kester 1544 flux) when the inks were fired on Si at 800 or 900°C for 1 or 2 min. The 4.2 vol pct $AgPO_3$ ink produced contact angles of 90 to 95° when the ink was fired at 700 or 800°C for 10 min.

More detailed studies of the $AgPO_3$ and lead borosilicate-based Ag ink solderabilities were conducted on n^+- and p-Si, respectively. Table 13 summarizes the data for $AgPO_3$-based inks containing 2 to 8 vol pct $AgPO_3$ and indicates progressively diminishing solderability with increasing $AgPO_3$ content. Best results are found in the 800 to 900°C ink firing temperature range with firing times of 1 to 3 min.

For lead borosilicate-based inks fired onto p-Si substrates the results, as shown in Table 14, indicate progressively decreasing solderability with increasing glass content, firing temperature, and time. With glass contents of 2.5 or 5 vol pct, solderability was acceptable for shorter firing times, e.g., 1 to 5 min, in the 600 to 900°C firing range. For the 15 vol pct glass-bearing ink, solderability results indicated a maximum firing range of 600 to 700°C for 1 to 5 min would be acceptable. Figures 34 through 39 summarize contact angle data graphically in n- and p-Si.

TABLE 13. SOLDER CONTACT ANGLE TO $AgPO_3$-BEARING Ag METALLIZATIONS ON n^+-Si (100) SUBSTRATE*

$AgPO_3$ vol pct, balance Metz FS Type C Ag

Firing Conditions °C-min	Angle (Degree) 2	4	6	8
600 - 1	D†	32	58	L††
2	D	104	114	L
3	D	62	L	71
700 - 1	36	124	124	L
2	24	D	L	L
3	D	D	100	L
800 - 1	46	63	60	L
2	45	133	136	43
3	57	56	144	L
900 - 1	33	146	151	L
2	25	49	50	L
3	27	102	85	99

*Reflowed solder (62Sn-36Pb-2Ag wt pct) balls using Kester 1544 solder flux and 215 ±2°C interface temperature for 5 to 8 s.

†D - Ag metallization pad dissolved by molten solder.
††L - Solder ball lifted, i.e., did not wet metallization.

TABLE 14. SOLDER CONTACT ANGLE TO LEAD BOROSILICATE-BEARING Ag METALLIZATIONS on p-Si SUBSTRATE*

Time (min)	Temperature (°C) 600	700	800	900
	Angle (Degree)			
	2 vol pct PBS** balance Metz FS Type C Ag			
1	17	17	35	49
2	18	24	40	69
5	19	37	52	59
10	18	52	62	68
	5 vol pct PBS balance Metz FS TYPE C Ag			
1	33	22	44	67
2	19	71	60	95
5	21	70	80	117
10	35	87	112	144
	15 vol pct PBS balance Metz FS Type C Ag			
1	44	77	117	159
2	51	109	139	160
5	76	109	157	159
10	82	149	158	158

*Reflowed solder (62Sn-36Pb-2Ag wt pct) balls using Kester 1544 solder flux and 215 +2°C interface temperature for 5 to 8 s.
**PBS = $80PbO-10B_2O_3-10SiO_2$, wt pct.

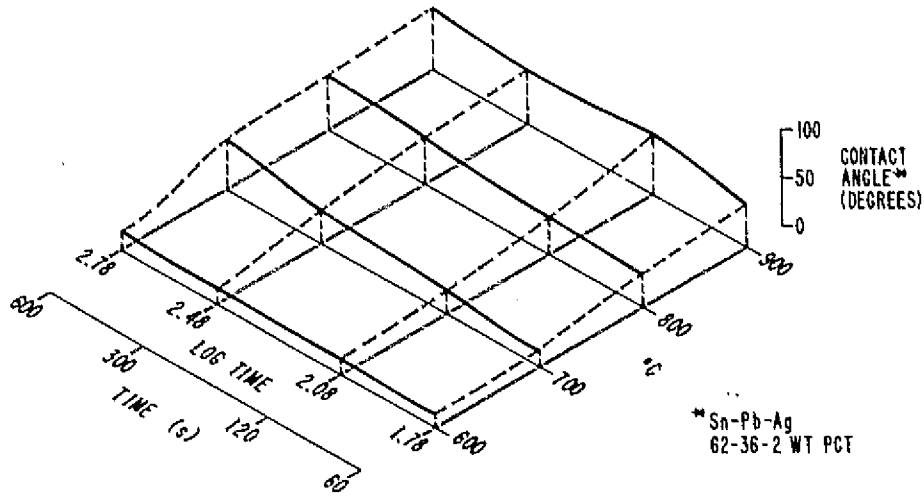

Ag (METZ FS TYPE C)+2.5 VOL PCT PBS FRIT ON p-Si

Figure 34. Wet solder contact angle as a function of firing temperature and time for Ag + 2.5 vol pct PBS ink on p-silicon.

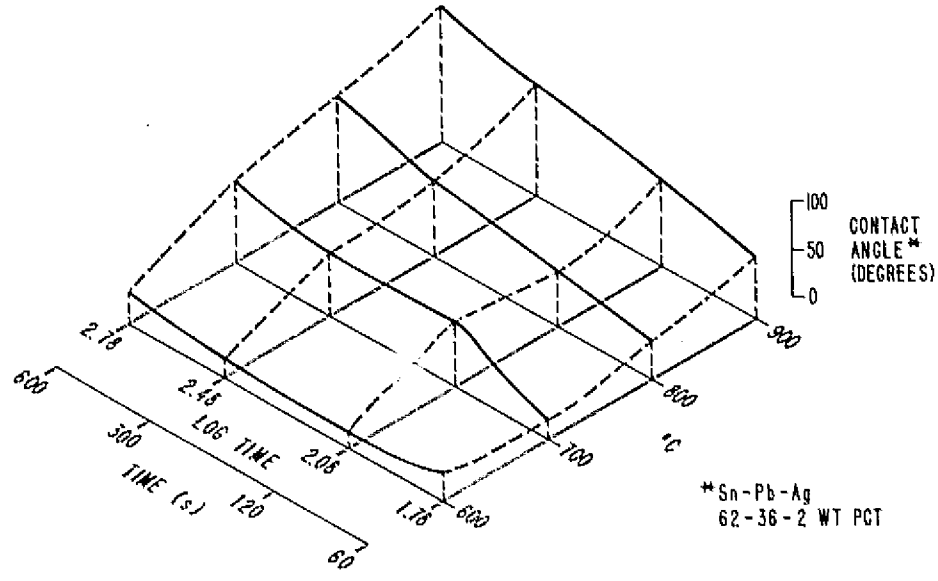

Ag (METZ FS TYPE C)+5 VOL PCT PBS FRIT ON p-Si

Figure 35. Wet solder contact angle as a function of firing temperature and time for Ag + 5 vol pct PBS ink on p-silicon.

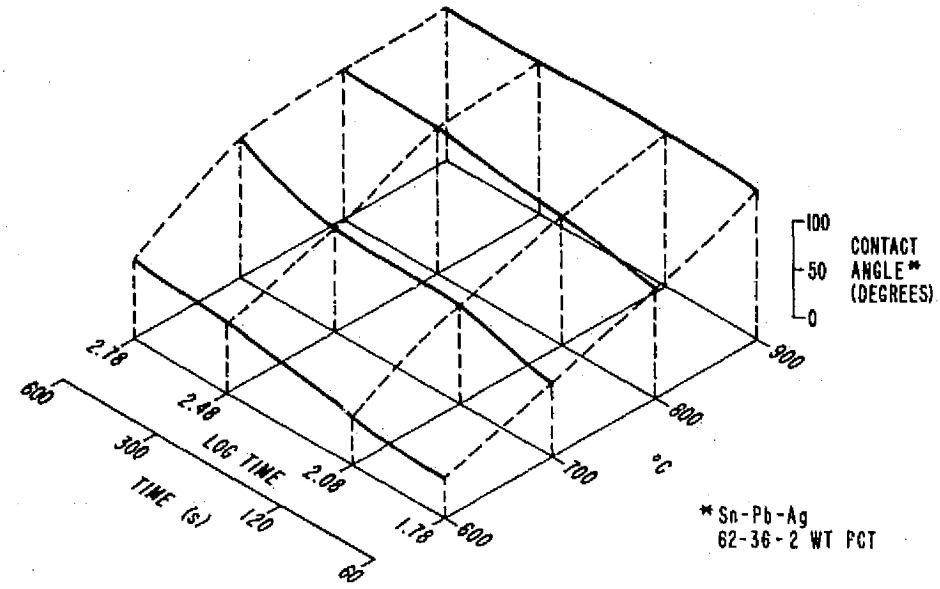

Ag (METZ FS TYPE C)+15 VOL PCT PBS FRIT ON p-Si

Figure 36. Wet solder contact angle as a function of firing temperature and time for Ag + 15 vol pct PBS ink on p-silicon.

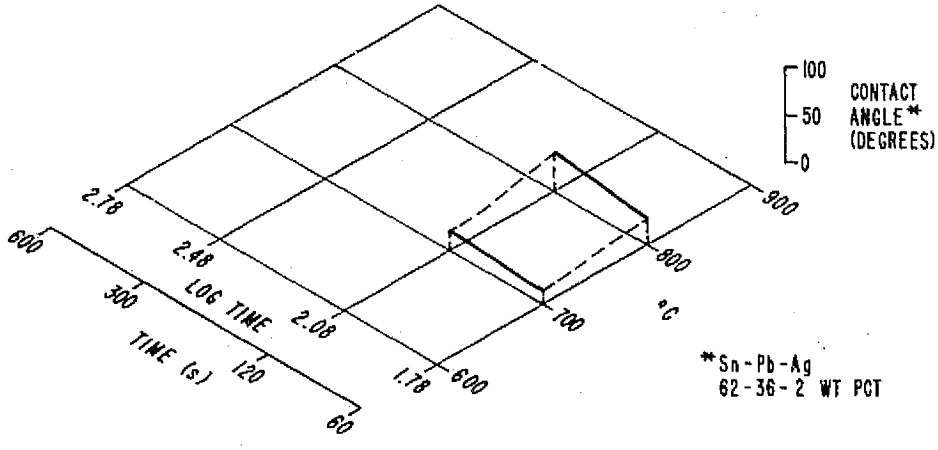

Ag (METZ FS TYPE C)+2.5 VOL PCT PBS FRIT ON n-Si

Figure 37. Wet solder contact angle as a function of firing temperature and time for Ag + 2.5 vol pct PBS ink on n-silicon.

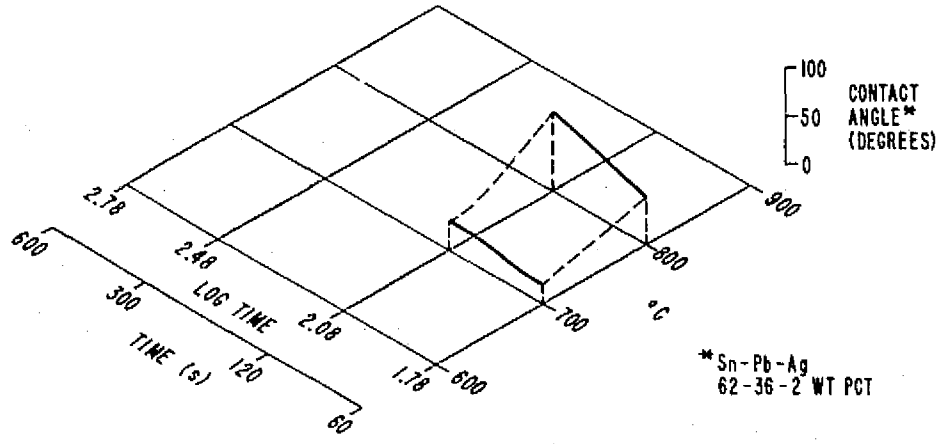

Figure 38. Wet solder contact angle as a function of firing temperature and time for Ag + 5 vol pct PBS ink on n-silicon.

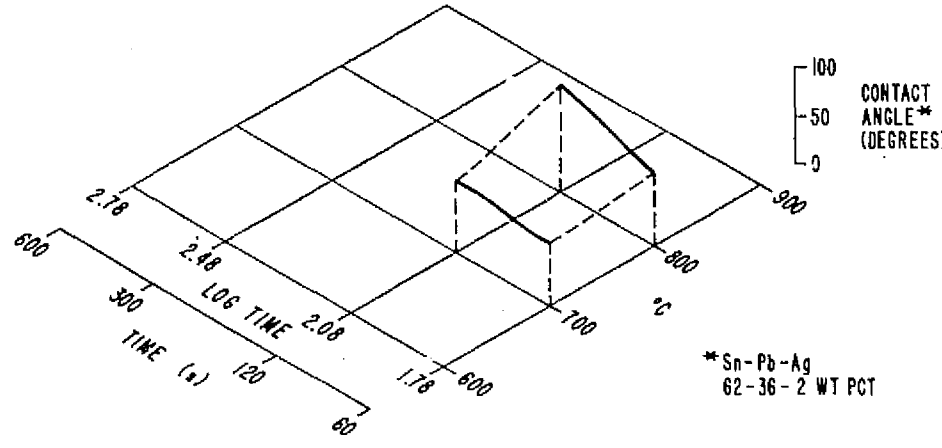

Figure 39. Wet solder contact angle as a function of firing temperature and time for Ag + 15 vol pct PBS ink on n-silicon.

Solderability can be improved by rinsing the fired metallization in HF (1 vol pct) for 30 s prior to soldering with flux. For example, as shown in Table 15, both the 15 vol pct PBS ink and commercial TFS 3347 (a lead borosilicate-based ink), which were fired for 2 min at 675 or 700°C, show a marked improvement in solderability after HF rinsing. Table 15 is also arranged to present data on adhesion strength results after thermal cycling, which is discussed below.

TABLE 15. SOLDER CONTACT ANGLE TO LEAD BOROSILICATE-BEARING Ag METALLIZATIONS ON n^+-Si (100) SUBSTRATE*

	Without Temperature Cycling		With Temperature Cycling**	
	Firing Conditions, 2 Min at			
	675°C	700°C	675°C	700°C
	Angle (Degree)			
	control			
TFS3347	33	44	49	37
RCA 15 vol pct PBS frit	47	73	49	62
	HF rinsed***			
TFS3347	20	18	16	19
RCA 15 vol pct PBS frit	20	21	19	17

*Reflowed solder (62Sn-36Pb-2Ag wt pct) balls using Kester 1544 solder flux and 215 ±2°C interface temperature for 5 to 8 s.
**Five cycles: 25°C to -40°C to 55°C to 25°C with 5-min dwell at extreme temperatures; single cycle time = 30 min.
***Immersed for 30 s in 1 vol pct HF in H_2O followed by deionized H_2O rise for 10 min at room temperature.

F. ADHESION STRENGTH OF RCA AND COMMERCIAL Ag INKS

Despite the poor solderability of OI-6105 it was included in the initial adhesion strength determinations which follow. The two RCA Ag inks and frit-bearing Engelhard 422E (Ag), 422F (Ag/Al), and Thick Film Systems 3347 (Ag) were also included, as well as fritless Thick Films Systems 250 (Ag). All the

inks were screen-printed with 325 mesh screen and 0.001-in. (0.0254-mm) emulsion buildup onto polished (100) silicon substrates so as to yield four test pads measuring 0.1 x 0.1 in. (2.5 x 2.5 mm) as shown in Fig. 33. The samples were dried and fired under three separate conditions: A - 675°C for 2 min in a tube furnace, B - 675°C for 5 min in a belt furnace moving at 15.2 cm (6 in.)/min, and C - 675°C for 10 min in the belt furnace moving at 7.6 cm (3 in.)/min. Copper straps were then applied by a reflow soldering technique for adhesion shear stress testing. The copper straps, which were pretinned with solder, measured 1.34 x 0.14 x 0.003 in. (34 x 3.5 x 0.08 mm). Kester 1544 solder flux and two 62Sn-36Pb-2Ag solder balls weighing about 0.005 g each were applied to the metallization test pads. The copper straps were positioned over the test pads and the assembly was placed on a 215 $\pm$2°C hot plate. Heating to 215°C took about 45 s, and the assembly was held at 215°C for 5 to 8 s before being quickly removed and cooled on a chilling block.

A shearing stress was then applied to the copper strap-metallization interface in an Instron Test Machine after allowing the assemblies to equilibrate for several hours at room temperature. The shearing forces, reported in Table 16, indicate a range of 0 (TFS fritless Ag 250) to 6087 g (RCA-Metz FS type C + 10 vol pct PBS frit +3 wt pct Al). This maximum value is equivalent to 1342 lb/in.^{2} (0.94 kg/mm^2) shear stress over the entire pad area. In many instances, however, the copper strap broke, in which case the silicon-metallization interface failure stress was not actually achieved, i.e., the interface strength exceeded the copper strap strength. In general, the three failure modes, e.g., copper, silicon, and interface failure, were observed on various inks with the weaker ones showing a predominance of interface failures. The stronger inks are generally noted to be the RCA inks and TFS 3347.

More detailed adhesion strength determinations were subsequently conducted on $AgPO_3$ and lead borosilicate-based Ag inks as well as the commercial lead borosilicate-based TFS 3347. The $AgPO_3$-based Ag ink was examined as a function of composition (2 to 8 vol pct $AgPO_3$), firing temperature (600 to 900°C), and time (1 to 3 min). Table 17 illustrates that acceptable adhesion strength, as demonstrated by copper strap failure, was found consistently only when the 2 vol pct $AgPO_3$ sample was fired at 900°C for 3 min. At lower firing temperatures, e.g., 600 and 700°C, copper strap-to-silicon delaminations were uniformly noted with no strength at low $AgPO_3$ concentrations. Consequently,

TABLE 16. METALLIZATION ADHESION SUMMARY FIRING CONDITIONS

Ink	Parameter	A 675°C-2 min (Tube)	B 675°C-5 min (Belt-6 in./min)	C 675°C-10 min (Belt-3 in./min)
OI-6105	$\bar{x}$* (g)	-	4015	4045
	%V**	-	33.3	8.7
	mode+	-	b	a,b,c
TFS 3347	$\bar{x}$	0	2775	0
	%V		21.7	
	mode	c	c	c
TFS 3347	$\bar{x}$ (g)	5465	5823	4818
	%V	9.1	5.3	11.9
	mode	a,b	a	a
Eng 422E	$\bar{x}$ (g)	0	4460	3930
	%V		43.3	37.8
	mode	c	b,c	a,b,c
Eng 422F	$\bar{x}$ (g)	3310	4218	3828
	%V	35.6	14.4	16.7
	mode	c	c	a,b,c
RCA-Metz FS Type C + 10 vol pct PBS	$\bar{x}$ (g)	4785	6015	5443
	%V	2.6	7.4	3.2
	mode	b,c	a	a
RCA-Metz FS Type C + 10 vol pct PBS + 3 wt pct Al	$\bar{x}$ (g)	4785	5533	5443
	%V	3.2	8.2	27.6
	mode	a,b	a,b	a,b

*$\bar{x}$ = shearing force, average value.
**%V = coefficient of variation.
+ Legend for failure mode: a = copper strap broke
b = silicon wafer broke partially or completely.
c = delamination somewhere between copper strap and silicon.

TABLE 17. ADHESION STRENGTHS OF $AgPO_3$-BEARING Ag METALLIZATIONS ON n^+-Si (100) SUBSTRATE

$AgPO_3$, Balance Metz FS TYPE C Ag

Parameter*												
						2 vol pct						
Temp (°C)		600			700			800			900	
Time (min)	1	2	3	1	2	3	1	2	3	1	2	3
$\bar{x}$ (kg)	0	0	0	0	0	0	0	0	0	0	0	0
%V	-	-	-	-	-	-	-	-	-	114	6	8
Failure Mode	c	c	c	c	c	c	c	c	c	b,c	a,b	a
Contact Angle (deg)	D	D	D	36	24	D	46	45	57	33	25	27
						4 vol pct						
$\bar{x}$ (kg)	0	0	0	0	0	0	0	1.6	0.6	1.6	5.3	5.0
%V	-	-	-	-	-	-	-	-	-	-	32	26
Failure Mode	c	c	c	c	c	c	c	c	c	c	a,b,c	a,c
Contact Angle (deg)	32	104	62	124	D	D	63	133	56	146	49	102
						6 vol pct						
$\bar{x}$ (kg)	0	0	0.8	0	0.8	0	0.6	1.8	3.0	3.8	5.4	5.9
%V	-	-	-	-	-	-	-	81	61	47	17	5
Failure Mode	c	c	c	c	c	c	c	c	c	b,c	a,b,c	b,c
Contact Angle (deg)	58	114	L	124	L	100	60	136	144	151	50	85
						8 vol pct						
$\bar{x}$ (kg)	0	1.0	0.6	0.4	0	0.6	0	0.7	0	1.3	2.6	4.0
%V	-	-	54	-	-	-	-	-	-	-	-	27
Failure Mode	c	c	c	c	c	c	c	c	c	c	c	b,c
Contact Angle (deg)	L	L	71	L	L	L	L	43	L	L	L	99

*Legend: $\bar{x}$ = force at failure in kg, average
%V = coefficient of variation, (Standard deviation ÷ $\bar{x}$) 100, sample size, n = 4, normally

Failure mode - a = copper strap broke
b = silicon wafer fractured or silicon chip removed under metallization
c = delamination somewhere between copper strap and silicon

effort was shifted to the lead borosilicate-based inks in order to obtain improved adhesion at lower firing temperatures.

From Table 18 it is clear that adhesion strength and failure mode varied with firing temperature, time, and glass content on p-Si substrate material. At low glass concentrations, e.g., 2.5 and 5 vol pct, acceptable adhesion and failure modes were found at the higher firing temperatures and time. With the higher glass content, e.g., 15 vol pct, acceptable results shifted to the lower firing temperatures, e.g., 600°C for times of 1 to 10 min and 700°C for 1 to 5 min. The results are consistent with glass wetting and sintering phenomena. At low glass concentrations, longer time and higher temperatures are required for sufficient quantity of glass to reach the Si surface to provide adequate adhesion between sintered Ag particles and the Si substrate. At high glass concentrations, e.g., 15 vol pct, sufficient glass is almost immediately present at the Ag-Si interface. Prolonged heating at elevated temperatures increases Ag film densification but also promotes additional wetting of the available Ag surfaces away from the Ag-Si interface. This additional wetting or coating of Ag particles with glass reduces solderability, as evidenced by the increasing contact angles for the 15 vol pct samples when fired at higher temperatures and longer times. With decreased solderability, an increasing frequency of copper strap-to-silicon delaminations was observed.

Limited adhesion strength measurements were again taken after depositing the same Ag inks on n^+-Si (100) substrates. In addition, these samples were exposed to three cycles of extreme liquid-to-liquid thermal shock, e.g., -75 to 125°C, in order to confirm the superiority of the 15 vol pct material. As shown in Table 19, only the 15 vol pct ink came close to acceptable limits. The consistent silicon fracturing is due to the mismatch in thermal expansion coefficients between glass and silicon.

Since HF rinsing of the fired Ag metallizations had been shown to improve solar-cell fill factor and efficiency, a test was conducted to compare the adhesion strength of rinsed and unrinsed samples with milder thermal cycling, e.g., -40 to 55°C. Both TFS 3347 and the RCA lead borosilicate-bearing ink were tested after firing at 675 and 700°C for 2 min.

As shown in Table 20, under all conditions both inks, with the exception of one sample, exhibited acceptable adhesion strength. After 30-s immersion in 1 vol pct HF at room temperature, the solderability of both inks improved

TABLE 18. ADHESION STRENGTH OF LEAD BOROSILICATE-BEARING Ag METALLIZATION ON p-Si (100) SUBSTRATE ($80PbO\text{-}10B_2O_3 10SiO_2$ wt pct) Balance Metz FS Type C Ag

Temperature (°C)	600				700				800				900			
2.5 vol pct																
Time (min)	1	2	5	10	1	2	5	10	1	2	5	10	1	2	5	10
$\bar{x}$ (kg)	3.5	3.9	3.5	6.3	3.1	5.3	6.8	6.6	4.9	6.6	6.7	7.2	7.1	7.3	7.3	6.9
%V	22	18	45	7	33	19	3	6	27	4	2	9	4	2	1	3
Failure Mode	c	c	c	b	c	a,b,c	a	a	a,c	a,b	a,b	a	a	a	a	a,b
Contact Angle (deg)	17	18	19	18	17	24	37	52	35	40	52	62	49	69	59	68
5.0 vol pct																
$\bar{x}$ (kg)	6.2	5.5	5.8	6.0	5.9	6.7	5.7	7.1	4.0	5.8	6.8	6.7	6.5	6.7	6.4	6.5
%V	5	26	10	10	17	5	16	6	38	12	9	8	10	13	21	2
Failure Mode	c	a,c	a,c	a,c	a,c	a,b,c	b,c	a	c	c	a,b,c	a,b	a,b,c	a,b	a,b	a,b
Contact Angle (deg)	33	19	21	35	22	71	70	87	44	60	80	112	67	95	117	144
15.0 vol pct																
$\bar{x}$ (kg)	6.8	7.1	6.9	6.8	6.8	6.5	6.9	7.1	6.9	6.7	4.6	2.8	6.4	4.7	4.8	4.5
%V	7	4	9	2	8	12	4	3	4	6	30	75	6	28	49	34
Failure Mode	a	a	a	a	a	a	a	a,b,c	a	a	c	c	a	a,c	a,c	c
Contact Angle (deg)	44	51	76	82	77	109	109	149	117	139	157	158	159	160	159	158

Legend: $\bar{x}$ = force at failure in kg, average
%V = coefficient of variation, (standard deviation ÷ $\bar{x}$) 100, sample size, n=4 normally

Failure mode - a = copper strap broke
b = silicon wafer fractured or silicon chip removed under metallization
c = delamination somewhere between copper strap and silicon

TABLE 19. ADHESION STRENGTH AFTER THERMAL SHOCK FOR LEAD BOROSILICATE-BEARING Ag METALLIZATION ON n^+-Si (100) SUBSTRATE

($80PBO-10B_2O_3-10SiO_2$ wt pct) Balance Metz FS Type C Ag

Parameter		2.5 vol pct		
Temp (°C)	700		800	
Time (min)	1	2	1	2
$\bar{x}$ (kg)	0	0	0	0.6
%V	-	-	-	43
Failure Mode	c	c	b,c	b
Contact Angle (deg)	14	22	29	41
		5.0 vol pct		
$\bar{x}$ (kg)	0.4	0.8	1.2	0.6
%V	-	73	-	-
Failure Mode	c	b,c	b,c	b,c
Contact Angle (deg)	20	33	51	85
		15.0 vol pct		
$\bar{x}$ (kg)	1.2	1.4	2.6	5.1
%V	33	36	40	18
Failure Mode	b	b	b	a,b
Contact Angle (deg)	68	78	74	113

Legend: $\bar{x}$ = force at failure in kg, average
%V = coefficient of variation, (standard deviation ÷ $\bar{x}$) 100, sample size, n = 4 normally

Failure Mode - a = copper strap broke
b = silicon wafer fractured or silicon chip removed under metallization
c = delamination somewhere between copper strap and silicon

TABLE 20. ADHESION STRENGTH OF LEAD BOROSILICATE-BEARING Ag METALLIZATION ON n^+-Si (100) SUBSTRATE

	Without Temperature Cycling		With Temperature Cycling*	
	Firing Conditions, 2 min at			
Parameters	675°C	700°C	675°C	700°C
		Control		
TFS 3347, $\bar{x}$ (kg)	6.5	6.5	5.6	6.5
%V	7	16	-	12
Failure Mode	a	a	a	a
Contact Angle (deg)	33	44	49	37
RCA, 15 vol pct PBS, $\bar{x}$ (kg)	6.5	6.6	6.4	6.4
%V	4	2	10	5
Failure Mode	3a,1c	a	a	a
Contact Angle (deg)	47	73	49	62
		HF rinsed***		
TFS 3347, $\bar{x}$ (kg)	6.6	6.5	6.7	6.5
%V	7	4	5	6
Failure Mode	a	a	a	a
Contact Angle (deg)	20	18	16	19
RCA, 15 vol pct PBS, **$\bar{x}$ (kg)	6.8	6.2	6.5	6.8
%V	5	10	4	3
Failure Mode	a	a	a	a
Contact Angle (deg)	20	21	19	17

*Temperature cycle: five cycles from 25°C to -40°C to 55°C to 25°C, with 5-min dwell at extreme temperature; single cycle time = 30 min.

**15 vol pct PBS - 15 vol pct glass frit composed of $80PbO-10B_2O_3-10SiO_2$ (wt pct)

***Parts immersed for 30 seconds in aqueous HF (1 vol pct) solution followed by deionized water rinse for 10 min

Failure mode: a = copper strap broke
b = silicon wafer fractured or silicon chip removed under metallization
c = delamination somewhere between copper strap and silicon

notably, as evidenced by a decrease in the contact angle. Under these conditions, all samples were strong enough to sustain copper strap breaks, i.e., shear stress in excess of 1 kg/mm^2.

G. METALLIZATION PENETRATION

Figure 40 illustrates the range of the typical phosphorous concentration profiles for average-depth n- on -p solar cells. Since it is known that metallization contact resistance rises abruptly if the phosphorous concentration is much below 10^{19} $atoms/cm^3$, it is apparent from Fig. 40 that metallization penetration, i.e., dissolution of the high phosphorous concentration region by ink constituents, must be less than about 0.1 μm average.

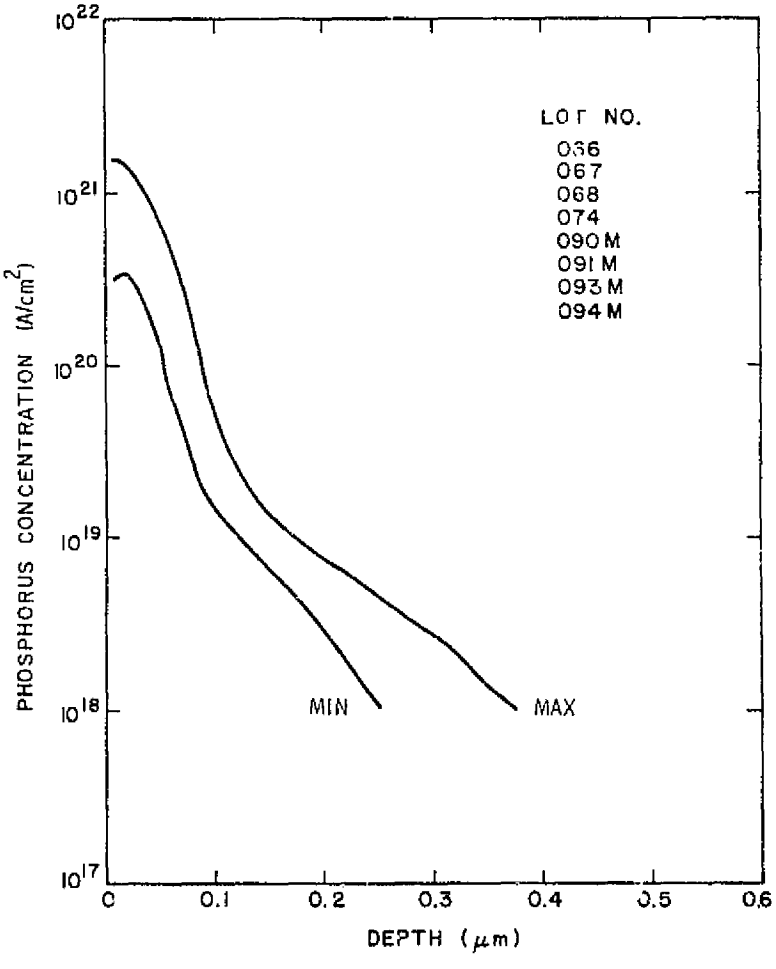

Figure 40. Range of $POCl_3$-diffused phosphorus concentration profiles.

To enable determination of the extent of penetration of the metallization, samples were treated with 1:1 NH_4OH-H_2O_2 solution to dissolve the Ag film. The remaining glass frit was dissolved in ultrasonically agitated HF solution. Scanning electron microscopy was then employed to determine the degree of attack on the underlying silicon.

For example, the RCA 15 vol pct lead borosilicate sample which was fired for 2 min at 800°C on n^+-Si is shown in Fig. 41 after metal and glass removal. Figure 41(a) illustrates the typical rectangular etch pits in (100)-oriented silicon caused by glass dissolution. Viewed at a low angle, Fig. 41(b) shows the depth of attack to be approximately 0.5 μm, essentially the entire n-layer thickness. From this observation, it is clear that such extensive dissolution would impair, if not preclude, device performance. Consequently, temperatures below 800°C must be considered as an upper boundary for solar-cell metallizing with this shallow junction design and glass composition.

H. APPLICATION OF SCREEN-PRINTING PROCESS TO SOLAR CELLS

1. Application to 3-in.-Diameter Cells with Diffused Junctions

Initial experiments were conducted with 3-in.-diameter solar-cell wafers having n^+ junction depths of ∿0.5 μm and sheet resistance of ∿30 Ω/□. These junctions were formed by a $POCl_3$ diffusion at 850°C for 60 min into p-type, 1- to 2-Ω-cm Czochralski wafers. The lots were split and printed on the sun-side with three different silver-based inks: Thick Film Systems TFS 3347, RCA-Metz type C, and Englehard E-422E. The backs of all samples were printed with Englehard E-422F Ag ink containing 3 to 4% aluminum.

The firing tests were conducted using two Argus International* #705 infrared lamp heaters. The samples were placed one at a time in a horizontal plane on a stainless-steel grid belt and fired simultaneously from both sides. A thermocouple placed on the sun-side of the wafers indicated that a temperature of 775 to 800°C was achieved in 30 s. Experiments were conducted at firing times of 1/2, 1, 1-1/2, 2, and 3 min.

The results as a function of the firing time are shown in Table 21. Good results were obtained at all firing times as indicated by the maximum

*Argus International, Hopewell, NJ.

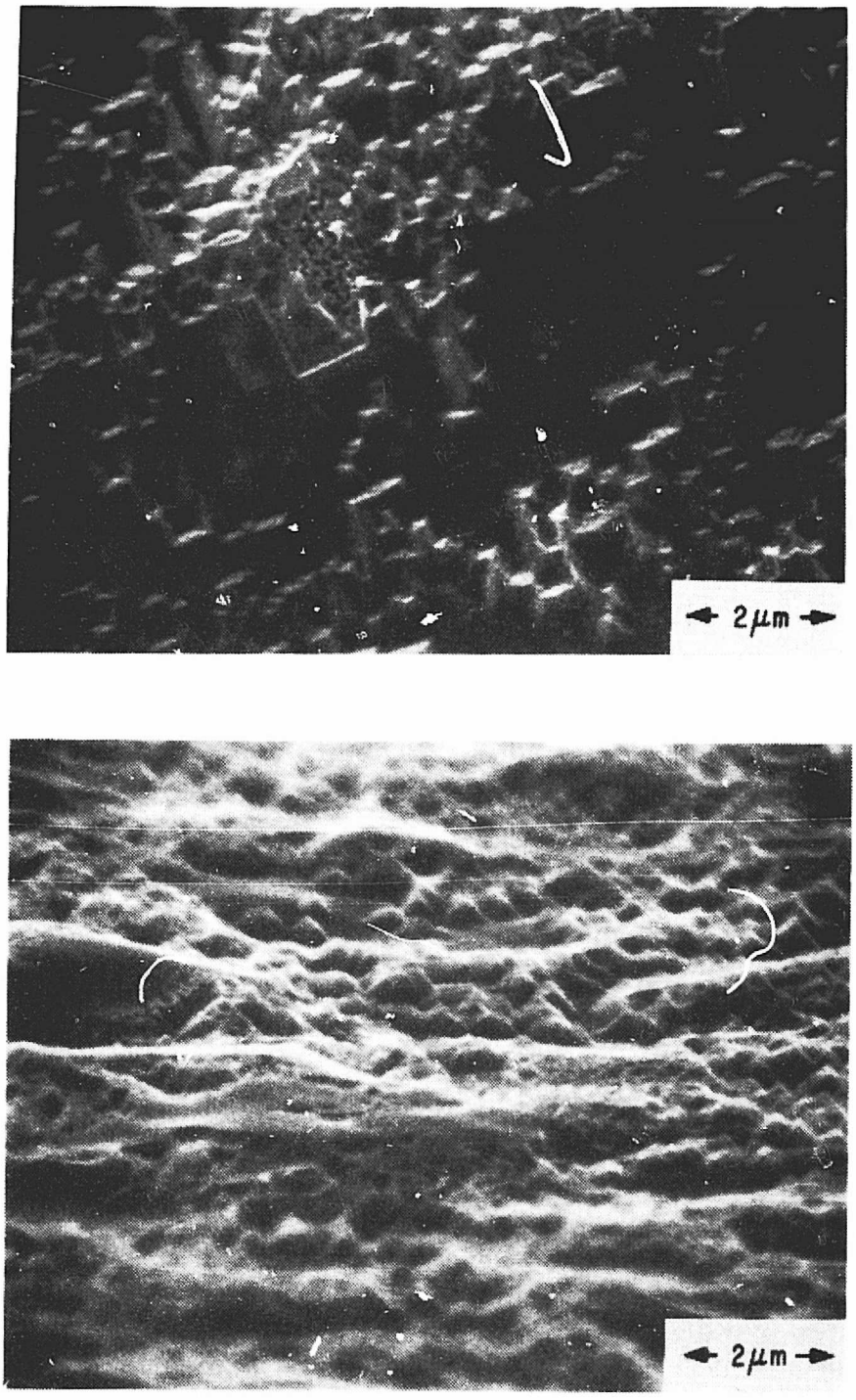

Figure 41. SEMs of n^+-silicon surface after dissolution of Ag and glass film. Film contained 15 vol pct lead borosilicate glass and was fired for 2 min at 800°C.

TABLE 21. RESULTS OF INFRARED LAMP FIRING AS A FUNCTION OF FIRING TIME

Firing Time (min)	No. of Samples	AM-1 Parameters J_{sc}* (mA/cm^2)	V_{oc} (mV)	FF -	FF_{max} -	η** (%)	η_{max}
1/2	8	20.7	577	0.662	0.731	7.9	8.9
1	9	20.5	582	0.697	0.728	8.3	9.0
1-1/2	10	20.2	577	0.679	0.713	7.9	8.8
2	8	19.8	574	0.697	0.727	7.9	8.7
3	5	20.0	572	0.703	0.717	8.0	8.6

*Cell area = 39 cm^2
**No AR coating

values shown in Table 21. However, wider variations in parameters were measured for the 30-s firing time, and some degradation in open-circuit voltage and short-circuit current is evident for increased firing time.

The solar-cell parameters as a function of ink are given in Table 22. It can be seen that the RCA type C ink yielded the best overall cell parameters with Thick Film Systems TFS 3347 a close second. The cells printed with Englehard ink E-422E generally had the lowest fill factors, caused primarily by excessive series resistance.

TABLE 22. SUMMARY OF INFRARED LAMP-FIRED SOLAR CELLS AS A FUNCTION OF INK

Ink		Firing Time	AM-1 Parameters J_{sc}*	V_{oc}	FF	FF_{max}	η	
Sun	Back	(min)	(mA/cm^2)	(mV)	-	-	(%)	η_{max}
TFS 3347	E-422F	1-3	19.8	577	0.690	0.713	8.0	8.8
RCA Type C	E-422F	1-3	20.4	582	0.700	0.717	8.2	8.8
Engelhard E-422E	E-422F	1-3	20.0	572	0.680	0.703	7.8	8.3

*No AR coating

The infrared lamp method of firing is rapid and seems to offer good stability and control. The experiments described below were conducted to assess the limits of this method and to determine optimum production parameters.

We have investigated the use of infrared-lamp heaters for firing screen-printed solar cells. The sensitivity of this method was studied by examining the effect of firing time and temperature on solar-cell parameters. The cells were from our standard lots of 3-in.-diameter wafers having junctions formed by $POCl_3$ diffusion with average junction depth of 0.5 μm and sheet resistance of 30 Ω/□. Studies were made with TFS 3347 and RCA n-type inks for the front grid metallization and RCA p-type for the back of the cells.

An attempt was made to measure the temperature of the metal film during heating rather than the surface temperature of the silicon. This was accomplished by imbedding a thermocouple in a small mass of the ink fired onto the silicon surface.

Firing times of 1 to 3 min in the 600 to 800°C temperature range were studied. An example of the results obtained for 1-min firing time is shown in Fig. 42. The temperature bandwidth is reasonably wide, about 50°C for a 1/4% decrease in efficiency. As might be expected, as the firing time is increased, the temperature for peak performance and the bandwidth decreases. Also, the onset of metal "spiking" becomes more abrupt.

2. Improvement in Fill Factor by HF Dipping

We have frequently noted low fill factors (∿0.65) with screen-printed solar cells even though they were fired under what we consider optimum conditions. These cells often exhibit expected values of short-circuit current and open-circuit voltage. It has been reported by other contractors that dipping the cells in hydrofluoric (HF) acid solutions can cause marked improvement in the fill factor, although a critical time in the solution was sometimes noted.

In our experiments, a 1% HF solution was used and we noted the following results:

(1) For screen-printed cells, an improvement in fill factor was noted in all cases. Substantial increases in fill factor were measured as shown in Fig. 43, with no degradation in other cell parameters.

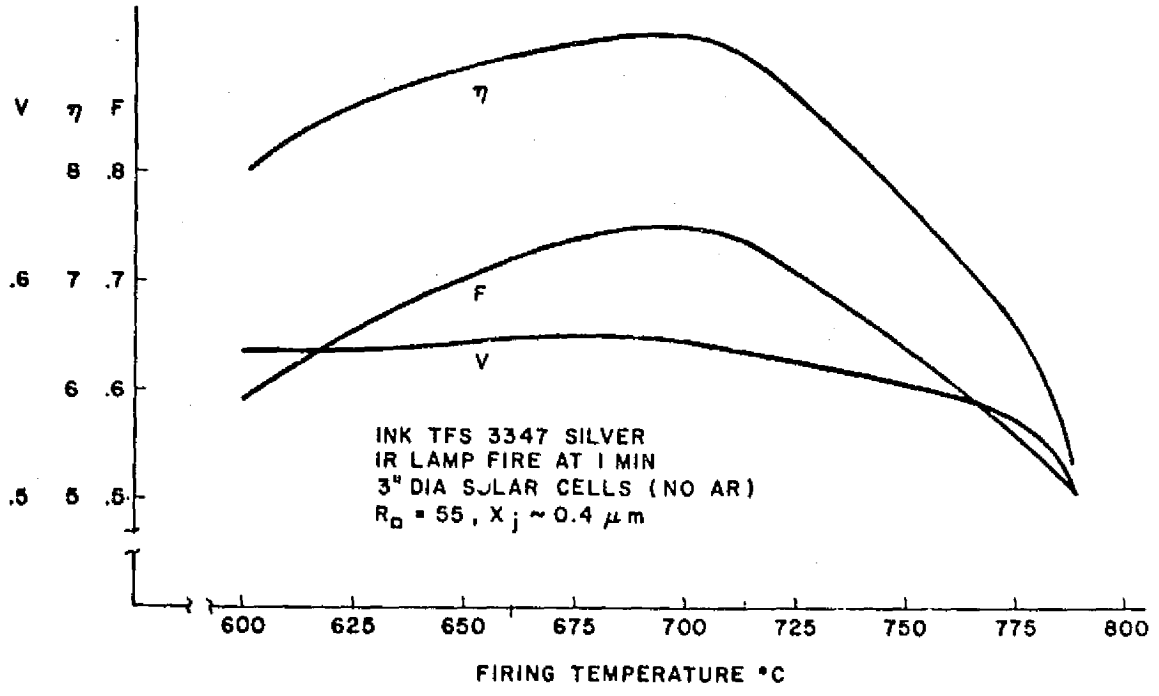

Figure 42. Results of test using infrared-lamp heater, 1-min firing time.

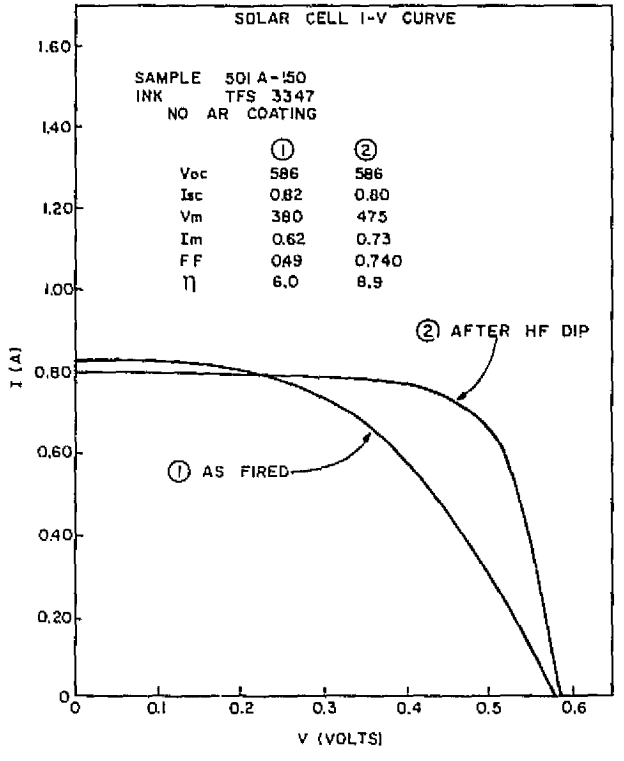

Figure 43. I-V curve produced by testing with HF dipping.

(2) No change in fill factor was measured for control cells which were metallized with conventional evaporated Ti/Pd/Ag.

(3) The time in the 1% HF solution was *not* critical. Generally, an increase in fill factor was noted for a 10-s dip and saturated after 40 s of dipping. Continuation of dipping beyond 40 s caused no apparent degradation of the cells.

At this time, we have no explanation for this effect.

In separate experiments with TFS 3347 and RCA n-type ink, the solderability and adhesion of these inks before and after a 30-s dip in 1% HF were measured. Marked improvement in solderability was measured and no change in relative bond strengths was noted.

3. Screen-Printing Applied to Ion-Implanted Solar Cells

Preliminary tests were conducted to apply screen-printing technology to cells with ion-implanted layers. Twenty-four samples were prepared, 12 for screen printing and 12 controls. The cells were fabricated with a phosphorus ^{31}P dose of 4×10^{15} A/cm^2 at 5 keV to form the n^+/p junction and the back p^+ contact was formed by either a boron implant (^{11}B, 5×10^{15} A/cm^2 at 25 keV) or by our boron glass BSF process (described in Section II of this report). Furnace annealing was used to activate the implants.

For the screen printing, TFS 3347 ink was used for both the front and back. It was felt that this ink would be adequate for the back contact since a p^+ layer is present in these samples. The screen contained the same pattern of 2- x 2-cm cells (Fig. 44) as that used photolithographically to define the contacts on the control samples. Firing was done with infrared lamps; the surface temperature was 675°C for 2 min.

After firing, the electrical output of the cells was measured under AM-1 illumination. The fill factors were between 0.4 and 0.6. The 1% HF dipping procedure described above was then applied. The cells were remeasured and a summary of the average AM-1 cell parameters obtained along with those for the controls is given in Table 23. Clearly, the HF dip caused a marked improvement in the fill factor.

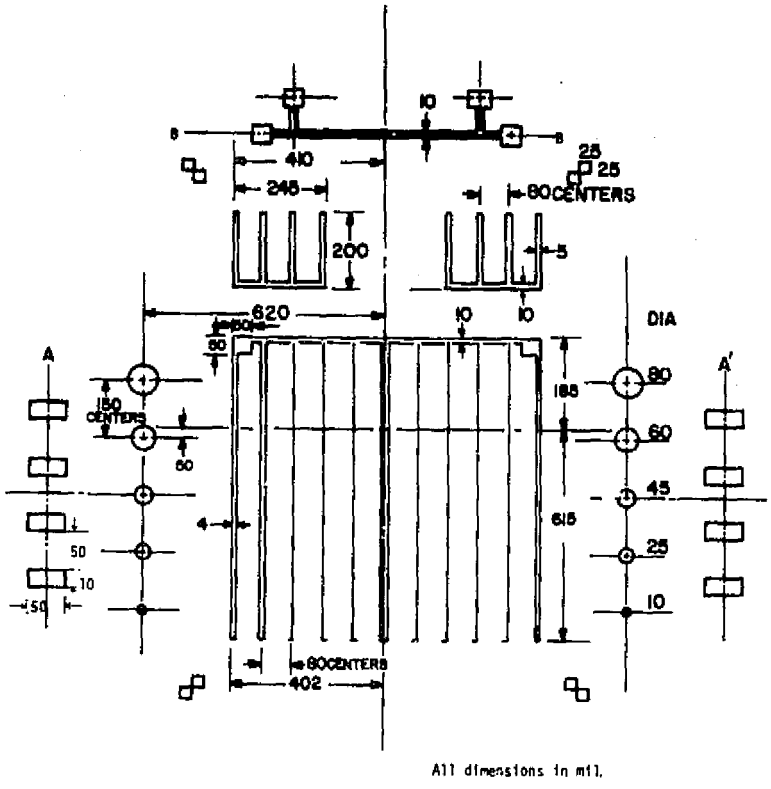

Figure 44. Solar-cell mask design including diagnostic cells.

TABLE 23. SUMMARY OF AVERAGE AM-1 CELL PARAMETERS FOR ION-IMPLANTED SOLAR CELLS WITH SCREEN-PRINTED METALLIZATION

Type of Sample	J_{sc} (mA/cm^2)	V_{oc} (mV)	FF -	η* (%)
Evap Ti/Ag; Boron-Glass BSF	20.3	555	0.785	8.8
Screen-Printed Ag**; Boron-Glass BSF	19.0	540	0.737	7.6
Evap Ti/Ag; Three-Step	22.1	582	0.777	10.0
Screen-Printed Ag**; Three-Step	20.9	550	0.750	8.6

*No AR coating
**TFS 3347 both sides

I. DISCUSSION AND CONCLUSIONS

A screen-printable lead borosilicate-doped Ag metallization ink has been developed specifically for solar cells. Material constituents have been characterized and the electrical conductivity, solderability, and adhesion explored as a function of ink composition and firing conditions. As a result of these evaluations, optimum material and process parameters have been established for the screen printed and fired metallizing of solar cells.

It was found that at least one commercial ink, TFS 3347, and the RCA n-type and p-type inks are suitable for forming thick-film screen-printed metallizations on 3-in.-diameter solar cells. Commercially available screen printers can be used to obtain high throughputs with good yield and the use of standard screens result in acceptable line definition for collector-grid patterns. Infrared lamps used for firing the contacts were found to provide a rapid and controllable process with reasonably wide tolerance in firing temperature and time.

On the negative side, the efficiencies of solar cells fabricated with the screen-printing process described here were about 85% of the control cells made with conventional evaporated contacts. This was primarily due to lower fill factors and in some cases, lower open-circuit voltage. However, the dramatic improvement in fill factor obtained by simply rinsing the cells in a 1% HF solution is an encouragement that higher efficiencies can be obtained by improved processing techniques.

Future effort should be focused on enhancement of solar-cell efficiency via HF rinsing techniques and development of non-noble metallizations for even lower cost solutions to the metallizing question.

SECTION IV

SPRAY-ON ANTIREFLECTION COATING PROCESS

A. BACKGROUND

Process development and optimization studies for low-cost spray deposition of single-layer antireflection (AR) coatings for metallized single-crystal silicon solar cells were conducted to examine: (1) effects of spray deposition machine parameters, (2) metallization bondability after AR coating, (3) cell electrical performance as a function of AR coating type and thickness, (4) heat treatment effects, and (5) characterization of AR films.

B. PROGRESS

1. Effects of Spray Deposition Machine Parameters

The automatic spray system used in our work is a Zicon Series 9000 autocoater.* This machine is a laboratory version of the much larger Series 11000 in-line unit which we have recommended for mass production applications. The spraying is conducted in a class 100 laminar downdraft clean booth supplied with HEPA-filtered air. A reciprocating spray gun traverses perpendicularly to the substrate cells, which are moved by an incremental advancing transport system. The machine operates automatically over a wide range of programmed cycles adjustable by front-panel controls. At least fifteen factors can be varied to provide the desired film thickness. These variables include (1) source solution delivery pressure, (2) atomization spray pressure, (3) gun-to-substrate distance, (4) propellant gas, (5) orifice size, (6) needle size, (7) spreader, (8) inserts, (9) gun-to-substrate distance, (10) solution flow rate, (11) number of spray guns, (12) spray gun traverse speed, (13) substrate advance rate, (14) source solution composition and reactant concentration, and (15) post-deposition heat treatments.

The first three variables are most easily manipulated for controlling film thickness with a given source solution. Three settings for each of these variables were selected to test their effects over the film thickness range of

*Zicon Corporation, Mount Vernon, NY.

interest. All other factors were held fixed at settings we considered near optimal. The propellant gas was nitrogen, the orifice size was 0.31 mm (12 mil), and a single spray gun was used. The RCA I titanium isopropoxide-based coating solution was used with polished silicon wafers as the substrate. The results are summarized in Table 24 and are graphically presented in Figs. 45 to 47. All three graphs exhibit a slight curvature over the narrow test range of practical interest to us. The film thickness increases with increasing source solution delivery pressure, with decreasing atomization spray pressure, and with decreasing gun-to-substrate distance. The uniformity of the AR film over the 7.5-cm-diameter test wafers was excellent throughout, demonstrating that any of the three machine variables can be used to fine-tune the thickness with good uniformity.

TABLE 24. AR FILM THICKNESS AS A FUNCTION OF THREE MACHINE VARIABLES

Source Liquid Delivery Pressure (kPa)	(in. H_2O)	Spray Atomization Pressure (kPa)*	(psig)	Spray-Gun-to-Substrate Distance (cm)	(in.)	Film Thickness** (Å)
4.98	20	172	25	14.0	5.5	560
7.47	30	172	25	14.0	5.5	750
9.96	40	172	25	14.0	5.5	840
7.47	30	138	20	16.5	6.5	680
7.47	30	172	25	16.5	6.5	640
7.47	30	207	30	16.5	6.5	550
7.47	30	172	25	11.4	4.5	740
7.47	30	172	25	14.0	5.5	680
7.47	30	172	25	16.5	6.5	640

*Referring to the gauge pressure.

**TiO_2 from RCA I titanium isopropoxide-based source liquid after post-deposition heat treatments for 30 s each at 70, 200, and 400°C. Surface temperatures were measured accurately with a calibrated thermocouple thermometer (Digital-Heat Prober by W. Wahl Corp.).

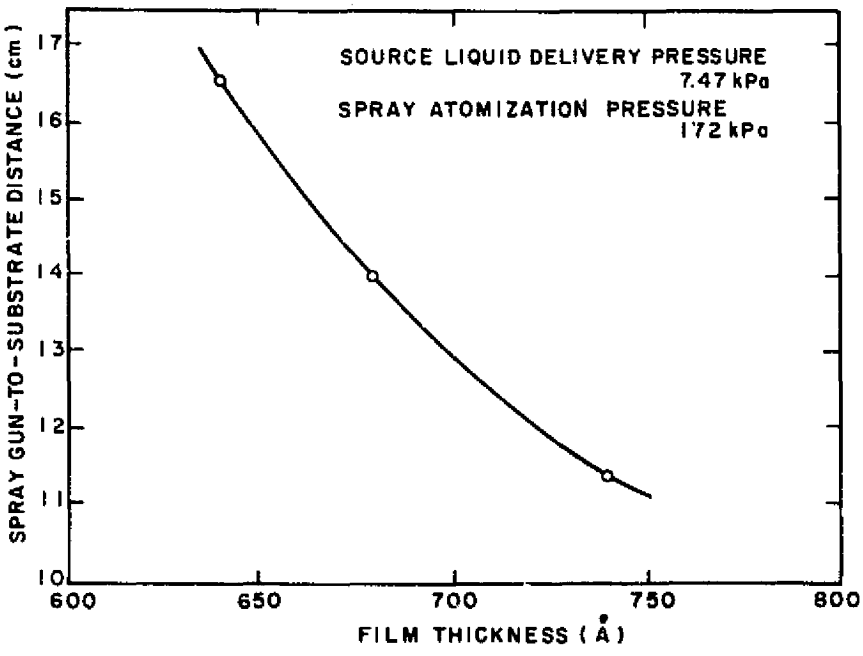

Figure 45. Effect of spray-gun-to-substrate distance as a function of film thickness.

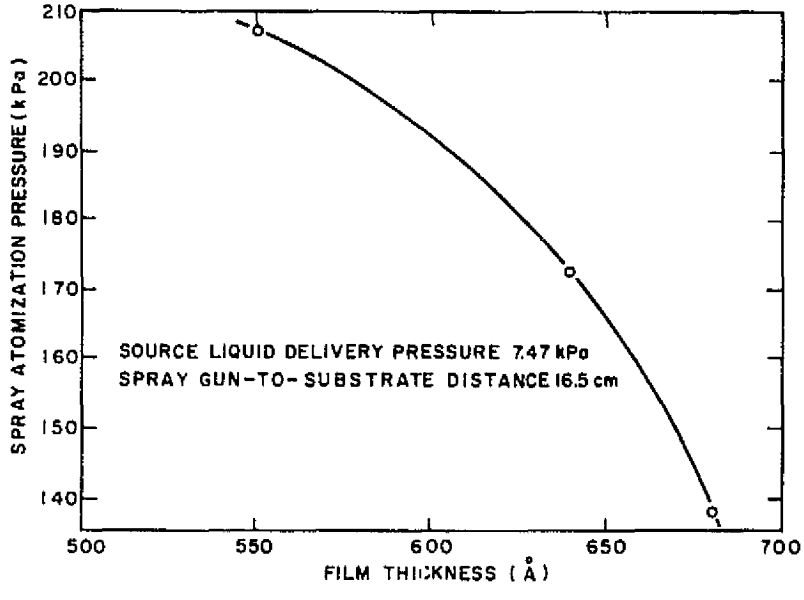

Figure 46. Effect of spray atomization pressure as a function of film thickness.

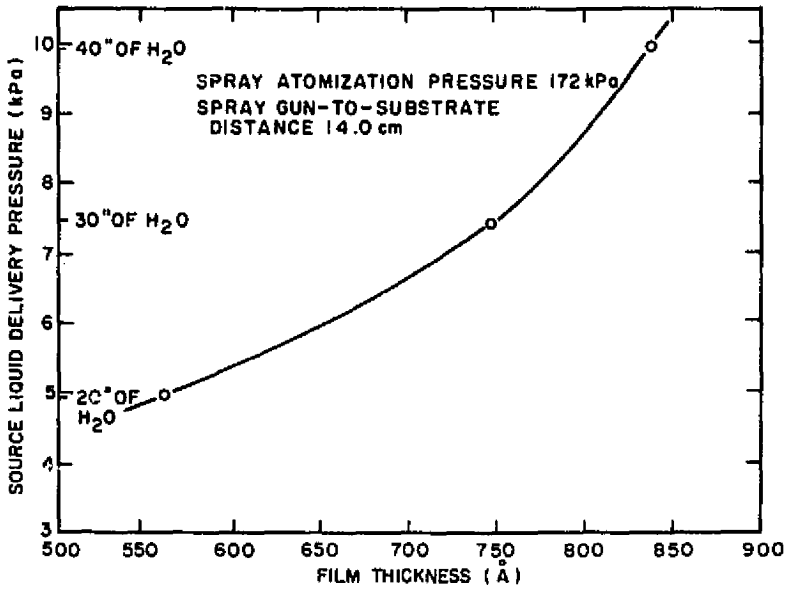

Figure 47. Effect of source liquid delivery pressure as a function of film thickness.

2. Metallization Bondability After AR Coating

The surface of the metallization grid collector pad must be free of AR coating in order to permit effective bonding of cell-to-cell interconnects. The simplest technique, suitable for laboratory applications, is masking the pad with a special solvent resistive polyethylene pressure tape with acrylic adhesive prior to spraying.* The tape tab is readily peeled off after coating but before heat treatments, leaving a clean and bondable surface.

Mechanical and chemical techniques can be used for automated high-speed processing. Selective mechanical removal of the AR coating can be accomplished by momentary application of an automatic ultrasonic vibrating or buffing tool combined with vacuum suction to remove the debris. Alternatively, since solder connection techniques are used which require fluxing of the bonding area, a flux composition could be formulated which contains a fluoride capable of selectively dissolving the thin AR coating. Rinsing with a jet of deionized water would prevent any subsequent metal corrosion.

*Tape No. 480, 3M Company, St. Paul, MN.

3. Cell Electrical Performance as a Function of AR Coating Type and Thickness

We have shown previously [18] that the solar-cell conversion efficiency is not markedly affected by the AR coating thickness in the range of 600 to 800 Å. Additional studies have been performed to extend the film thickness range and to compare RCA cells having screen-printed silver metallization with commercial OCLI cells* having conventional evaporated Ti/Pd/Ag metallization. The conversion efficiency of the AR-coated OCLI cells was determined by the usual I_{sc} and V_{oc} measurements under a standardized light source. The AR coating, consisting of SiO_x, was then stripped by etching briefly in buffered HF solution, followed by rinsing with deionized water, and spin drying. The cells were remeasured, AR recoated by us, and again measured. The ratio of J_{sc} measured after AR coating over J_{sc} of the bare cell before coating is taken as a convenient approximation of the change in conversion efficiency under standardized irradiation conditions.

The source preparations for depositing the AR coatings were RCA I titanium isopropoxide-based composition and commercial Emulsitone** "Titaniumsilicafilm C" solution. The RCA II titanium ethoxide-based alternative preparation was not included since it offers no advantages over RCA I, has a shorter shelf life, and is more expensive. Formulation of the source solutions, application by centrifugal spinning, heat treatment of the films, and ellipsometric measurements of refractive index and film thickness were performed as described previously [18]. Polished single-crystal silicon wafers were used as control substrates for the optical measurements.

The results for RCA cells with 10- to 18-μm-thick screen-printed silver metallization, AR coated with RCA I source solution, are summarized in Table 25. The effect of TiO_2 film thickness on the increase in current density ratio Γ (J_{sc} after coating/J_{sc} before coating) is shown graphically in Fig. 48. A broad maximum of $\Gamma = 1.39$ is attained with a film thickness of 700 Å. Film thickness measurements were done ellipsometrically on the cells as well as on analogously AR-coated polished silicon test wafers. The films on cells gave unreliable thickness readings that averaged 22% more, apparently due to the

18. R. V. D'Aiello, *Automated Array Assembly, Phase II*, Quarterly Report No. 4, prepared under Contract No. 954868 for Jet Propulsion Laboratory, October 1978.

*Space grade cells manufactured by Optical Coating Labs, Inc., Santa Clara, CA.
**Emulsitone Company, Whippany, NJ.

TABLE 25. INCREASE IN CELL EFFICIENCY AS A FUNCTION OF TiO_2 FILM THICKNESS FOR CELLS WITH SCREEN-PRINTED METALLIZATION

Source Liquid (type)	Solar Cell[1] (Å)	Film Thickness[2] (Å)	Refractive Index[2] (n)	Current Density Increase (Γ)	Conversion Efficiency[4] Before Coating (%)	After Coating (%)
RCA I[5]	501A-110	903	2.141	1.26	8.7	10.9
	501A-109	801	2.150	1.29	8.5	10.8
	501A-107	697	2.137	1.39	8.8	12.1
	501A-105	639	2.137	1.36	8.5	11.7
	501A-86	539	2.182	1.35	8.6	11.6
	501A-85	483	2.150	1.36	8.6	11.8

1. Screen-printed Ag metallization, 7.5-cm-diam RCA cells. Metal thickness: 8.0 μm.
2. Ellipsometric measurement on polished silicon test wafer; Hg light at λ = 5461 Å.
3. Ratio of J_{sc} after/before coating.
4. AM-1 simulation ELH lamp at 100 mW/cm^2.
5. Titanium isopropoxide-based, yielding TiO_2; post-deposition heat treatments 30 s each at 70, 200, and 400°C.

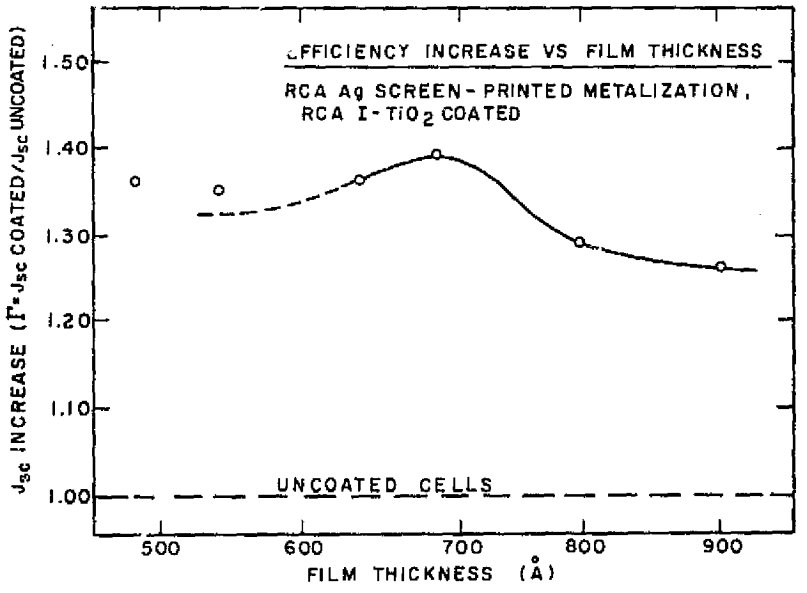

Figure 48. Electrical performance as a function of film thickness, 8-μm-thick vacuum-evaporated Ti/Pd/Ag metallization.

C-2

surface roughness of sawed and chemically etched silicon surfaces. The accurate film thicknesses measured on the smooth test wafers are considered more representative and were used for plotting the graphs in Figs. 48 and 49.

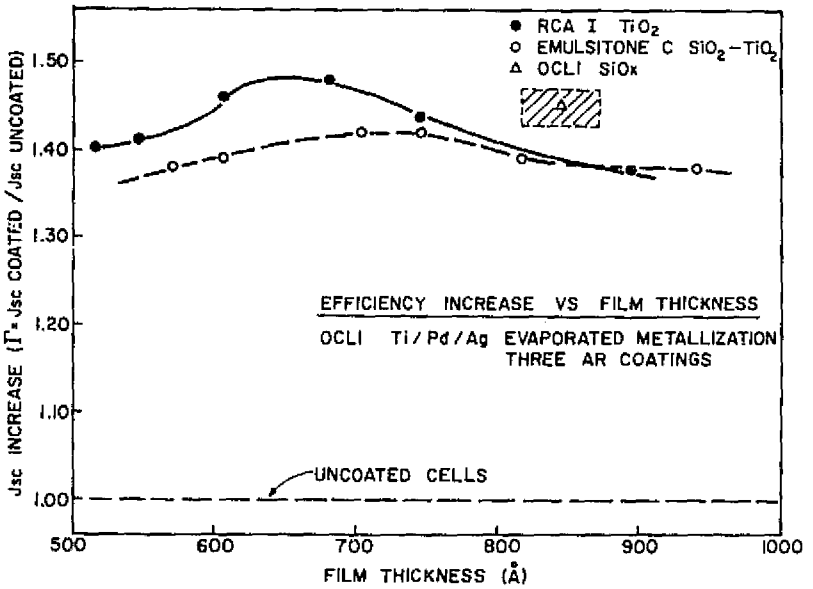

Figure 49. Electrical performance as a function of film thickness, 2.7-μm-thick vacuum-evaporated Ti/Pd/Ag metallization.

Stylus profilometric traces of typical RCA cell surfaces showed silicon roughness peaks of 0.4 μm at an average frequency of 9 peaks/mm horizontal distance, rendering step-height measurements of the thin AR film also unreliable. The ellipsometrically determined index of refraction averaged 2.15 for the test wafers and 2.18 for the cells. The cell conversion efficiency (η) averaged 8.6% before and 11.5% after TiO_2 coating.

The results we obtained for OCLI cells with 2.7-μm-thick vacuum-evaporated Ti/Pd/Ag metallization are presented in Table 26 and in Fig. 49. The effectiveness of the OCLI sputter-deposited SiO_x AR coating was determined by measuring the current density before and after chemical stripping of the coating. As indicated in Fig. 49, the ratio increase (Γ) averaged 1.45 for a nominal ellipsometric film thickness range of 820 to 870 Å. No test wafers with SiO_x were available for comparison. The cell conversion efficiency averaged 7.6% for bare cells and 11.0% for SiO_x coated cells.

TABLE 26. INCREASE IN CELL EFFICIENCY AS A FUNCTION OF AR FILM THICKNESS FOR CELLS WITH EVAPORATED METALLIZATION

Source Liquid (type)	Solar Cell[1] (No.)	Film Thickness[2] (Å)	Refractive Index[2] (n)	Current Density Incr.[3] (Γ)	Conversion Before Coating (%)	Efficiency[4] After Coating (%)
RCA I[5]	10	895	2.220	1.38	7.6	10.6
	11	745	2.204	1.44	7.6	10.8
	12	677	2.193	1.48	7.9	11.4
	9	605	2.218	1.46	7.4	10.8
	7	545	2.187	1.41	7.8	11.1
	8	515	2.165	1.40	7.4	10.3
Emulsitone C[6]	1	940	1.973	1.38	7.3	10.2
	2	816	1.950	1.39	7.6	10.6
	3	745	1.940	1.42	7.4	10.0
	4	702	1.929	1.42	7.8	10.9
	6	604	1.933	1.39	7.4	9.9
	5	572	1.916	1.38	7.6	10.3

1. Vacuum-evaporated Ti/Pd/Ag metallization, 7.5-cm-diam OCLI cells stripped of their AR coating. Profilometrically measured metal thickness is 2.7 μm.
2. Ellipsometric measurement on polished silicon test wafer; Hg light at λ = 5461 Å.
3. Ratio of J_{sc} after/before recoating.
4. AM-1 simulation ELH lamp at 100 mW/cm^2.
5. Titanium isopropoxide-based, yielding TiO_2; post-deposition heat treatments 30 s each at 70, 200, and 400°C.
6. Emulsitone "Titaniumsilicafilm C" yielding $SiO_2 \cdot TiO_2$; post-deposition heat treatments 30 s each at 70, 200, and 400°C.

Recoating the cells with RCA I TiO_2 led to a peak increase of Γ of at least 1.48, centered between 625- and 675-Å film thickness. Recoating with Emulsitone TiO_2-SiO_2 led to a Γ maximum of 1.42 for a film thickness between 700 and 740 Å. The film thicknesses stated were obtained from ellipsometrically measured silicon test wafers. Measurements on cells again deviated, but in the opposite direction than observed for RCA cells: OCLI cells averaged 17% *less* than the test wafers. Stylus profilometery indicated a cell surface roughness of typically 0.6 μm with a frequency averaging 14 peaks/mm horizontal distance.

Ellipsometric measurements of the refractive index of the AR films also gave differences between test wafer substrates and OCLI cells: RCA I TiO_2 averaged an index of 2.20 on test wafers and "2.37" on cells; Emulsitone C TiO_2-SiO_2 was 1.94 on test wafers and "2.26" on cells; OCLI SiO_x measured "1.81" on cells, which corresponds to 1.55 to 1.69 on test wafers if corrected on the basis of the TiO_2-SiO_2 and the TiO_2 differences noted.

The OCLI cell conversion efficiency averaged 7.6% without AR coating, 10.8% with RCA I TiO_2, and 11.0% with OCLI SiO_x. The values for Emulsitone TiO_2-SiO_2 are somewhat lower, averaging 10.3%.

Several conclusions can be derived from these results:

(1) Comparison of the effectiveness of TiO_2, TiO_2-SiO_2, and SiO_x AR coatings on commercial thin-film metallized cells showed that TiO_2 from RCA I solution is superior to both Emulsitone TiO_2-SiO_2 and OCLI SiO_x. Maximal Γ values are 1.48+ at 625 to 675 Å, 142 at 700 to 740 Å, and 1.45 at 820 to 870 Å, respectively.

(2) Screen-print metallized RCA cells with RCA I TiO_2 coating exhibited a maximal Γ value of 1.39 at 700 Å. This apparently lower value is due to the higher initial cell conversion efficiency of RCA cells (8.6%) than that of OCLI cells (7.6%). However, the final conversion efficiency after coating increased to 11.5% for RCA cells, but to only 10.8% for OCLI cells.

(3) The conversion efficiency for OCLI cells recoated with RCA I TiO_2 exhibited a maximum efficiency of 11.4% for a film thickness of 700 Å.

(4) The conversion efficiency for OCLI cells with their more expensively produced SiO_x coating averaged 10.9% for the presumably optimal thickness of these films. A greater effectiveness should really be expected for a physically vapor-deposited AR coating. Reduced scattering losses result from the more uniform coverage attainable, especially in comparison to the centrifugal spinning over thick-film metallized cells as used in this analytical study.

(5) The new results we obtained again emphasize the relative noncriticality of the AR film thickness. For example, the cell efficiency of RCA I TiO_2 recoated OCLI cells, averaged over the entire tested film thickness range from 500 to 900 Å, is a remarkable 10.8%

(without indications of drastic decreases beyond this range), as compared to 11.4% for the maximum at about 700 Å.

(6) Ellipsometric measurements of thickness and refractive index of AR coatings on microscopically nonplanar cell surfaces are not reliable due to optical causes. Control measurements must be performed on polished silicon test wafers and correlated with cell values as was done in our present work. Alternatively, a macroscopic interferometric reflection technique of a relatively large area of the silicon cell surface may be more appropriate for direct in-line process control applications.

4. Heat-Treatment Effects and Characterization of AR Films

Effects of additional heat treatments on cell efficiency and AR film properties are being examined to ascertain whether further improvements could be achieved. The cells and silicon test wafers described in the subsection above were used for this purpose. As noted, these samples had been heat-treated after film deposition by exposure in room air to 70°C on a hot plate for 0.5 min, followed by heating at 200°C for 0.5 min, and finally by heating at 400°C for 0.50 min. Additional heating was done at 400°C for 5 min, followed by cell measurements and film analyses. A third heat treatment at 400°C was then performed for 50 min to extend the time again by a factor of 10, followed by final measurements and analyses.

SECTION V

PANEL ASSEMBLY

A. BACKGROUND

To meet the requirements for a 20-year life and to provide mechanical strength for simply supported large panels, RCA has selected a double-glass panel design. The details of this design are shown in Fig. 50. Based on cost analysis and experimental comparisons, the safety glass lamination process emerged as the preferred panel assembly technique.

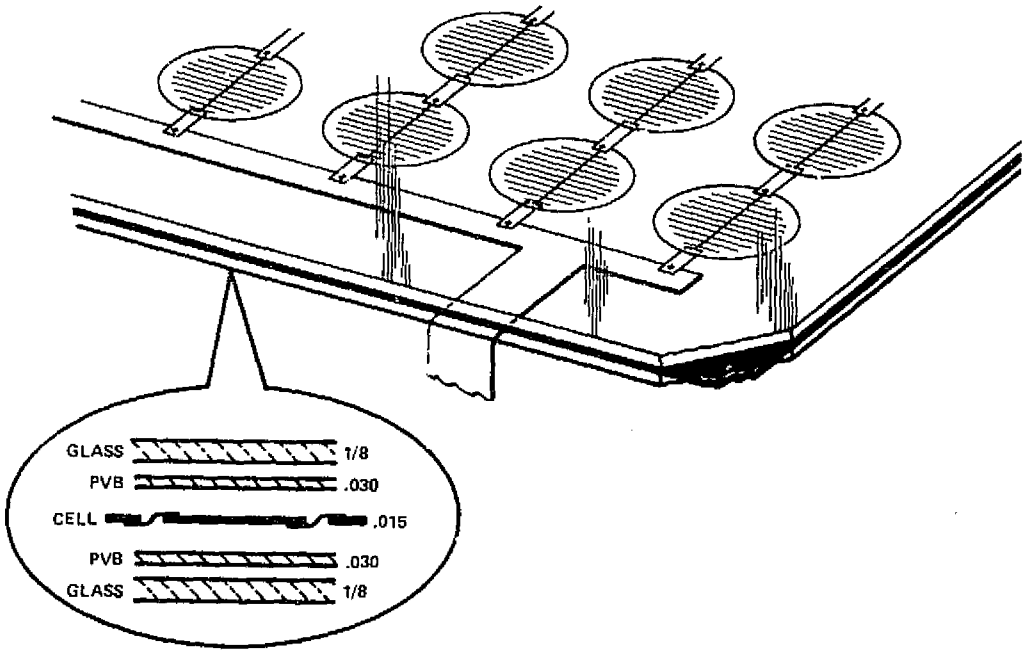

Figure 50. Solar-panel configuration.

The basic approach is to encapsulate the cells in the same polyvinyl butyral (PVB) resin that is used for safety glass. The technology of laminating two sheets of untempered glass with a 0.015-in. sheet of PVB is widely used for automotive and architectural applications. Current production rates of PVB are equivalent to more than 1000 MW/yr; thus the midterm requirements for PVB would not have an impact on cost and supply.

The refractive index of PVB is 1.48 which is an excellent match to the index of soda lime of 1.50. There are various grades of PVB with UV absorbing

compounds added to protect fabrics from yellowing. However, above 0.40 UV transmission tests indicate no detectable interface reflectance between PVB and glass. In the PVB compounds without UV absorbing materials there has never been a report of UV yellowing. Since PVB has been in service for more than 20 years, it appears that this material will achieve the JPL life goals.

We began our search for a workable process by using the laminators' standard process for the fabrication of safety glass. It consists of drawing a vacuum to 27 in. Hg, heating the PVB to 107°C, and applying 50-psig hydrostatic pressure. This process is optimum for glass sandwiches that do not contain inclusion such as solar cells, so that glass or cells were often cracked and air bubbles or voids were found between and around cells. The experiments and verification runs described below show that a successful modification consists of an initial phase of high vacuum to remove a large fraction of the trapped air, low laminating pressure, followed by a high softening temperature and pressure during the autoclaving phase.

B. EXPERIMENTAL LAMINATIONS AND VERIFICATION

To illustrate the effectiveness of this modified laminating process, a small 9-cell array was laminated between 2 sheets of 1/8-in.-thick float glass and two sheets of 15-mil-thick PVB using 21-mil-thick (versus the standard 15 mil) 3-in.-diameter cells. Two 0.25-in.-thick glass pressing plates are employed to prevent deflecting the glass at the edges of the panel. The first stage of the lamination was done in a vacuum bag maintained at an absolute pressure of 5-mm Hg. The vacuum was drawn down for 1 hour prior to heating to 140°C. The heat- and vacuum-induced laminating pressure of 14.6 psi was maintained overnight. Then the heat was turned off and the vacuum maintained for another hour during cool down. The PVB flowed completely around all cells with only a few rarefied bubbles remaining. The laminate was then autoclaved at 140°C and 150-psig hydrostatic pressure in a vacuum bag. The resulting laminate was totally bubble-free.

Interestingly, due to the long duration of the lamination (>14 h) and slight inclination of the panel in the oven (<15°) the array of cells "slid" about 1/2 in. out of bottom of the panel, which illustrates the low viscosity of the PVB at 140°C. Also, a considerable amount of PVB extruded out of the

sandwich at the edges, resulting in a thinner layer of PVB between the glass sheets than if it were contained by an edge cell.

These experiments have shown that under appropriate conditions, PVB will flow readily, even beyond the extent required to fill the voids between the cells. In fact, to fill the voids only, for laminating 21-mil-thick cells using two sheets of 15-mil-thick PVB, a 13.3% displacement of PVB is required. Under the same conditions, laminating 15-mil-thick cells using two sheets of 10-mil-thick PVB, only 14.3% PVB displacement is necessary. This suggests that it should be possible to accomplish lamination with 0.010-in. PVB; however, thermal stress considerations may preclude use of this thickness.

Lamination experiments were then begun at a vendor's* location using a small (16- x 46-in.) autoclave especially set up for our use. In the initial experiments, 1- x 3-ft panels containing blank 3-in.-diameter silicon wafers, 15 mil thick, were laminated. A silicone bag designed for this application was used in the preautoclaving phase to apply the vacuum and to hold the panel and the 1/4-in.-thick glass pressing plates. The procedures outlined in the previous paragraphs were then used with reductions in the time for each phase.

This procedure was successful in that no glass or wafers cracked and no air bubbles or voids were found in the panels. The steps were repeated seeking minimum times for each phase of the lamination. It was found, for example, that for a 1- x 3-ft panel, the time for the application of initial vacuum can be reduced to 10 min.

This lamination schedule was then applied to fabricate two 12- x 38-in. panels containing an interconnected array of 44 (11 x 4, series-parallel) live 3-in.-diam solar cells. A photograph of one of these panels after lamination is shown in Fig. 51.

Larger panels ∿4 x 4 ft were also laminated; in this case, a production size 6-ft-diam autoclave was used. It was found that the procedures used for the smaller 1- x 3-ft panels are applicable to the large autoclave for the 4- x 4-ft panel. A photograph of a completed panel containing 210 screen-printed cells is shown in Fig. 52. In that panel, the one cracked cell (fourth column, second row from the top) was broken during the soldering of the array, and the flow of the PVB during lamination caused the pieces to

*Saftee-Glass, a division of Chromalloy, King of Prussia, PA.

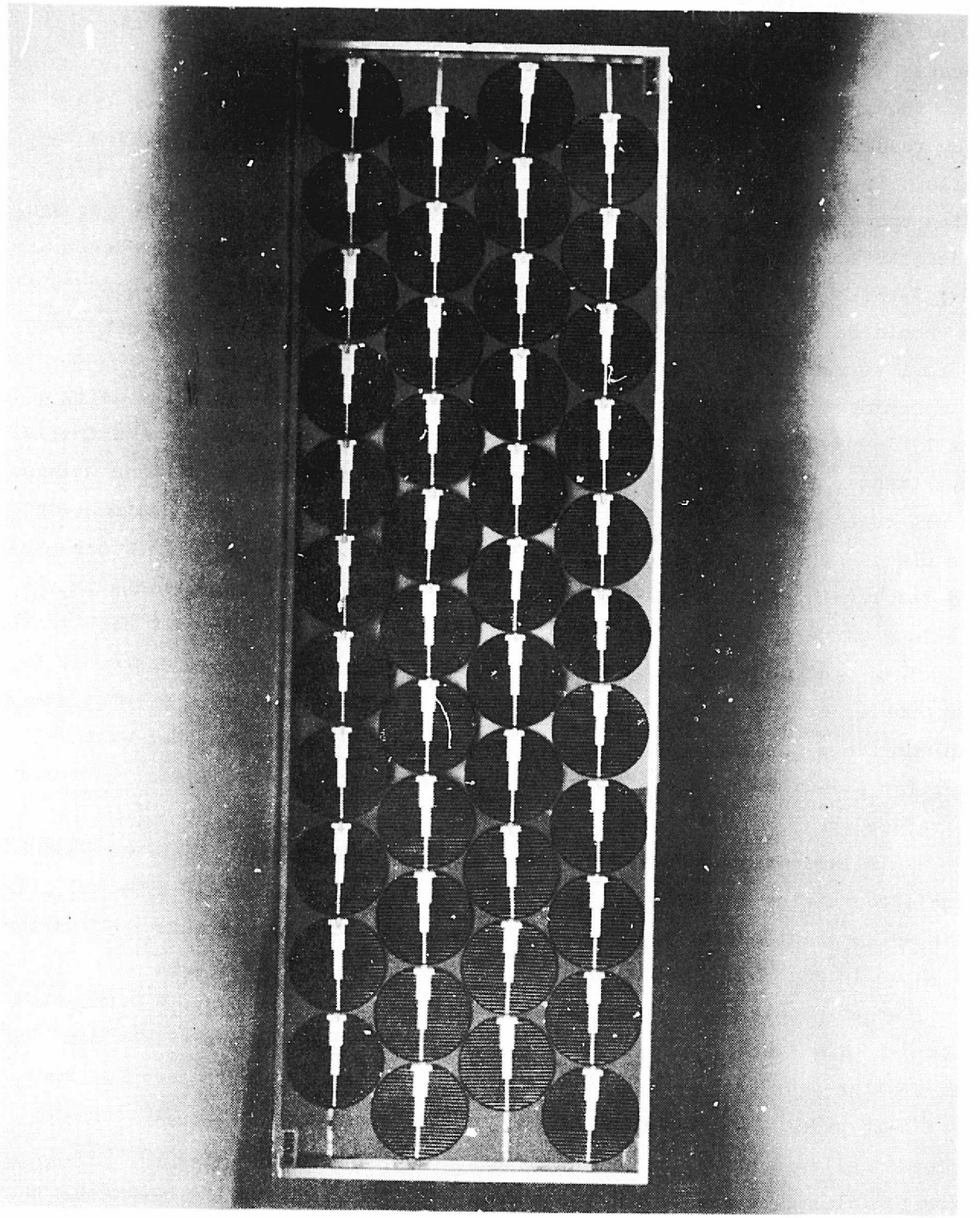

Figure 51. A 12- x 38-in. panel after lamination.

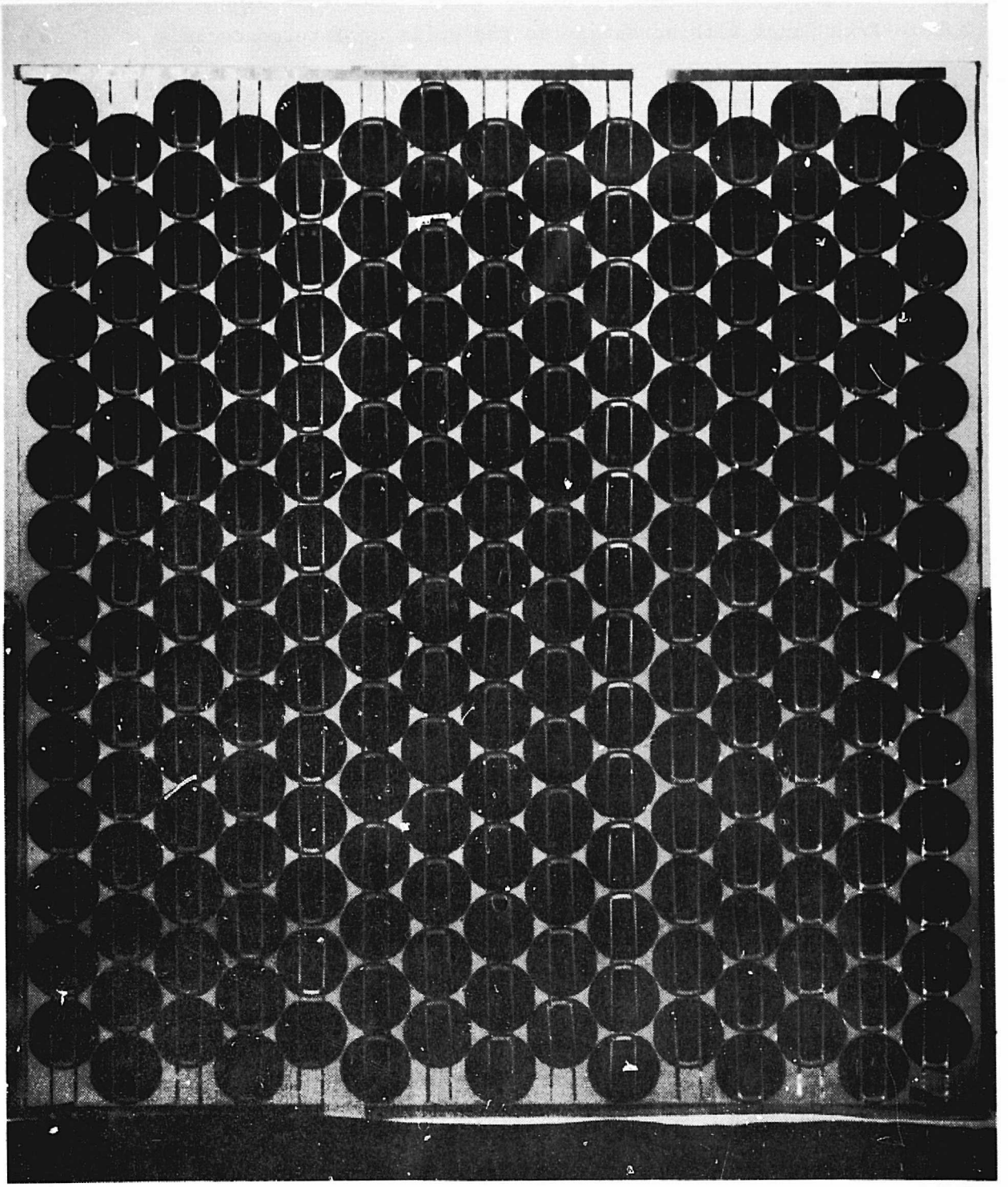

Figure 52. Completed solar panel with 210 screen-printed cells.

separate. However, it can be seen that the lamination produced a clear, bubble-free panel with no damage to the cells or interconnects.

C. PROCESS SPECIFICATION

A process specification detailing the panel assembly procedures was written and is available upon request from the Processes and Equipment Development Area of the JPL-LSA Project.

SECTION VI

CONCLUSIONS

Detailed technical conclusions relating to the processes investigated are included in the sections describing the development and verification of each process. In this section, discussion will be limited to the salient features regarding technological readiness or cost effectiveness.

A. JUNCTION FORMATION - ION IMPLANTATION

The range of implant parameters and two furnace-annealing techniques were determined which result in solar cells having AM-1 efficiencies of 14 to 15%. The results show that solar cells of high quality can be reproducibly fabricated using ion-implantation for the junction formation. Although a modern implantation machine was used in this work, the throughput of that machine, 60 per h, is low compared to that required for a truly low-cost process. In addition, the furnace-annealing techniques used here are somewhat complex, so that future work on the ion-implantation process should be directed toward simplified annealing procedures.

B. THICK-FILM SCREEN-PRINTED METALLIZATION

Our program has resulted in the synthesis of silver-based inks suitable for contacting the n and p side of solar cells. The processing parameters for the use of infrared-lamp firing were explored and were found to have sufficiently wide tolerance to make this an acceptable process. There are, however, limitations caused by the contact-formation process which primarily reduces the cell fill factor thereby lowering the efficiency of screen-printed solar cells. For silver inks, there is a need for further work to improve the understanding of contact mechanisms as was illustrated by the dramatic increase in fill factor caused by hydrofluoric acid rinsing. With regard to the ink, the use of non-noble metals should be explored to reduce material costs.

C. SPRAY-ON AR COATING

Low-cost solutions were developed which were successfully tested with commercially available spray-coating machines. The specifications for liquid source solution, machine parameters, film curing conditions, and the range of film thickness and refractive index have been determined. Our estimates for production rates of 10 to 30 MW/yr place the cost for this process at ∿ $0.015/W.

D. PANEL ASSEMBLY - DOUBLE-GLASS LAMINATION

We now consider this process to be technically verified in that the process steps required to successfully laminate large-area, up to 4 x 4 ft, double-glass panel structures containing live, interconnected cells have been determined. Clear, bubble-free panels have been fabricated, but no significant accelerated life-testing has been conducted on these panels to date. The laminations described in this report were conducted at a vendor location with commercial equipment designed for the fabrication of safety glass in a variety of sizes. This equipment was suitable for testing our process; however, since we have determined a workable process, machines can now be designed specifically for solar-panel laminations which will decrease processing time and increase throughput.

REFERENCES

1. ASTM Tentative Test Method F391 for Minority Carrier Diffusion Length in Silicon by Measurement of Steady-State Surface Photovoltage, *1976 Annual Book of ASTM Standards*, Part 43, Electronics (1976).

2. The diffusion length L is obtained from a best parameter fit of the measured quantum efficiency data to the diffusion-only equations described by H. J. Hovel, "Solar Cells: Carrier Collection, Spectral Response and Photocurrent", Chapter 2 in *Semiconductor Devices*, Vol. 11, Edited by Willardson and Beer.

3. A. S. Grove, *Physics and Technology of Semiconductor Devices*, (Wiley-Interscience, New York, 1967), Chapter 6.

4. E. C. Douglas and A. G. F. Dingwall, "Ion Implantation for Threshold Control in COSMOS Circuits," IEEE Trans. Electron Devices ED-21, 324 (1974).

5. R. H. Kingston, "Switching Time in Junction Diodes and Junction Transistors," Proc. IRE 42, 829 (1954). Also see B. Lax and S. F. Neustadter, "Transient Response of a P-N Junction," J. Appl. Phys. 25, 1148 (1954) and R. H. Dean and C. J. Nuese, "A Refined Step-Recovery Technique for Measuring Minority Carrier Lifetimes and Related Parameters in Asymmetric P-N Junction Diodes," IEEE Trans. Electron Devices ED-18, 151 (1971).

6. M. S. Bae and R. V. D'Aiello, "P^+/N High-Efficiency Silicon Solar Cells," Appl. Phys. Lett. 31, 285 (1977).

7. D. R. Rupprecht and J. Stach, "Oxidized Boron Nitride Wafers as an In-Situ Boron Dopant for Silicon Diffusions," J. Electrochem. Soc. 120, 1266 (1973).

8. J. Stach and J. Krusest, "A Versatile Boron Diffusion Process," Solid State Technol. 19, 60 (October 1976).

9. Technical Note, "Hydrogen Injection Process Low Temperature 725°C-975°C," Form C715, June 1978, The Carborundum Co., Graphite Products Division, P. O. Box 577, Niagara Falls, New York 14302.

10. A. Kirkpatrick, "Process Specification for High Efficiency Implanted 3" Diameter Cells," Proceedings: 9th Project Integration Meeting, LSA Low Cost Solar Array Project, JPL, April 11-12, 1978. (See page 4-104 of Proceedings.)

11. D. Helmreich and E. Sirtl, "Oxygen in Silicon: A Modern View," Semiconductor Silicon 1977, Proceedings of the 3rd International Symposium on Silicon Materials Science and Technology, The Electrochemical Society, Inc., P. O. Box 2071, Princeton, N.J. 08540. (Article located on Pages 626 to 636.)

12. M. Watanabe, H. Muraoka, and T. Yonezawa, "Perfect Crystal Technology," Proceedings of the 6th Conference on Solid State Devices, Tokyo, 1974, Supplement to the Journal of the Japan Society of Applied Physics, Vol. 44, 269 (1975).

13. T. Yonezawa, M. Watanabe, Y. Koshino, H. Ishida, H. Muraoka, and T. Ajina, "High Concentration Diffusion without Generation of Crystal Defects," Proceedings of the Third International Symposium on Silicon Materials Science and Technology, Philadelphia, PA, 1977. *Semiconductor Silicon 1977*, Vol. 77-2, p. 658, The Electrochemical Society, Princeton, NJ.

14. A Goetzberger and W. Shockley, "Metal Precipitates in Silicon P-N Junctions," J. Appl. Phys. 31, 1821 (1960). See also M. N. Nakamura and T. Kato, "A Study of Gettering Effect of Metallic Impurities in Silicon," Japan J. Appl. Phys. 7, 512 (1968) and E. L. MacKenna, "Silicon and Silicon Dioxide Gettering in Perspective," Extended Abstract No. 216, Electrochem. Soc. Vol. 74-2, October 1974.

15. J. Lindmayer, "Development of 20% Efficient Solar Cells," Final Project Report NSF/RANN/SE/GI-43090/FR/75/2, NSF Grant GI-43090, October 1975

16. J. Lindmayer, "Theoretical and Practical Fill Factors in Solar Cells," Comsat Tech. Rev., Vol. 2, No. 1, pp. 105-121, Spring 1972.

17. K. R. Bube and T. T. Hitch, "Basic Adhesion Mechanisms in Thick and Thin Films," Final Report, March 1978, NASA Contract N00019-77-C-0176.

18. R. V. D'Aiello, *Automated Array Assembly, Phase II*, Quarterly Report No. 4, prepared under Contract No. 954868 for Jet Propulsion Laboratory, October 1978.

APPENDIX A

DATA FROM SOLAR-CELL EXPERIMENTS

Table A-1 presents the results of measurements made on the various solar cells fabricated during the course of this experimental study. The Wacker wafers used were cut from boules prepared using float-zone processing, and the Monsanto and RCA Mountaintop wafers were cut from boules prepared using Czochralski processing. The notation WAC1-3 indicates a 1- to 3-ohm-cm Wacker wafer. The column describing implant conditions lists the front-side implant first. BG refers to the backside boron glass step produced using Process B.

Figure A-1 shows an example of the measurements used to obtain the values of conversion efficiency η, short-circuit current density J_{sc}, open-circuit voltage V_{oc}, and fill factor FF. Equations (1) and (2) in the main body of this report were used to find η and FF given the raw data values of V_{oc}, I_{sc}, V_m, I_m and A = 4.5 cm^2.

When measuring lifetime τ and diffusion length $L = \sqrt{D\tau}$ in the cells, the diode-reverse-recovery (drr) method[5] was used initially to obtain τ in finished cells. The surface photovoltage method (spv)[1] was eventually adopted as the method for measuring the diffusion length directly in starting wafers (before processing), and a parameter fit to the quantum efficiency curve (QE)[2] was adopted as the method for measuring the value of the diffusion length in the bulk after processing.

The antireflection coatings used on these cells were formed using the spin-on technique. The emulsion material used was Titaniasilica Type C which is commercially available from Emulsitone. After spinning on and baking for 15 min at 400°C, the resulting AR coating thickness is 0.075 μm.

TABLE A-1. DATA FROM ION-IMPLANTED SILICON SOLAR CELLS

Cell	Implant Conditions	Anneal Conditions	η (%)		J_{sc} (mA/cm^2)		V_{oc} (mV)		FF		T(μs)
			No AR	AR	No AR	AR	No AR	AR	No AR	AR	drr
S3a	5 keV ^{75}As 1.5×10^{15} fs	875°C, 15 min SiO_2+0.2 μm Silane Cap									
CZ	10 / 100 keV ^{11}B 1×10 / 2.5×10^{15} bs	950°C Anneal-15 min O_2, 45 min N_2 + 10 min slow pull	7.9	9.6	20.5	30.6	530	535	0.693	0.586	0.5
S3b Float	Same	Same	7.7	10.7	19.8	28.8	527	542	0.714	0.666	0.5
S1a	5 keV ^{31}P 1.5×10^{15} fs										
CZ	10 / 100 keV ^{11}B 1×10^{15} / 2.5×10^{15} bs	Same	6.0	8.7	16.3	23.0	500	508	0.701	0.684	
S1b Float	Same	Same	7.8	11.8	18.5	26.5	540	555	0.745	0.742	
S2	5 keV ^{31}P 0.75×10^{15} fs 10 / 100 keV ^{11}B 1×10^{15} / 2.5×10^{15} bs	Same	9.0	12.6	20.2	29.7	553	566	0.774	0.728	2.0
S4	5 keV ^{75}As 0.75×10^{15} fs Same	Same	7.0	9.7	18.1	26.4	522	532	0.714	0.671	2.0
S5	5 keV ^{75}As 5.6×10^{15} fs Same	No Deposited Cap but Same anneal	7.4	10.9	17.9	25.9	518	530	0.776	0.776	
IISS11 WAC 1-3	5 keV ^{31}P 1.5×10^{15} fs 20 / 100 keV ^{11}B 1×10^{15} / 2.5×10^{15} bs	0.5 μm Silane cap fs, 0.7 μm on bs 900°C Drive for 30 min	5.1		18.2		450		0.623		0.2
IISS13 WAC 1-3	5 keV ^{31}P $.75\times10^{15}$ fs 20 / 100 keV ^{11}B 1×10^{15} / 2.5×10^{15} bs	Same	7.3	10.3	18.4	27.5	506	510	0.760	0.733	0.15
IISS14 WAC 1-3	5 keV ^{31}P 1.5×10^{15} fs Boron Glass bs	0.5 μm Silane Cap fs 900°C Drive for 30 min	8.8	12.3	21.3	28.3	525	550	0.784	0.772	2.1
IISS15	5 keV ^{31}P 1.5×10^{15} fs	0.5 μm Silane Cap fs									
WAC 1-3	Boron Glass bs	900°C Drive for 30 min	9.3	13.4		29.7	540	568	0.785	0.77	
IISS16	5 keV ^{31}P 0.75×10^{15} fs	0.5 μm Silane Cap fs									
WAC 1-3	Boron Glass	900°C Drive for 30 min	8.6	12.7	20.9	31.5	540	542	0.765	0.742	

TABLE A-1. DATA FROM ION-IMPLANTED SILICON SOLAR CELLS (Continued)

Cell	Implant Conditions	Anneal Conditions	η (%)		J_{sc} (mA/cm^2)		V_{oc} (mV)		FF		τ(μs)	L(μm)	
			No AR	AR	No AR	AR	No AR	AR	No AR	AR	drr	SPV Before	QE After
IISS17	5 keV ^{31}P $5x10^{14}$	0.5 μm Silane Cap 900°C 30 min Drive											
WAC 1-3	BG	+ 800°C BG Dep + Slow Pull	9.1	13.0	21.4	29.8	545	562	0.757	0.755	11.5		206
IISS18	5 keV ^{31}P $7.5x10^{14}$												
WAC 1-3	BG		9.1	13.6	21.0	30.7	545	570	0.772	0.75	10.9		
IISS19	5 keV ^{31}P $1.5x10^{15}$												
WAC 1-3	BG		9.3	13.9	21.2	30.7	550	568	0.773	0.77	13.1		
IISS20	5 keV ^{31}P $5x10^{14}$	1000°C 30 min Drive											
WAC 1-3	BG	+ Slow Pull	9.7	13.5	21.2	30.2	565	575	0.788	0.76	15.0		
IISS21	5 keV ^{31}P $7.5x10^{14}$												
WAC 1-3	BG		9.0	13.1	21.2	30.0	545	570	0.756	0.745	17.9		
IISS22	5 keV ^{31}P $1.5x10^{15}$												
WAC 1-3	BG												
IISS23	5 keV ^{31}P $7.5x10^{14}$												
MON 1-3	BG	900°C	8.4	12.6	21.4	30.7	535	568	0.712	0.70	12.2		
IISS24	5 keV ^{31}P $1.5x10^{15}$												
MON 1-3	BG	900°C	9.3	13.3	21.1	30.6	548	580	0.778	0.74	12.1		
IISS25	5 keV ^{31}P $7.5x10^{14}$												
MON 1-3	BG	1000°C											
IISS26	5 keV ^{31}P $1.5x10^{15}$												
MON 1-3	BG	1000°C	9.0	13.1	20.5	28.9	542	570	0.784	0.77	9.8		

TABLE A-1. DATA FROM ION-IMPLANTED SILICON SOLAR CELLS (Continued)

	Cell	Implant Conditions	Anneal Conditions	η (%)		J_{sc} (mA/cm^2)		V_{oc} (mV)		FF		L(μm)	
				No AR	AR	No AR	AR	No AR	AR	No AR	AR	SPV Before	QE After
2-in. Cells	IISS27	5 keV ^{31}P $2x10^{14}$											
	WAC 1-3	BG	900°C - 25 min, 10 min slow cool		10.0		32		540		0.56		301
	IISS28	5 keV ^{31}P $2x10^{14}$											
	WAC 1-3	BG	1000°C - 25 min, 10 min slow cool		11.6		32		550		0.65		
	IISS29	5 keV ^{31}P $1x10^{15}$											
	WAC 1-3	BG	900°C - 25 min, 10 min slow cool		10.3		31.6		540		0.59		
	IISS30	5 keV ^{31}P $1x10^{15}$											
	WAC 1-3	BG	1000°C - 25 min, 10 min slow cool		13.1		31.4		562		0.72		
	IISS31	5 keV ^{31}P $5x10^{15}$											
	WAC 1-3	BG	900°C - 25 min, 10 min slow cool		14.8		31.4		578		0.79		
	IISS32	5 keV ^{75}As $5x10^{15}$											
	WAC 1-3	BG	1000°C - 25 min, 10 min slow cool						BROKEN				
	IISS33	5 keV ^{75}As $2x10^{14}$											
	WAC 1-3	BG	1000°C - 60 min, 10 min slow cool		8.4		32.2		542		0.47		
	IISS34	5 keV ^{75}As $2x10^{14}$											
	WAC 1-3	BG	1050°C - 60 min, 10 min slow cool		12.0		31.1		556		0.67		
	IISS35	5 keV ^{75}As $1x10^{15}$											
	WAC 1-3	BG	1000°C - 60 min, 10 min slow cool		13.4		31.8		565		0.73		
	IISS36	5 keV ^{75}As $1x10^{15}$											
	WAC 1-3	BG	1050°C - 60 min, 10 min slow cool		14.2		31.3		578		0.76		
	IISS37	5 keV ^{75}As $5x10^{15}$											
	WAC 1-3	BG	1000°C - 60 min, 10 min slow cool						BROKEN				
	IISS38	5 keV ^{75}A $5x10^{15}$											
	WAC 1-3	BG	1050°C - 60 min, 10 min slow cool		14.0		30.7		580		0.76		

TABLE A-1. DATA FROM ION-IMPLANTED SILICON SOLAR CELLS (Continued)

	Cell	Implant Conditions	Anneal Conditions	η (%) No AR	η (%) AR	J_{sc} (mA/cm^2) No AR	J_{sc} (mA/cm^2) AR	V_{oc} (mV) No AR	V_{oc} (mV) AR	FF No AR	FF AR	L (μm) SPV Before	L (μm) QE After
2-in. Cells	IISS39	5 keV $1x10^{15}$ ^{31}P											
	MON 1-3	BG	1000°C - 25 min, 10 min slow cool										
	IISS40	5 keV $1x10^{15}$ ^{31}P											
	MON 1-3	BG	1000°C - 25 min, 10 min slow cool										
	IISS41	5 keV $1x10^{15}$ ^{31}P											
	MON 1-3	BG	1000°C - 25 min, 10 min slow cool										
	IISS42	5 keV $1x10^{15}$ ^{75}As											
	MON 1-3	BG	1050°C - 60 min, 10 min slow cool										
	IISS43	5 keV $1x10^{15}$ ^{75}As											
	MON 1-3	BG	1050°C - 60 min, 10 min slow cool										
	IISS44	5 keV $1x10^{15}$ ^{75}As											
	MON 1-3	BG	1050°C - 60 min, 10 min slow cool										
	IISS45	5 keV $1x10^{15}$ ^{31}P											
	MON 1-3	BG	900°C - 25 min, 10 min slow cool										
	IISS46	5 keV $1x10^{15}$ ^{31}P											
	MON 1-3	BG	900°C - 25 min, 10 min slow cool	6.9		19.6		552		0.634			
	IISS47	5 keV $1x10^{15}$ ^{31}P											
	MON 1-3	BG	1000°C - 25 min, 10 min slow cool										
	IISS48	5 keV $1x10^{15}$ ^{31}P											
	MON 1-3	BG	1000°C - 25 min, 10 min slow cool										
3-in. Cells	IISS49	5 keV $5x10^{15}$ ^{31}P											
	MON 1-3	BG	900°C - 25 min, 10 min slow cool										
	IISS50	5 keV $5x10^{15}$ ^{31}P											
	MON 1-3	BG	900°C - 25 min, 10 min slow cool	6.8		18.6		550		0.662			
	IISS51	5 keV $5x10^{15}$ ^{31}P											
	MON 1-3	BG	1000°C - 25 min, 10 min slow cool	7.6		18.2		565		0.739			
	IISS52	5 keV $5x10^{15}$ ^{31}P	1000°C - 25 min, 10 min slow cool	7.3		18.1		556		0.725			
	IISS53		1000°C - 25 min, 10 min slow cool	7.1		18.4		562		0.685			
	MON 1-3	BG											

I_{SHUNT} very high due to misaligned metal

Actual functioning area 41.85 cm^2

Used new ^{11}B boron glassing furnace

TABLE A-1. DATA FROM ION-IMPLANTED SILICON SOLAR CELLS (Continued)

Cell	Implant Conditions	Anneal Conditions	η (%)		J_{sc} (mA/cm^2)		V_{oc} (mV)		FF		L(μm)	
			No AR	AR	No AR	AR	No AR	AR	No AR	AR	SPV Before	QE After
IISS54 WAC 1-3	$2x10^{14}$ ^{31}P $2x10^{14}$ ^{75}As 5 keV	900°C, 30 min		10.3		32.3		552		0.59		
IISS55 WAC 1-3	$2x10^{14}$ ^{31}P $2x10^{14}$ ^{75}As 5 keV	1000°C, 30 min		12.5		31.9		565		0.68		
IISS56 WAC 1-3	$4x10^{14}$ ^{31}P 5 keV	900°C, 30 min		10.2		31.6		548		0.57		266
IISS57 WAC 1-3	$4x10^{14}$ ^{31}P 5 keV	1000°C, 30 min		11.9		31.1		560		0.56		
IISS58 WAC 1-3	$1x10^{15}$ ^{31}P $1x10^{15}$ ^{75}As 5 keV	900°C, 30 min		14.1		32.8		572		0.75		
IISS59 WAC 1-3	$1x10^{15}$ ^{31}P $1x10^{15}$ ^{75}As 5 keV	1000°C, 30 min		14.6		32.4		583		0.75		
IISS60 WAC 1-3	$2x10^{15}$ ^{31}P 5 keV	900°C, 30 min		14.4		31.9		577		0.76		
IISS61 WAC 1-3	$2x10^{15}$ ^{31}P 5 keV	1000°C, 30 min		14.9		31.9		587		0.78		
IISS62 WAC 1-3	$2.5x10^{15}$ ^{31}P $2.5x10^{15}$ ^{75}As 5 keV	900°C, 30 min		14.9		31.8		583		0.78		
IISS63 WAC 1-3	$2.5x10^{15}$ ^{31}P $2.5x10^{15}$ ^{75}As 5 keV	1000°C, 30 min		15.0		31.1		590		0.73		
IISS64 WAC 1-3	$5x10^{15}$ ^{31}P 5 keV	900°C, 30 min		14.9		30.7		594		0.79		
IISS65 WAC 1-3	$5x10^{15}$ ^{31}P 5 keV	1000°C, 30 min		14.3		30.8		597		0.78		

TABLE A-1. DATA FROM ION-IMPLANTED SILICON SOLAR CELLS (Continued)

Cell	Implant Conditions	Anneal Conditions	η (%)		J_{sc} (mA/cm^2)		V_{oc} (mV)		FF		L(μm)	
			No AR	AR	No AR	AR	No AR	AR	No AR	AR	SPV Before	QE After
IISS66	5 keV $5x10^{14}$ ^{31}P											
WAC 1-3	BG	900°C for 30 min	BROKEN									
IISS67	5 keV $1x10^{15}$ ^{31}P											
WAC 1-3	BG	900°C for 30 min	9.4	13.1	21.3	30.7	570	565	0.773	0.733		
IISS68	5 keV $5x10^{15}$ ^{31}P											
WAC 1-3	BG	900°C for 30 min	9.2	12.9	21.1	30.4	575	576	0.756	0.711		
IISS69	5 keV $1x10^{16}$ ^{31}P											
WAC 1-3	BG	900°C for 30 min	9.2	13.0	20.9	30.2	570	572	0.775	0.729		166
IISS70	5 keV $5x10^{15}$ ^{31}P											
WAC 1-3	BG	1000°C for 30 min	9.2	13.0	20.4	29.8	572	571	0.784	0.762		
IISS71	5 keV $1x10^{16}$ ^{31}P											
WAC 1-3	BG	1000°C for 30 min	9.2	13.3	20.7		570		0.783			
IISS72	5 keV $5x10^{14}$ ^{31}P	550°C 2 h 850°C 15 min										
WAC 1-3	25 keV $5x10^{15}$ ^{11}B	550°C 2 h	7.6	11.4	19.6	28.7	562	550	0.687	0.704		
IISS73	5 keV $5x10^{14}$ ^{31}P	550°C 2 h 850°C 15 min										
WAC 1-3	25 keV $5x10^{15}$ ^{11}B	550°C 2 h	BROKEN									
IISS74	5 keV $1x10^{15}$ ^{31}P	550°C 2 h 850°C 15 min										
WAC 1-3	25 keV $5x10^{15}$ ^{11}B	550°C 2 h	8.4	12.4	20.0	29.3	553	560	0.759	0.737		
IISS75	5 keV $1x10^{15}$ ^{31}P	550°C 2 h 850°C 15 min										
WAC 1-3	25 keV $5x10^{15}$ ^{11}B	550°C 2 h	8.9	12.5	20.4	29.8	562	560	0.774	0.727		
IISS76	5 keV $5x10^{15}$ ^{31}P	550°C 2 h 850°C 15 min										
WAC 1-3	25 keV $5x10^{15}$ ^{11}B	550°C 2 h	9.2	13.4	20.8	30.0	569	569	0.780	0.761		
IISS77	5 keV $5x10^{15}$ ^{31}P	550°C 2 h 850°C 15 min										
WAC 1-3	25 keV $5x10^{15}$ ^{11}B	550°C 2 h	BROKEN									
IISS78	5 keV $5x10^{14}$ ^{31}P	550°C 2 h + 900°C for 850°C 15 min 30 min										
WAC 1-3	BG	550°C 2 h	9.4	12.9	21.8	30.7	567	565	0.762	0.725		
IISS79	5 keV $5x10^{14}$ ^{31}P	550°C 2 h + 900°C for 850°C 15 min 30 min										
WAC 1-3	BG	550°C 2 h	9.4	12.2	21.8	30.9	570	560	0.758	0.682		

TABLE A-1. DATA FROM ION-IMPLANTED SILICON SOLAR CELLS (Continued)

Cell	Implant Conditions	Anneal Conditions	η (%)		J_{sc} (mA/cm^2)		V_{oc} (mV)		FF		L(μm)	
			No AR	AR	No AR	AR	No AR	AR	No AR	AR	SPV Before	QE After
IISS80	5 keV $1x10^{15}$ $31P$	550°C 2 h + 900°C for 850°C 15 min 30 min										
WAC 1-3	BG	550°C 2 h	9.1	13.2	21.3	30.1	560	567	0.757	0.749		
IISS81	5 keV $1x10^{15}$ $31P$	550°C 2 h + 900°C for 850°C 15 min 30 min										
WAC 1-3	BG	550°C 2 h	8.8	12.4	21.5	30.4	561	560	0.731	0.727		
IISS83	5 keV $5x10^{15}$ $31P$	550°C 2 h + 900°C for 850°C 15 min 30 min										
WAC 1-3	BG	550°C 2 h	10.3	14.1	22.2	31.1	586	580	0.789	0.760		
IISS82	BROKEN											
IISS84	BROKEN											
IISS85	5 keV $2x10^{15}$ $31P$ $N_{max}=5.65x10^{20}$											
WAC 1-3	BG	900°C, 30 min, N_2		12.6		29.0		562		0.753		80
IISS86	5 keV $N_{Dose}=2x10^{15}$ $31P$ $N_{max}=5.65x10^{12}$											
WAC 1-3	BG	900°C, 30 min, N_2		12.4		28.9		560		0.742		100
IISS87	15 keV $N_{Dose}=2.5x10^{15}$ $31P$ $N_{max}=5.65x10$											
WAC 1-3	BG	900°C, 30 min, N_2		12.8		29.1		565		0.752		110
IISS88	15 keV $N_{Dose}=2.5x10^{15}$ $31P$ $N_{max}=5.65x10^{20}$											
WAC 1-3	BG	900°C, 30 min, N_2		12.7		28.7		560		0.766		
IISS89	30 keV $N_{Dose}=3.9x10^{15}$ $31P$ $N_{max}=5.65x10^{20}$											
WAC 1-3	BG	900°C, 30 min, N_2		11.9		28.2		556		0.737		90
IISS90	30 keV $N_{Dose}=3.9x10^{15}$ $31P$ $N_{max}=5.65x10^{20}$											
WAC 1-3	BG	900°C, 30 min, N_2		12.5		28.7		560		0.758		
IISS91												
WAC 1-3	BROKEN											
IISS92	50 keV $N_{Dose}=4.6x10^{15}$ $31P$ $N_{max}=5.65x10^{20}$											
WAC 1-3	BG	900°C, 30 min, N_2		12.5		28.3		560		0.763		95
IISS93	75 keV $N_{Dose}=5.3x10^{15}$ $31P$ $N_{max}=5.65x10^{20}$											
WAC 1-3	BG	900°C, 30 min, N_2		12.3		27.8		563		0.760		100

TABLE A-1. DATA FROM ION-IMPLANTED SILICON SOLAR CELLS (Continued)

Cell	Implant Conditions	Anneal Conditions	η (%)		J_{sc} (mA/cm^2)		V_{oc} (mV)		FF		L(μm)	
			No AR	AR	No AR	AR	No AR	AR	No AR	AR	SPV Before	QE After
IISS94	75 keV $N_{Dose}=5.3\times10^{15}$ 31p $N_{max}=5.65\times10^{20}$											
WAC 1-3	BG	900°C, 30 min, N_2		11.9		27.4		558		0.758		100
IISS95	100 keV $N_{Dose}=5.9\times10^{15}$ 31p $N_{max}=5.65\times10^{20}$											
WAC 1-3	BG	900°C, 30 min, N_2		11.6		26.9		555		0.759		90
IISS96	100 keV $N_{Dose}=5.9\times10^{15}$ 31p $N_{max}5.65\times10^{20}$											
WAC 1-3	BG	900°C, 30 min, N_2		11.3		25.8		525		0.808		70
IISS97	5 keV, 4×10^{14}										110	100(SPV)
1-4<100>	BG	900°C, 30 min, N_2	8.8		20.2		552		0.786			89
IISS98	5 keV, 4×10^{14}										110	100(SPV)
1-4<100>	BG	900°C, 30 min, N_2	8.9		20.5		553		0.785			100
IISS99	5 keV, 4×10^{14}										100	70(SPV)
1-4<100>	BG	900°C, 30 min, N_2	8.9		20.5		556		0.781			109
IISS100	5 keV, 4×10^{14}										130	110(SPV)
8-12<100>	BG	900°C, 30 min, N_2	8.4		20.9		520		0.774		90	115
IISS101	5 keV, 4×10^{14}											
8-12<100>	BG	900°C, 30 min, N_2	BROKEN									
IISS102											100	350(SPV)
8-12<100>	BG	900°C, 30 min, N_2	8.3		20.9		516		0.771			106
IISS103	5 keV, 4×10^{14}										100	130(SPV)
8-12<111>	BG	900°C, 30 min, N_2	8.3		20.8		514		0.774			107
IISS104	5 keV, 4×10^{14}										110	210(SPV)
8-12<111>	BG	900°C, 30 min, N_2	8.3		20.6		524		0.773			150
IISS105	5 keV, 4×10^{14}											
8-12<111>	BG	900°C, 30 min, N_2	BROKEN									
IISS106	5 keV, 4×10^{14}											
2<111>	BG	900°C, 30 min, N_2	BROKEN									

TABLE A-1. DATA FROM ION-IMPLANTED SILICON SOLAR CELLS (Continued)

Cell	Implant Conditions	Anneal Conditions	η (%)		J_{sc} (mA/cm^2)		V_{oc} (mV)		FF		L(μm)	
			No AR	AR	No AR	AR	No AR	AR	No AR	Ah	SPV Before	QE After
IISS107	5 keV, ^{11}B $2x10^{15}$											
n-type,<111> WAC 1-2 FZ	PG	900°C, 30 min		14.9		31.6		601		0.760		
IISS108	5 keV, ^{11}B $2x10^{15}$											
WAC 1-2	PG	900°C, 30 min		14.4		31.0		600		0.751		
IISS109	5 keV ^{11}B $2x10^{15}$											
WAC 1-2	PG	1000°C, 30 min		14.7		31.1		600		0.766		
IISS110	5 keV ^{11}B $2x10^{15}$											
WAC 1-2	PG	1000°C, 30 min		14.5		31.1		600		0.755		
IISS111	30 keV ^{27}Al $3.55x10^{14}$											
WAC 1-2		900°C, 30 min		8.6		30.7		560		0.490		
IISS112	30 keV ^{27}Al $3.55x10^{14}$	Improperly										
WAC 1-2		Annealed										
IISS113	30 keV ^{27}Al $3.55x10^{14}$	Improperly										
WAC 1-2		Annealed										
IISS114	30 keV ^{27}Al $3.55x10^{14}$	Improperly										
WAC 1-2		Annealed										
IISS115	70 keV ^{70}Ga $1.2x10^{14}$	Improperly										
WAC 1-2		Annealed										
IISS116	70 keV ^{70}Ga $1.2x10^{14}$	Improperly										
WAC 1-2		Annealed										
IISS117	70 keV ^{70}Ga $1.2x10^{14}$	Improperly										
WAC 1-2		Annealed										
IISS118	70 keV ^{70}Ga $1.2x10^{14}$											
WAC 1-2		900°C, 30 min		8.5		32.6		545		0.465		

TABLE A-1. DATA FROM ION-IMPLANTED SILICON SOLAR CELLS (Continued)

Cell	Implant Conditions	Anneal Conditions	η (%)		J_{sc} (mA/cm^2)		V_{oc} (mV)		FF		L(μm)	
			No AR	AR	No AR	AR	No AR	AR	No AR	AR	SPV Before	QE After
119 M(8-15) <100>	5 keV $4x10^{15}$ ^{31}P BG	900°C, 30 min, N_2	7.8	11.1	20.0	28.2	510	575	0.769	0.746	120	23
120 M(8-15) <100>	5 keV $4x10^{15}$ ^{31}P BG	900°C, 30 min, N_2	8.2	11.3	20.7	28.7	518	533	0.768	0.742	115	83
121 M(8-15) <100>	5 keV $4x10^{15}$ ^{31}P BG	900°C, 30 min, N_2	8.1		20.9		502		0.774		100	
122 M(8-15) <100>	5 keV $4x10^{15}$ ^{31}P BG	900°C, 30 min, N_2	8.4		21.0		524		0.763			
123 M(8-15) <100>	5 keV $4x10^{15}$ ^{31}P BG	900°C, 30 min, N_2	8.2		20.9		515		0.766			
124 M(8-15) <100>	5 keV $4x10^{15}$ ^{31}P BG	900°C, 30 min, N_2	8.1		20.1		513		0.761			
125 M(8-15) <100>	5 keV $4x10^{15}$ ^{31}P BG	900°C, 30 min, N_2	BROKEN									
126 M(8-15) <100>	5 keV $4x10^{15}$ ^{31}P 25 keV $5x10^{15}$ ^{11}B	500°C 2 h, 850°C 15 min, 500°C 2 h	BROKEN								130	
127 M(8-15) <100>	5 keV $4x10^{15}$ ^{31}P 25 keV $5x10^{15}$ ^{11}B	500°C 2 h, 850°C 15 min, 500°C 2 h	10.0	13.7	23.3	32.7	560	582	0.767	0.720	120 120	597 597
128 M(8-15) <100>	5 keV $4x10^{15}$ ^{31}P 25 keV $5x10^{15}$ ^{11}B	500°C 2 h, 850°C 15 min, 500°C 2 h	9.6		22.4		552		0.776		140	320
129 M(8-15) <100>	5 keV $4x10^{15}$ ^{31}P 25 keV $5x10^{15}$ ^{11}B	500°C 2 h, 850°C 15 min, 500°C 2 h	10.0		22.7		566		0.778			
130 M(8-15) <100>	5 keV $4x10^{15}$ ^{31}P 25 keV $5x10^{15}$ ^{11}B	500°C 2 h, 850°C 15 min, 500°C 2 h	9.5		22.7		554		0.758			
131 M(8-15) <100>	5 keV $4x10^{15}$ ^{11}P 25 keV $5x10^{15}$ ^{11}B	500°C 2 h, 850°C 15 min, 500°C 2 h	9.1		22.2		553		0.717			

TABLE A-1. DATA FROM ION-IMPLANTED SILICON SOLAR CELLS (Continued)

Cell	Implant Conditions	Anneal Conditions	η (%)		J_{sc} (mA/cm^2)		V_{oc} (mV)		FF		L(μm)	
			No AR	AR	No AR	AR	No AR	AR	No AR	AR	SPV Before	QE After
132 M(8-15) <100>	5 keV $4x10^{15}$ ^{31}P 25 25 keV $5x10^{15}$ ^{11}B	500°C 2 h, 850°C 15 min, 500°C 2 h	10.0		22.6		556		0.784			
133 MT 1.5 <100>	5 keV $4x10^{15}$ ^{31}P BG	900°C, 30 min, N_2	8.6		20.1		550		0.777		110	80
134 MT 1.5 <100>	5 keV $4x10^{15}$ ^{31}P BG	900°C, 30 min, N_2	8.5		20.0		546		0.777		130	71
135 MT 1.5 <100>	5 keV $4x10^{15}$ ^{31}P BG	900°C, 30 min, N_2	8.5		19.6		556		0.780		90	
136 MT 1.5 <100>	5 keV $4x10^{15}$ ^{31}P BG	900°C, 30 min. N_2	8.9		20.1		558		0.793			
137 MT 1.5 <100>	5 keV $4x10^{15}$ ^{31}P BG	900°C, 30 min, N_2	BROKEN									
138 MT 1.5 <100>	5 keV $4x10^{15}$ ^{31}P BG	900°C, 30 min, N_2	8.71		20.0		552		0.783			
139 MT 1.5 <100>	5 keV $4x10^{15}$ ^{31}P BG	900°C, 30 min, N_2	8.6		19.8		554		0.780			
140 MT 1.5 <100>	5 keV $4x10^{15}$ ^{31}P 25 keV $5x10^{15}$ ^{11}B	500°C 2 h, 850°C 15 min, 500°C 2 h	9.7		21.6		572		0.787		80	181
141 MT 1.5 <100>	5 keV $4x10^{15}$ ^{31}P 25 keV $5x10^{15}$ ^{11}B	500°C 2 h, 850°C 15 min, 500°C 2 h	9.9		22.2		575		0.777		80	259
142 MT 1.5 <100>	5 keV $4x10^{15}$ ^{31}P 25 keV $5x10^{15}$ ^{11}B	500°C 2 h, 850°C 15 min, 500°C 2 h	9.6		21.6		570		0.781		80	
143 MT 1.5 <100>	5 keV $4x10^{15}$ ^{31}P 25 keV $5x10^{15}$ ^{11}B	500°C 2 h, 850°C 15 min, 500°C 2 h	10.1		22.0		583		0.789			
144 MT 1.5 <100>	5 keV $4x10^{15}$ ^{31}P 25 keV $5x10^{15}$ ^{11}B	500°C 2 h, 850°C 15 min, 500°C 2 h	10.0		21.9		583		0.781			

TABLE A-1. DATA FROM ION-IMPLANTED SILICON SOLAR CELLS (Continued)

Cell	Implant Conditions	Anneal Conditions	η (%)		J_{sc} (mA/cm^2)		V_{oc} (mV)		FF		L(μm)	
			No AR	AR	No AR	AR	No AR	AR	No AR	AR	SPV Before	QE After
145 MT 1.5 <100>	5 keV $4x10^{15}$ ^{31}P 25 keV $5x10^{15}$ ^{11}B	500°C 2 h, 850°C 15 min, 500°C 2 h	9.8		21.8		582		0.772			
146 MT 1.5 <100>	5 keV $4x10^{15}$ ^{31}P 25 keV $5x10^{15}$ ^{11}B	500°C 2 h, 850°C 15 min, 500°C 2 h	10.0		22.0		582		0.780			
147 WAC 1-4 <100>	5 keV $4x10^{15}$ ^{31}P BG	900°C, 30 min, N_2	8.8		20.7		547		0.777		160	108
148 WAC 1-4 <100>	5 keV $4x10^{15}$ ^{31}P BG	900°C, 30 min, N_2	8.6		20.2		541		0.785		140	87
149 WAC 1-4 <100>	5 keV $4x10^{15}$ ^{31}P BG	900°C, 30 min, N_2	8.7		20.4		543		0.783		100	
150 WAC 1-4 <100>	5 keV $4x10^{15}$ ^{31}P BG	900°C, 30 min, N_2	8.8		20.2		553		0.786			
151 WAC 1-4 <100>	5 keV $4x10^{15}$ ^{31}P BG	900°C, 30 min, N_2	8.7		20.0		551		0.787			
152 WAC 1-4 <100>	5 keV $4x10^{15}$ ^{31}P BG	900°C, 30 min, N_2	BROKEN									
153 WAC 1-4 <100>	5 keV $4x10^{15}$ ^{31}P BG	900°C, 30 min, N_2	8.7		20.0		554		0.782			
154 WAC 1-4 <100>	5 keV $4x10^{15}$ ^{31}P 25 keV $5x10^{15}$ ^{11}B	500°C, 2 h, 850°C 15 min, 500°C 2 h	9.9		22.0		571		0.789		130	742
155 WAC 1-4 <100>	5 keV $4x10^{15}$ ^{31}P 25 keV $5x10^{15}$ ^{11}B	500°C, 2 h, 850°C 15 min, 500°C 2 h	9.7		22.0		571		0.773		130	368
156 WAC 1-4 <100>	5 keV $4x10^{15}$ ^{31}P 25 keV $5x10^{15}$ ^{11}B	500°C, 2 h, 850°C 15 min, 500°C 2 h	10.1		22.2		572		0.797		130	
157 WAC 1-4 <100>	5 keV $4x10^{15}$ ^{31}P 25 keV $5x10^{15}$ ^{11}B	500°C, 2 h, 850°C 15 min, 500°C 2 h	9.8		21.6		578		0.787			

TABLE A-1. DATA FROM ION-IMPLANTED SILICON SOLAR CELLS (Continued)

Cell	Implant Conditions	Anneal Conditions	η (%)		J_{sc} (mA/cm^2)		V_{oc} (mV)		FF		L(μm)	
			No AR	AR	No AR	AR	No AR	AR	No AR	AR	SPV Before	QE After
158 WAC 1-4 <100>	5 keV $4x10^{15}$ ^{31}P 25 keV $5x10^{15}$ ^{11}B	500°C 2 h, 850°C 15 min, 500°C 2 h	9.9		21.9		578		0.778			
159 WAC 1-4 <100>	5 keV $4x10^{15}$ ^{31}P 25 keV $5x10^{15}$ ^{11}B	500°C 2 h, 850°C 15 min, 500°C 2 h	9.9		21.8		581		0.783			
160 WAC 1-4 <100>	5 keV $4x10^{15}$ ^{31}P 25 keV $5x10^{15}$ ^{11}B	500°C 2 h, 850°C 15 min, 500°C 2 h	10.2		22.2		582		0.785			
161 WAC 1-4 <100>	5 keV $4x10^{14}$ ^{31}P BG	900°C, 15 min, N_2	9.0		20.4		558		0.786			
162 WAC 1-4 <100>	5 keV $4x10^{14}$ ^{31}P BG	900°C, 15 min, N_2	9.0		20.4		558		0.790			
163 WAC 1-4 <100>	5 keV $4x10^{14}$ ^{31}P BG	900°C, 15 min, N_2										
164 WAC 1-4 <100>	5 keV $4x10^{14}$ ^{31}P BG	900°C, 15 min, N_2	8.6		20.0		550		0.780			
165 WAC 1-4 <100>	5 keV $4x10^{14}$ ^{31}P BG	900°C, 15 min, N_2	8.8		20.3		554		0.784			
166 WAC 1-4 <100>	5 keV $4x10^{14}$ ^{31}P BG	900°C, 15 min, N_2										
167 WAC 1-4 <100>	5 keV $4x10^{14}$ ^{31}P BG	900°C, 15 min, N_2										
168 WAC 1-4 <100>	5 keV $4x10^{14}$ ^{31}P BG	900°C, 15 min, N_2										
169 WAC 1-4 <100>	5 keV $4x10^{14}$ ^{31}P BG	900°C, 15 min, N_2										
170 WAC 1-4 <100>	5 keV $4x10^{14}$ ^{31}P BG	900°C, 15 min, N_2										

Screen-printed metals

TABLE A-1. DATA FROM ION-IMPLANTED SILICON SOLAR CELLS (Continued)

Cell	Implant Conditions	Anneal Conditions	η (%)		J_{sc} (mA/cm^2)		V_{oc} (mV)		FF		L(μm)	
			No AR	AR	No AR	AR	No AR	AR	No AR	AR	SPV Before	QE After
171 WAC 1-4 <100>	5 keV $4x10^{14}$ ^{31}P BG	900°C, 15 min, N_2 Screen-printed metal										
172 WAC 1-4 <100>	5 keV $4x10^{14}$ ^{31}P 25 keV $5x10^{15}$ ^{11}B	500°C 2 h, 850°C 15 min, 500°C 2 h	10.1		22.2		582		0.782			
173 WAC 1-4 <100>	5 keV $4x10^{14}$ ^{31}P 25 keV $5x10^{15}$ ^{11}B	500°C 2 h, 850°C 15 min, 500°C 2 h	9.5		21.7		574		0.763			
174 WAC 1-4 <100>	5 keV $4x10^{14}$ ^{31}P 25 keV $5x10^{15}$ ^{11}B	500°C 2 h, 850°C 15 min, 500°C 2 h	10.2		22.2		583		0.790			
175 WAC 1-4 <100>	5 keV $4x10^{14}$ ^{31}P 25 keV $5x10^{15}$ ^{11}B	500°C 2 h, 850°C 15 min, 500°C 2 h	10.3		22.3		587		0.782			
176 WAC 1-4 <100>	5 keV $4x10^{14}$ ^{31}P 25 keV $5x10^{15}$ ^{11}B	500°C 2 h, 850°C 15 min, 500°C 2 h	9.8		22.1		582		0.763			
177 WAC 1-4 <100>	5 keV $4x10^{14}$ ^{31}P 25 keV $5x10^{15}$ ^{11}B	500°C 2 h, 850°C 15 min, 500°C 2 h										
178 WAC 1-4 <100>	5 keV $4x10^{14}$ ^{31}P 25 keV $5x10^{15}$ ^{11}B	500°C 2 h, 850°C 15 min, 500°C 2 h										
179 WAC 1-4 <100>	5 keV $4x10^{14}$ ^{31}P 25 keV $5x10^{15}$ ^{11}B	500°C 2 h, 850°C 15 min, 500°C 2 h										
180 WAC 1-4 <100>	5 keV $4x10^{14}$ ^{31}P 25 keV $5x10^{15}$ ^{11}B	500°C 2 h, 850°C 15 min, 500°C 2 h										
181 WAC 1-4 <100>	5 keV $4x10^{14}$ ^{31}P 25 keV $5x10^{14}$ ^{11}B	500°C 2 h, 850°C 15 min, 500°C 2 h										
182 WAC 1-4 <100>	5 keV $4x10^{14}$ ^{31}P 25 keV $5x10^{15}$ ^{11}B	500°C 2 h, 850°C 15 min, 500°C 2 h										

Screen-printed metals

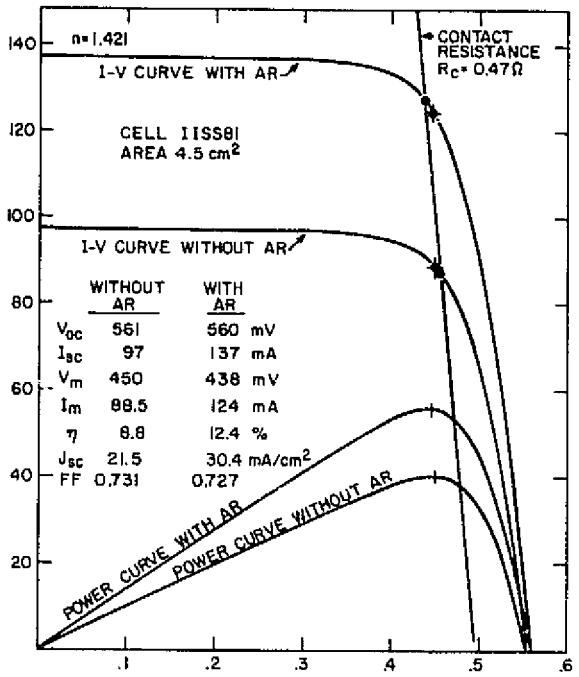

Figure A-1. A plot showing the measurement technique used to evaluate the solar cells discussed in this report. Light source: sunlamps producing 1-sun illumination level of 100 mW/cm^2. A NASA standard cell (RCA No. 14) was used to calibrate the illumination level. A thermoelectric cooler maintains 28°C during measurements.

APPENDIX B

DESCRIPTION OF THE TEST VEHICLE USED TO STUDY ION-IMPLANTED SILICON SOLAR CELLS

A composite diagram of the mask set used to fabricate the solar cells and test diodes discussed in this report is given in Fig. B-1. The cross-hatched regions are photolithographically opened using mask SS2. The dark shaded region on test diodes C and the resistor patterns D along with the entire area within the large dotted rectangle surrounding the solar cells is photolithographically opened using mask SS3A. The definition of the metallization pattern SS4 follows, but is slightly larger than, the illustrated contact openings in the case of the diodes and resistors, the dark shaded region. A wafer map is given below which shows the device assignment numbers and areas referred to in the report.

Wafer Map

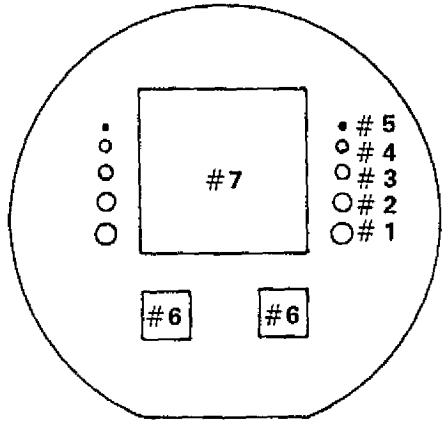

Device	Diam (mil)	Area (cm^2)
1	100	5.07×10^{-2}
2	80	3.24×10^{-2}
3	60	1.82×10^{-2}
4	40	8.11×10^{-3}
5	20	2.03×10^{-3}
6	–	0.316
7	–	4.5

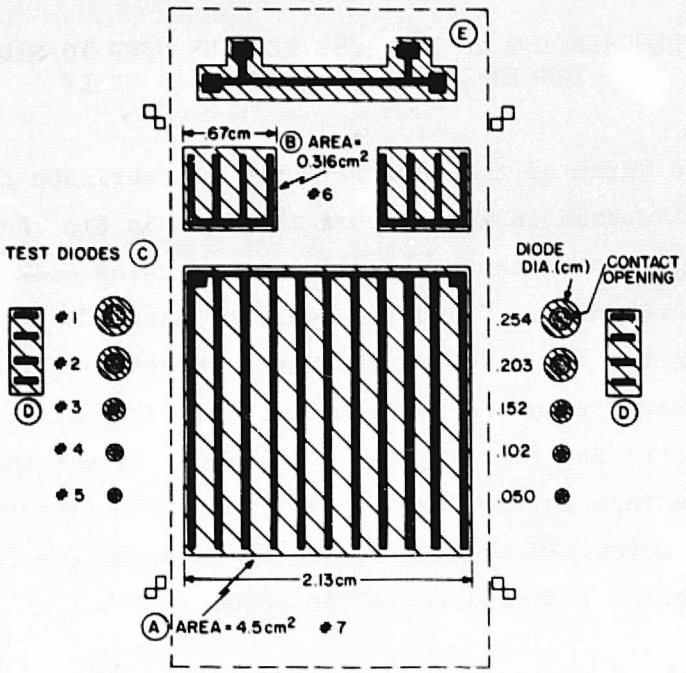

Figure B-1. Composite diagram of mask set.

APPENDIX C

EMISSION SPECTROGRAPHIC ANALYSES - INK

TABLE C-1. EMISSION SPECTROGRAPHIC ANALYSIS OF THICK-FILM CATION CONSTITUENTS
(ppm by weight)

	Engelhard				Thick Film Systems	
Element	E-422-C Ag	E-422-D Ag/Al	E-422-E Ag	E-422-F Ag/Al	A-250 Ag	3347 Ag
Ag	S*	S*	S*	S*	S*	S*
Al	15-150	3000-30,000	10-100	3000-30,000	10-100	20-200
Zn	100-1000	100-1000	----	30-300	30-300	30-300
Na	10-100	10-100	60-600	100-1000	15-150	20-200
Cu	20-200	20-200	200-2000	200-2000	60-600	100-1000
Fe	15-150	100-1000	10-100	100-1000	10-100	15-150
Pb	3000-30,000	3000-30,000	600-6000	2000-20,000	15-150	3000-30,000
Mg	0.6-6	30-300	20-200	60-600	30-300	6-60
Mn	0.3-3	6-60	0.3-3	10-100	1-10	1-10
Sb	30-300	30-300	----	----	----	----
Si	300-3000	500-5000	500-5000	600-6000	150-1500	600-6000
B	600-6000	600-6000	300-3000	300-3000	----	300-3000
Ba	----	10-100	----	----	----	----
Ti	----	60-600	30-300	150-1500	3-30	3-30
Ga	----	10-100	----	10-100	----	----
Cd	----	----	10-1000	100-10000	----	----
Pd	----	----	----	----	----	6-60
Bi	----	----	----	----	----	10-100
Au	----	----	----	----	----	10-100

S* = amount present is substantially above analytical range.

TABLE C-2. EMISSION SPECTROGRAPHIC ANALYSIS OF THICK-FILM CATION CONSTITUENTS, O-I 6105 Ag
(ppm by weight)

Element	Lot T-70526	Lot 71114
Ag	S*	S*
P	1000-10,000	1500-15,000
Na	100-1000	100-1000
Zn	10-100	---------
Cu	100-1000	60-600
Ti	3-30	3-30
Al	15-150	60-600
Bi	1-10	1-10
Fe	6-60	2-20
Si	60-600	15-150
Pb	3-30	30-300
Mg	5-50	3-30
Mn	1-10	---------
Au	3-30	---------
Ca	---------	6-60

S* = amount present is substantially above analytical range.

TABLE C-3. EMISSION SPECTROGRAPHIC ANALYSIS OF THICK-FILM CATION CONSTITUENTS, Cermalloy Cu 7029-5
(ppm by weight)

Element	Cermalloy Cu 7029-5
Cu	S*
Ni	1-10
Pd	150-1500
Ag	10-100
Na	60-600
Zn	20-200
Ca	10-100
Al	150-1500
Bi	0.6-6
Fe	6-60
Si	200-2000
Pb	1000-10000
Mg	6-60
Mn	50-500
B	300-3000

*S = amount present is substantially above analytical range.

APPENDIX D

EMISSION SPECTROGRAPHIC ANALYSES - POWDERS

TABLE D-1. EMISSION SPECTROGRAPHIC ANALYSES OF SILVER POWDER CATION CONSTITUENTS (ppm by weight)

Element	Metz K-150	Metz FS Type C	U.S. Metal Refining Lot 71-2
Si	100-1000	50-500	60-600
Mg	2-20	5-50	10-100
Pb	10-100	6-60	15-150
Fe	2-20	3-30	10-100
Cu	600-6000	10-100	100-1000
Zn	30-300	30-300	30-300
Al	----	2-20	6-60
Ca	----	15-150	3-30
Na	----	60-600	60-600
Mn	----	----	1-10
Sn	----	----	3-30
Maximum Impurities			
Total, wt pct	0.74	0.18	0.30
Ag, wt pct	99.26	99.82	99.70
Specific Surface Area (BET Method) m^2/gm	3.4	0.88	0.24

TABLE D-2. EMISSION SPECTROGRAPHIC ANALYSES OF CELLULOSIC POLYMERS CATION CONSTITUENTS (ppm by weight)

Element	Ethyl Cellulose*	Klucel**	Klucel
	N-300	L	H
Ni	3-30	----	----
Na	300-3000	300-3000	60-600
Cu	6-60	150-1500	2-20
Ca	100-1000	----	100-1000
Fe	10-100	2-20	0.6-6
Mg	5-50	5-50	5-50
Si	3-30	6-60	30-300
Ag	----	0.03-0.3	0.6-6
Al	----	3-30	2-20
Sn	----	6-60	----
Pb	----	----	3-30
Maximum Impurities			
Total, wt pct	0.43	0.47	0.20

*Hercules, Inc, Wilmington, DE.
**Hercules, Inc, Wilmington, DE - Klucel is registered trademark for hydroxyproply cellulose.